Ultra-high field NMR spectroscopy of GABA in the human brain

Dissertation
zur
Erlangung des Doktorgrades (Dr. rer. nat.)
der
Mathematisch-Naturwissenschaftlichen Fakultät
der
Rheinischen Friedrich-Wilhelms-Universität Bonn

von
Yannik Völzke
aus
Lüdenscheid

Bonn, 2023

Angefertigt mit Genehmigung der Mathematisch-Naturwissenschaftlichen Fakultät der
Rheinischen Friedrich-Wilhelms-Universität Bonn

1. Gutachter:	Prof. Tony Stöcker
2. Gutachter:	Prof. Dieter Meschede
Tag der Promotion:	03.07.2023
Erscheinungsjahr:	2023

Acknowledgements

This work would have not been possible without the support of many people. I would like to thank

- Prof. Tony Stöcker and Prof. Elke Hattingen for the opportunity to join the DZNE and to work on this topic.
- Prof. Tony Stöcker for his continuous guidance and support. His open door was always appreciated.
- The examining board. Especially Prof. Dieter Meschede who now spends valuable time in his well-earned retirement for his former student
- Eberhard Pracht for always pushing my research, helping me to get familiar with the IDEA framework an all the fruitful discussions about.
- Rüdiger Stirnberg for allowing me to use his well-rounded EPI sequence which was great starting point for developing the EPSI readout. Chapter 5 would not have been possible without this head start and his patience to answer all the questions that arose along the way.
- My PhD office mates Jolanda, Alex, and Suzan for the great companionship during all those years
- Suzan Akbey, Eberhard Pracht, Martin Schidlowski, Jolanda Schwarz, and Markus Werner for spending their time for proofreading this thesis.
- The whole AG Stöcker group for creating such a great working environment.
- Anke Rühling for the introduction me to MR scanning and for organizing the group retreats.
- All my friends for all the support and joy
- My parents for their unconditional support
- Johanna for the past 11 years

Abstract

Magnetic resonance imaging (MRI) is a non-invasive and radiation-free imaging method that has been utilized in medicine for decades. Using magnetic fields, the nuclear spins within the tissue are perturbed, and the resulting magnetization is measured. A strong, homogeneous main field creates a net magnetization within the subject. This magnetization can be manipulated by applying RF pulses on-resonant to the nuclear magnetic resonance frequency. Switchable gradient fields allow to spatially and temporally alter the resonance frequency. Next to high-resolution anatomical scans, a wide variety of physiological processes, like perfusion and diffusion, can be visualized using different measurement sequences.

The time evolution of the magnetization is affected by the molecular surrounding of the nuclear spin. Magnetic resonance spectroscopy (MRS) uses this effect to differentiate the signals of different chemical compounds and infer their concentrations. Although MRS is historically older than MRI, it is still rarely used in clinical practice. This is mainly because of the limited signal strength. MRI uses the signal from the hydrogen nuclei within the water molecules. The concentration of the compounds that are measured using MRS is much lower. Furthermore, elaborate data processing is needed to ensure reliable concentration estimates.

A higher magnetic field strength leads to an increased signal. Additionally, the spectral resolution increased. Therefore, MRS could strongly benefit from the relatively recent introduction of clinical 7 Tesla MRI machines. The higher field strength does not come without challenges. The higher resonance frequency facilitates slice selection, which is needed to obtain a localized signal. Furthermore, the higher RF frequency leads to a more effective absorption within the tissue. For security reasons, the applicable RF power is limited. This must be taken into account when planning measurement sequences. Lastly, the magnetic fields are less homogeneous compared to lower field strengths.

This thesis focuses on measuring the concentration of gamma-amino butric acid (GABA), the dominant inhibitory neurotransmitter in the human brain. Changes in GABA concentration are linked to multiple diseases. Due to its low concentration and the signal overlap of more prominent metabolites, a GABA-specific measurement sequence is needed. *J*-editing is a method that is based on measuring two slightly different spectra. The resonance shapes of the target compound differ in both spectra, while the resonance shapes of an overlapping compound are identical. Consequently, the signal of the target compound can be isolated by subtracting both spectra. MEGA-sLASER is a high-field sequence that uses this principle.

The main part of this thesis focuses on the implementation, optimization, and validation of a MEGA-sLASER sequence for GABA concentration estimation. The main target region is the hippocampus, a brain region that is severely affected by Alzheimer's disease. Strong field inhomogeneities are present in this region, hampering accurate concentration estimates. No

hippocampal GABA concentration has previously been published. An inter-subject variation, comparable to published values in more accessible brain regions, was found. To achieve this reproducibility, the pulse sequence was optimized with simulated GABA resonances. Furthermore, a dedicated data processing pipeline was implemented.

Additionally, an imaging module is added to the sequence. This allows measuring the spatial distribution of the GABA concentration inside the human brain. Within a single slice, the spatial distribution was imaged with a resolution of 1 mm. Because of the small voxel size and the low GABA concentration, quantification is very difficult. Despite strong noise in the concentration maps, higher GABA concentration in grey matter than in white matter was found. This is in agreement with several published studies.

Zusammenfassung

Magnetresonanztomographie wird seit Jahrzehnten in der Medizin als bildgebendes Verfahren verwendet, welches strahlungsfrei und nichtinvasiv ist. Mit Hilfe magnetischer Felder werden die Kernspins innerhalb des Gewebes beeinflusst und die resultierende Magnetisierung wird vermessen. Ein starkes, homogenes Hauptfeld erzeugt eine Magnetisierung im Probanden. Mittels RF-Pulsen in der kernmagnetischen Resonanzfrequenz kann diese Magnetisierung manipuliert werden und mittels schaltbaren Gradientenfeldern kann diese Resonanzfrequenz zeitlich und räumlich verändert werden. Mittels unterschiedlichen Messsequenzen kann neben hochaufgelösten anatomischen Aufnahmen auch eine Vielzahl an physiologischen Prozessen, wie beispielsweise Diffusion oder Perfusion dargestellt werden.

Die Zeitentwicklung der Magnetisierung wird durch die molekulare Umgebung der Kernspins beeinflusst. Magnetresonanzspektroskopie (MRS) nutzt diesen Effekt aus, um das Signal unterschiedlicher chemischer Komponenten zu trennen und somit die Konzentration dieser Komponenten zu bestimmen. Obwohl MRS historisch älter ist als die Bildgebung wird es immer noch selten im klinischen Alltag angewandt. Die liegt zum Großteil an dem limitierten Signal. Die Bildgebung nutzt das Signal, welches von den in Wassermolekülen gebundenen Wasserstoffatomen erzeugt wird. Die Konzentration der mittels MRS zu vermessenen Stoffe ist mehrere Größenordnungen geringer ist als die des Wassers. Desweiteren ist eine aufwändige Datenanalyse notwendig um eine gute Konzentrationsbestimmung zu gewährleisten.

Eine höhere Feldstärke führt zu einem höheren Signal. Zusätzlich steigt die spektrale Auflösung. MRS könnte daher stark von der relativ kürzlichen Einführung von klinischen 7 Tesla MRT Geräten profitieren. Die höhere Feldstärke bringt allerdings auch einige Probleme mit sich. Die höhere Resonanzfrequenz erschwert die Schichtselektion, die notwendig ist um ein lokalisiertes Signal zu erzeugen. Deswegen sind spezielle Hochfeldsequenzen nötig. Außerdem führt die höhere Frequenz zu einer effizienteren Absorption der RF Leistung im Gewebe. Aus Sicherheitsgründen ist daher die applizierte RF Leistung limitiert. Dies muss bei der Planung von Messsequenzen berücksichtigt werden. Zusätzlich dazu sind die magnetischen Felder weniger homogen bei größeren Feldstärken.

Diese Arbeit beschäftigt sich mit der MR-spektroskopischen Bestimmung der Konzentration von γ-Aminobuttersäure (GABA), des wichtigsten inhibitorischen Neurotransmitters im menschlichen Gehirn. Veränderungen der GABA Konzentration kann mit einer Vielzahl von Erkrankungen in Verbindung gebracht werden. Durch die geringe GABA Konzentration und den Überlapp mit Signalen von anderen Stoffen ist eine GABA-spezifische Sequenz nötig. *J*-Editierung ist eine Methode bei der zwei unterschiedliche Spekren mit leicht unterschiedlichen Messsequenzen aufgenommen werden. Das Signal des Zielstoffes ist unterschiedlich in beiden Spektren, während die überlappenden Signale eines anderen Stoffes identisch sind. Durch

Subtraktion beider Spektren kann das Signal des Zielstoffes isoliert werden. MEGA-sLASER ist eine Hochfeldsequenz, die diese Prinzip nutzt.

Der Hauptteil dieser Arbeit beschäftigt sich mit der Entwicklung, Optimierung und Validierung einer MEGA-sLASER Messsequenz zur Bestimmung der GABA Konzentration im menschlichen Gehirn. Der Hippokampus, eine Hirnregion, die in Alzheimerpatienten besonders betroffen ist, ist hier die Zielregion. In dieser Region gibt es eine sehr starke Feldinhomogenität, die das genaue Bestimmen der GABA Konzentration zusätzlich erschwert. Keine GABA Konzentration im Hippokampus wurde zuvor veröffenticht. Die im Rahmen dieser Arbeit implementierte MEGA-sLASER Sequenz erlaubt eine Bestimmung der GABA Konzentration im Hippokampus mit einer Interprobandenvarianz, die vergleichbar ist mit veröffentlichten Werten in Hirnregionen, die eine höhere Feldinhomogenität aufweisen. Um diese Varianz zu erreichen wurden die Pulse in der Sequenz mittels Simulationen optimiert. Außerdem wurde ein speziell auf diese Anwendung zugeschnittenes Analyseverfahren implementiert.

Anschließend wird die entwickelte Sequenz um ein Bildgebungsmodul erweitert. Dies ermöglicht die räumliche Verteilung der GABA Konzentration im menschlichen Gehirn zu vermessen. In einer einzelnen Schicht wurde die räumliche GABA Konzentration mit einer Auflösung von 1 cm aufgelöst. Durch die geringe Voxelgröße und der geringen GABA Konzentration ist das GABA Signal sehr gering und die Quantifizierung sehr schwierig. Trotz starkem Rauschen konnte in den Konzentrationskarten eine höhere GABA Konzentrationen in grauer Hirnsubstanz als in weißer Hirnsubstanz vermessen werden. Dies ist in Übereinstimmung mit einigen veröffentlichten Messungen.

Contents

CHAPTER 1

Introduction

1.1 Motivation

Nuclear magnetic resonance (NMR) extracts information about a material by manipulating the nuclear spins within this material by applying magnetic fields and measuring the resulting magnetization. Consequently, it can be used as a completely non-invasive imaging modality that does not rely on ionizing radiation, like positron emission tomography (PET) or computed tomography (CT). It is highly flexible, and multiple different contrast mechanisms can be explored. One of these is NMR spectroscopy which allows to differentiate the signals of different chemical compounds within the sample and, therefore, estimates their concentrations. Early experiments date back to Bloch [1] and Purcell [2] in the 1940s, who were awarded the Nobel Prize in physics in 1953. After the development of Fourier-based spectroscopy by Ernst [3], who was awarded a Nobel Prize in chemistry in 1991, it became an important tool in chemistry. First experiments with biological tissue were performed in the early 1970s [4, 5].

While magnetic resonance imaging (MRI) has been an essential modality in everyday clinical practice for several decades, NMR spectroscopy is still rarely used in clinical practice. One intrinsic problem of NMR spectroscopy is the low signal strength. MRI is, in most cases, based on the signal arising from the hydrogen nuclei within the water molecules. As other chemicals, like brain metabolites, are far less abundant, their signal strength is reduced by several orders of magnitude. Additionally, the signals of similar molecules overlap, which further complicates the concentration estimates. For these reasons, intensive data processing is necessary, which might explain the limited usage of *in-vivo* NMR spectroscopy in the medical routine. Furthermore, there is a lack of standardization of measurement procedures, hampering the routine usage of *in-vivo* NMR spectroscopy even further.

Single-voxel spectroscopy (SVS) creates magnetization in one preselected spatial region, the voxel of interest (VoI), by suppressing the signal of the rest of the tissue. By measuring the time evolution of the resulting magnetization, the frequency profile can be extracted, from which the chemical composition of the VoI can be inferred. The first measurement sequence that utilized this technique was Point RESolved Spectroscopy (PRESS). Using PRESS, Bottomley measured the first *in vivo* NMR spectroscopic measurements in the human brain were performed in 1985 [6]. Ever since, SVS has been used in medical research, as it gives unique insides into the

biochemistry within living tissue.

Due to the inherently low signal of SVS, intensive data processing is needed to estimate the concentrations of different metabolites reliably. A basis function for each chemical compound is defined based on the molecular shape and the measurement sequence. This is usually done by quantum mechanical simulation of the time evolution of the magnetization. These basis functions are fitted to the measured data, and the concentrations are inferred from the fitted amplitude of the respective basis function. Multiple toolboxes are available for this step, most notably [7], Gannet [8], jMRUI [9], and TARQUIN [10]. Before this quantification is performed, multiple additional data processing steps can be applied to increase the data quality.

In the 1980s, magnetic resonance spectroscopic imaging (MRSI) was introduced [11, 12], which includes MRI techniques in NMR spectroscopic acquisitions. In MRI, the NMR signal is measured spatial frequency space. After image reconstruction, spectra of different spatial positions can be obtained simultaneously. This allows to measure concentrations and the spatial distribution of concentrations. The achievable resolution is limited by the signal strength of the targeted compounds and the available acquisition time. The introduction of echo-planar spectroscopic imaging (EPSI) in 1994 [13] resulted in a strong increase in acquisition speed.

Ultra-high field MR scanners offer a higher signal strength, due to an increase of magnetization, and easier separation of the signals of different metabolites, due to an increased spectral dispersion. However, it does not come without challenges. Field inhomogeneities increase, and NMR spectroscopy is especially susceptible to these. Due to the low sensitivity, the voxel size in spectroscopic measurements has to be considerably larger compared to MRI. Therefore, intra-voxel field variations are more problematic. Furthermore, the increased large-scale inhomogeneities impede MRSI.

Ever since the introduction of *in-vivo* NMR spectroscopy, the human brain has been a prime target. The number of accessible metabolites, has been steadily increased. These metabolites also include γ-aminobutric acid (GABA) using NMR spectroscopy, which is the target metabolite in this thesis. GABA is the primary inhibitory neurotransmitter in the human brain [14] and also acts as a glio transmitter [15]. Changes in the GABA concentration have previously been linked to numerous diseases, including Parkinson's [16], schizophrenia [17], and depression [18]. The small concentration and the signal overlap with more prominent resonances make GABA a difficult metabolite to access using *in-vivo* NMR spectroscopy. Therefore, GABA is usually measured using a specialized measurement technique called *J*-editing, which was introduced by Mescher and Garwood in 1998 [19].

Alterations in function and size of the hippocampus is observed are Alzheimer's disease [20]. The hippocampus lies in proximity to susceptibility discontinuities within the brain. These cause substantial field inhomogeneities within and around the hippocampus. This makes the hippocampus an exceptionally difficult target region. To minimize the effect of intra-voxel field variations, the hippocampus is often only partially measured in NMR spectroscopy [21–23]. However, no hippocampal GABA concentration has previously been reported.

1.2 Thesis outline

This thesis contains five main parts. First, an overview of the theoretical background (chapter 2), followed by an introduction to the data analysis approach developed during the course of this thesis (chapter 3). Single-voxel experiments on GABA spectroscopy are presented (chapter 4), as well as spectroscopic imaging of GABA (chapter 5). A conclusion (chapter 6) summarizes the results and gives a small outlook

In chapter 2 of this thesis, the physical and biological background of GABA spectroscopy at ultra-high field is explained. This includes an introduction to the quantum mechanical origins of the NMR signal and a brief overview of the role of GABA in the human brain, especially in Alzheimer's disease. Afterwards, the physical background of modern measurement techniques is explained for SVS and MRSI. Finally, the experimental challenges, which arise with the usage of ultra-high field scanners, are introduced.

Intensive data processing is needed to obtain reliable and accurate concentration measures. This is especially the case for GABA spectroscopy. In chapter 3, the data processing pipeline, which was developed during this thesis, is introduced. Data processing includes image reconstruction techniques, and the compensation for systematic instabilities.

In chapter 4, the main experiment of this thesis is described, including some preperation experiments. The reproducibility of the measurement of hippocampal GABA concentrations is optimized. The findings are partially published in a MAGMA paper [24]. To prepare for this experiment, the pulse sequence is optimized using simulated GABA measurements. Afterwards, field homogenization is optimized in a brief, preceding *in vivo* study. The aim was to have the field at the hippocampus as homogenous as possible, while having a stable measurement process, as a routine usage of the measurement sequence is required for clinical studies. Finally, a pilot study is performed to tailor the data processing to hippocampus GABA spectroscopy and thereby optimize the reproducibility of the GABA concentration measures.

After incorporating all the optimizations explained in chapter 4, the measurement approach was adapted for MRSI. This experiment is explained in chapter 5. The spatial distribution of the GABA concentration was measured in one volunteer.

Finally, in chapter 6, the findings of this thesis are briefly summarized, and an outlook is given.

1.3 Publications

The following works have been published within the scope of this thesis:

Journal paper

- Völzke Y, Pracht ED, Hattingen E, Y Tse DH, Stöcker T. *On the reproducibility of hippocampal MEGA-sLASER GABA MRS at 7T using an optimized analysis pipeline* MAGMA. 2021 Jun;34(3):427-436. DOI: 10.1007/s10334-020-00879-9

Conference contributions

- Völzke Y, Pracht ED, Hattingen E, Stöcker T. *Towards repeatable GABA-MRS of the hippocampus: Development of an extended post-processing pipeline* Proc. Intl. Soc. Mag. Reson. Med. 26 (2018)

- Völzke Y, Pracht ED, Hattingen E, Y Tse DH, Stöcker T. *Improving the reproducability of GABA+ MRS using spectral registration* Proceedings of the 3th Scientific Meeting of the European Society for Magnetic Resonance in Medicine and Biology (2017)

CHAPTER 2

Physical and Biological Background of *in-vivo* NMR spectroscopy

2.1 Fundamentals of Nuclear Magnetic Resonance

Nuclear Magnetic Resonance (NMR) aims to extract information about the chemical composition of a sample. This is achieved by creating magnetization caused by the nuclear spin ensemble within the sample, and manipulating this magnetization. In an NMR experiment, three different magnetic fields are used to interact with these spins: a strong, homogeneous, and constant field, gradient fields, and a radio-frequency field.

The system of nuclear spins and magnetic fields is best described in a semi-classical fashion, where the spins are treated as a quantum mechanical ensemble interacting with classical fields. Therefore, the nuclear spin Hamiltonian needs to be developed.

2.1.1 Nuclear spin Hamilton operator in the presence of magnetic fields

The magnetic moment of a nucleus, created by its spin, can be described as

$$\hat{\vec{\mu}} = \gamma\hbar\hat{\vec{I}}, \tag{2.1}$$

where γ is the gyromagnetic ratio and $\hat{\vec{I}}$ the spin angular momentum operator. Thus, the nuclear spin Hamiltonian in the presence a magnetic field $\vec{B}$ is given by

$$\mathcal{H} = -\hat{\vec{\mu}}\vec{B} = -\gamma\hbar\vec{B}\hat{\vec{I}}. \tag{2.2}$$

Influence of a constant external field

When the spin ensemble is introduced to a strong, homogeneous, external field $\vec{B}_0$, equation 2.2 simplifies to

$$\mathcal{H}_{\text{ext}} = -\underbrace{\gamma B_0}_{\omega_0} \hbar \hat{I}_z. \tag{2.3}$$

Thus, the Larmor frequency ω_0 depends linearly on the nucleus and the field strength. Note that the external field points in z-direction. Therefore, the eigenstates of the Hamiltonian are the Zeeman states

$$\begin{aligned} |\uparrow\rangle &:= \begin{pmatrix}1\\0\end{pmatrix}, \text{fulfilling } \mathcal{H}_{\text{ext}}|\uparrow\rangle = -\frac{\hbar\omega_0}{2}|\uparrow\rangle \\ |\downarrow\rangle &:= \begin{pmatrix}0\\1\end{pmatrix}, \text{fulfilling } \mathcal{H}_{\text{ext}}|\downarrow\rangle = +\frac{\hbar\omega_0}{2}|\downarrow\rangle . \end{aligned} \tag{2.4}$$

As the spins form a canonical ensemble, the density matrix in thermal equilibrium is given by

$$\begin{aligned} \sigma^{\text{th}} &= \frac{\exp\left\{(-\beta\hat{H})\right\}}{\text{Trace}(\exp\left\{(-\beta\hat{H})\right\})} = \frac{\sum_m \exp\{(-\beta E_m)\}\,|m\rangle\langle m|}{\sum_m \exp\{(-\beta E_m)\}} \\ &= \frac{\exp\{(\beta\hbar\omega_0/2)\}\,|\uparrow\rangle\langle\uparrow| + \exp\{(-\beta\hbar\omega_0/2)\}\,|\downarrow\rangle\langle\downarrow|}{\exp\{(\beta\hbar\omega_0/2)\} + \exp\{(-\beta\hbar\omega_0/2)\}} \\ &\approx \mathbf{1} + \frac{\hbar\omega_0}{2k_{\text{B}}T}\begin{pmatrix}1 & 0\\0 & -1\end{pmatrix} \\ &= \mathbf{1} + \frac{\hbar\gamma\omega_0}{2k_{\text{B}}T}I_z, \end{aligned} \tag{2.5}$$

with the Boltzman constant k_B, the temperature T and $\beta = (k_{\text{B}}T)^{-1}$. Thus, the external magnetic field causes a net magnetization of the spin ensemble and therefore, the measured subject. Under the high-temperature approximation, the net equilibrium magnetization is proportional to the strength of the magnetic field.

Gradient fields

Gradient coils generate magnetic fields parallel to $\vec{B}_0$. The strengths of these gradient fields are linearly dependent on one spatial dimension. In an NMR experiment, three gradient coils are used, one for each spatial dimension. As the gradient field also points in z-direction the nuclear spin Hamiltonian is given by

$$\mathcal{H}_0(\vec{r}) = -\hbar(\omega_0 + \gamma(G_x x + G_y y + G_z z) = -\hbar(\omega_0 + \gamma\vec{G}\vec{r})\hat{I}_z, \tag{2.6}$$

where $\vec{G}$ is the field gradient and is referred to as gradient strength in the course of this thesis.

Radio frequency field

Following equation 2.2, the spin ensemble is also affected by a radio frequency (EF)pulse. Only an RF pulse with a field oriented perpendicular to the main field is considered. The field of an RF pulse can be split into a clockwise rotating and an anti-clockwise rotating field where only the clockwise rotating field affects the spin ensemble [1]. Using this, the RF field contribution to the nuclear spin Hamiltonian can be written as

$$\mathcal{H}_{\mathrm{RF}} = \hbar\gamma B_1(t)\left(\cos\left(\omega_{\mathrm{RF}}t + \phi(t)\right)\hat{I}_x + \sin\left(\omega_{\mathrm{RF}}t + \phi(t)\right)\hat{I}_y\right), \tag{2.7}$$

where $B_1(t)$ is the field amplitude of the resonant part of the RF field and $\phi(t)$ is the phase of the pulse. Note that the RF pulse introduces an inherent time dependence of the Hamiltonian. Every time-dependent magnetic field induces electrical currents, and consequently, energy is deposited in the subject. This energy will be converted to heat inside the subject. To ensure patient safety, the specific absorption rate (SAR) for human use is limited. Following

$$\begin{aligned} W &\propto \sigma j^2 \propto \left(\frac{\partial B}{\partial t}\right)^2 \propto B_1^2\omega_0^2 \\ &\propto B_1^2 B_0^2, \end{aligned} \tag{2.8}$$

where j is the induced current density and σ the conductivity, it becomes apparent that SAR depends quadratically on the field strength. Therefore, it becomes more problematic for ultra-high field applications and has to be considered in sequence planning.

Chemical Shift

So far, the chemical environment the nuclei are embedded in was not considered. However, the electrons surrounding the nuclei create their own magnetic field and, thus, alter the local magnetic field [25, 26]. This causes the Larmor frequency to depend on the chemical environment of the nucleus. This effect is called chemical shift and is linear in B_0. A standardized dimensionless frequency measure, defined as

$$f_i = 10^{-6}\frac{\omega_{0,i} - \nu_{\mathrm{ref}}}{\nu_{\mathrm{ref}}}, \tag{2.9}$$

allows for comparison between different field strengths. Here the subscript i denotes the different chemical environments. The Larmor frequency of Tetramethylsilan (TMS) is used as a reference frequency. The nuclear spin Hamiltonian of a system with differently affected nuclei is given by

$$\mathcal{H}_{0,N} = \hbar\sum_{n_1}^{N}\omega_{0,n}\hat{I}_{n,z}. \tag{2.10}$$

Internal coupling

Nuclear spins can couple with each other. NMR spectroscopy can only be done with relatively small molecules in an aqueous solution *in-vivo*. In these conditions, the effect of direct coupling does not affect energy levels. However, nuclei can indirectly couple via the electronic cloud [27]. The internal coupling Hamiltonian is given by

$$\mathcal{H}_{ij}^{J} = 2\pi\hbar J_{ik}\hat{\vec{I}}_i\hat{\vec{I}}_j = 2\pi\hbar J_{ik}\left(\underbrace{\hat{I}_{i,z}\hat{I}_{j,z}}_{longitudinal} + \underbrace{\frac{1}{2}\left(I_i^+ I_j^- + I_i^- I_j^+\right)}_{transversal}\right), \tag{2.11}$$

where J_{ij} is the coupling strength between the nuclei i and j. In the small coupling regime $|\omega_i - \omega_j| >> J_{ij}$, the effect of the transversal component may be omitted. With this approximation and in the absence of an RF field, the Zeeman states are still eigenstates of the nuclear spin Hamiltonian. For a two-spin system, the eigenstates are

$$\begin{aligned}
|\uparrow\uparrow\rangle &:= \begin{pmatrix}1\\0\\0\\0\end{pmatrix}, \text{fulfilling } (\mathcal{H}_0 + \mathcal{H}_{1,2}^{\mathrm{J}})\,|\uparrow\uparrow\rangle = (-\tfrac{\omega_{0,1}}{2} - \tfrac{\omega_{0,2}}{2} + 2\pi J)\,|\uparrow\uparrow\rangle \\
|\uparrow\downarrow\rangle &:= \begin{pmatrix}0\\1\\0\\0\end{pmatrix}, \text{fulfilling } (\mathcal{H}_0 + \mathcal{H}_{1,2}^{\mathrm{J}})\,|\uparrow\downarrow\rangle = (-\tfrac{\omega_{0,1}}{2} + \tfrac{\omega_{0,2}}{2} - 2\pi J)\,|\uparrow\downarrow\rangle \\
|\downarrow\uparrow\rangle &:= \begin{pmatrix}0\\0\\1\\0\end{pmatrix}, \text{fulfilling } (\mathcal{H}_0 + \mathcal{H}_{1,2}^{\mathrm{J}})\,|\downarrow\uparrow\rangle = (+\tfrac{\omega_{0,1}}{2} - \tfrac{\omega_{0,2}}{2} - 2\pi J)\,|\downarrow\uparrow\rangle \\
|\downarrow\downarrow\rangle &:= \begin{pmatrix}0\\0\\0\\1\end{pmatrix}, \text{fulfilling } (\mathcal{H}_0 + \mathcal{H}_{1,2}^{\mathrm{J}})\,|\downarrow\downarrow\rangle = (+\tfrac{\omega_{0,1}}{2} + \tfrac{\omega_{0,2}}{2} + 2\pi J)\,|\downarrow\downarrow\rangle\,.
\end{aligned} \tag{2.12}$$

Due to the need for the electronic cloud, this coupling mechanism is strongly distance-dependent. Therefore, it is not only completely intra-molecular but also is usually omitted for nuclei distanced more than two covalent bounds. Thus, the combined total nuclear spin Hamiltonian of a spin system formed by all nuclear spins within a molecule is given by

$$\mathcal{H}(\vec{r},t) = \hbar\sum_i \omega_i\hat{I}_{i,z} + 2\pi\hbar\sum_{(i,j)} J_{i,j}\,\hat{\vec{I}}_i\hat{\vec{I}}_j + \vec{\hbar}\gamma G(\vec{r},t)\vec{r}\hat{\vec{I}} + \omega_1(t)(\hat{I}_x\cos(\phi(t)) + \hat{I}_y\sin(\phi(t))), \tag{2.13}$$

where the summation in the indirect coupling term is performed for unique pairs.

Magnetic equivalence

Exploiting spatial symmetries within the molecular structure, formula 2.13 can be simplified. Internal coupling between magnetically equivalent nuclei does not affect the time evolution of the magnetization[28, 29] and can thus be omitted when calculating the magnetization. A set of nuclei is considered magnetically equivalent if:

1. They have identical chemical shift due to a symmetry transformation that maps the molecule on itself, exchanging the position of these nuclei.

2. The nuclei have identical coupling to all other nuclei within the molecule.

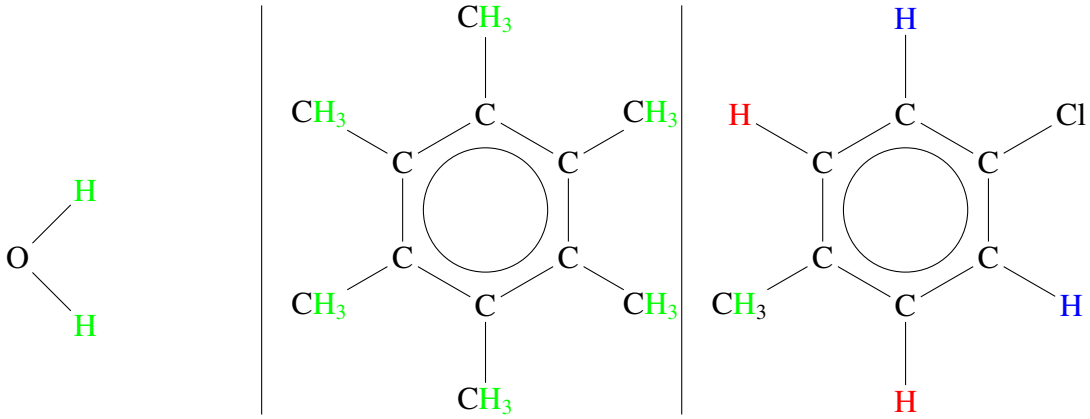

Figure 2.1: Examples for chemically equivalent hydrogen nuclei. All hydrogen atoms of the water (left) and hexa-methyl benzene (middle) are chemically equivalent. As there are no other nuclei with spin present in the molecule, they are also magnetically equivalent. In the case of p-chlorotoluene (right) the situation is more difficult. The nuclei within the CH_3 group (green) are magnetically equivalent. The other two pairs of chemically equivalent nuclei (blue and red) are not magnetically equivalent as the couple differently to the nuclei of the individual nuclei from the other group.

The first condition is also called chemical equivalence. Note that, due to rapid internal rotation, this condition can approximately be extended to nuclei within certain chemical groups, like methyl groups [29]. Figure 2.1 shows magnetic equivalence in some exemplary molecules. All hydrogen nuclei within water (left) are chemically equivalent due to reflection symmetry. As there are no other nuclei with spin, magnetic equivalence is obvious. The hydrogen nuclei within a methyl group of hexa-methyl benzene (middle) are chemically equivalent. Due to rotational symmetry, all methyl groups are chemically equivalent. Again, magnetic equivalence is given due to the lack of other nuclei. A more complicated situation can be found in p-chlorotoluene (right). All nuclei within the methyl group are magnetically equivalent. Due to a reflection symmetry two pairs of chemically equivalent nuclei (red and blue) can be found. These nuclei, however, couple differently to their respective neighbors, and thus, are not magnetically equivalent.

This means that for some simple molecules, including water, internal coupling does not affect the time evolution of the magnetization at all.

Rotating frame Hamiltonian

The time dependence of the Hamiltonian, introduced by the RF field, impedes calculations. Thus, it is convenient to rewrite it in a reference frame, rotating with the RF field frequency. Therefore, the complete rotating frame Hamiltonian can be written as

$$\mathcal{H}_{\text{rot}} = -\hbar \sum_i \Omega_i \hat{I}_{i,z} + \hbar\gamma \vec{G}(t)\vec{r}\hat{I}_z + 2\pi\hbar \sum_{(i,j)} J_{i,j} \hat{\vec{I}}_i \hat{\vec{I}}_j + \hbar\gamma B_1(t) \left(\cos\phi(t)\hat{I}_x + \sin\phi(t)\hat{I}_y\right), \quad (2.14)$$

where $\Omega_i = \omega_i - \omega_{\text{RF}}$ is the rotating frame frequency of the i-th nucleus. Formula 2.14 is the Hamiltonian that describes every NMR experiment. The Hamiltonian, and consequently the time evolution of the magnetization, depends on molecular properties (Ω_i, $J_{i,j}$) and the gradient and RF-pulse scheme that is applied.

2.1.2 Coherences and Relaxation

It is convenient to use the spin density formalism to describe the temporal evolution of the magnetization. Additionally, decoherence effects, which have not been considered so far, drive the spin system towards thermal equilibrium.

Spin density formalism and Liouville-von Neumann equation

In an NMR experiment, the magnetization of the subject is measured. As the magnetization is proportional to the expectation value of the nuclear spin operator, its time evolution is given by

$$\vec{M}(t) \propto \left\langle \hat{\vec{I}} \right\rangle (t) = \text{Trace}(\sigma(t)\hat{\vec{I}}), \quad (2.15)$$

where $\sigma(t)$ is the density matrix of the spin system. The time evolution of the density matrix is described by the Liouville- von Neumann equation

$$\frac{\partial\sigma}{\partial t} = -\frac{i}{\hbar}\left[\hat{H}, \sigma\right]. \quad (2.16)$$

The nuclear spin Hamiltonian, as described in formula 2.14, is time-dependent. However, in numerical calculations, it will be considered point-wise constant. Thus, the density matrix can iteratively be calculated by

$$\sigma_{n+1}(\vec{r}) = \exp(-i\mathcal{H}(\vec{r})\Delta t/\hbar)\sigma_n(\vec{r})\exp(i\mathcal{H}(\vec{r})\Delta t/\hbar), \quad (2.17)$$

where Δt is the time between time points n and $n+1$. Due to the application of gradient fields, the density matrix is spatially dependent. Note that the density matrix of a spin system with N nuclei has dimension $2N \times 2N$, including every possible transition between the Zeeman states. The components of this matrix are called coherences, where the coherence order is determined by the number of creation operators minus the number of destruction operators needed to perform the transition.

The Pauli matrices form, in combination with the unity matrix, a basis for the single spin density matrix. The density matrix of an N nuclear spin system all combinations of N basis matrices, joined by Kronecker products. This allows for an alternative representation of the density matrix. For weakly coupled spin systems, a product operator formalism was developed [30]. In this representation, it is much easier to describe the time evolution of different spin families. Using a small set of rules, the time evolution of the spin density matrix can be calculated and expressed by product operators. For a three-spin system, some of the $4^3 = 64$ product operators are

$$\begin{aligned} I_{1,x} &:= \hat{I}_x \otimes \mathbf{1} \otimes \mathbf{1} \\ I_{1,x}I_{3,z} &:= \hat{I}_x \otimes \mathbf{1} \otimes \hat{I}_{3,z} \\ I_{1,x}I_{2,x}I_{3,z} &:= \hat{I}_x \otimes \hat{I}_{2,x} \otimes \hat{I}_{3,z}. \end{aligned} \tag{2.18}$$

As a shorthand notation, unity matrices and the Kronecker products are dropped. In order to discriminate between spin operators, and product operators the latter is written without the hat symbol in this thesis. The coherence order for the product operator coherence is given by the number of transversal spin operators needed to construct the product operator. Note that every product operator coherence with coherence order p contains multiple transitional coherences with coherence order $\pm p$.

The GABA spin system can be approximately described as an IS_2 system (see chapter 2.4.2). This means that one spin of the spin family I weakly couples to two magnetically equivalent spins of the spin family S.

Relaxation

Decoherence effects drive the spin system towards thermal equilibrium. An excellent overview of these processes can be found in [31]. However, in this thesis, relaxation is not considered in quantum mechanical calculations. Instead, exponential decay of the transversal magnetization is assumed. Analogously, the longitudinal magnetization is assumed to approach its equilibrium value in an exponential manner. Therefore,

$$\begin{aligned} M_z(t) - M_0 &\propto \exp(-t/T_1) \\ M_{xy}(t) &\propto \exp(-t/T_2), \end{aligned} \tag{2.19}$$

where T_1 and T_2 are the longitudinal and transversal relaxation times, respectively. These relaxation parameters depend not only on molecular properties but also on the properties of the surrounding tissue. Therefore, they are often used as a source of contrast in MR imaging.

In a real experiment, the magnetic field will not be perfectly homogeneous, especially in a high external field (see chapter 2.5.1). This will lead to dephasing and consequently, an increased apparent transversal relaxation $T_2^* < T_2$.

2.1.3 Classical description of the magnetization evolution

In the absence of coupling processes, the evolution of the magnetization can be described classically by the Bloch equation [32]

$$\frac{\mathrm{d}M}{\mathrm{d}t} = \gamma\vec{M} \times \vec{B} - \begin{pmatrix} M_x/T_2 \\ M_y/T_2 \\ (M_z - M_0)/T_1 \end{pmatrix}. \tag{2.20}$$

The external field $\vec{B}$ contains the static field B_0 and the RF field B_1, as well as gradient fields. Without the RF field, the magnetization precesses around the axis of the external field, with the frequency $\omega_0 = \gamma B_0$. Using gradients, a linear spatial dependence can be introduced to the precession frequency. An on-resonant RF pulse will flip the magnetization by the flip angle

$$\alpha = \int \mathrm{d}t \underbrace{\gamma B_1(t)}_{\omega_1} \tag{2.21}$$

around the axis where the pulse is applied in. For off-resonant pulses, analytic solutions only exist in a subset of RF pulse shapes. However, within the small tip-angle approximation [33] the frequency response function is proportional to the Fourier transform of the RF pulse. Using the effective frequency $\omega_e = \sqrt{\Omega^2 + \omega_1^2}$, the effect of a rectangular pulse with a frequency offset Ω can be written as a rotation matrix acting on the magnetization vector [34]

$$\mathbf{R}(\Omega, \omega_1, t) = \begin{pmatrix} \omega_1/\omega_e + \Omega/\omega_e \cos(\omega_e t) & \Omega/\omega_e \sin(\omega t) & \Omega\omega_1/\omega_e^2(1 - \cos(\omega_e t)) \\ -\Omega/\omega_e \sin(\omega t) & \cos(\omega_e t) & \omega_1/\omega_e \sin(\omega_e t) \\ \Omega\omega_1/\omega_e^2(1 - \cos(\omega_e t)) & \omega_1/\omega_e \sin(\omega_e t) & \Omega^2/\omega_e^2 + \omega_1^2/\omega_e^2 \cos(\omega_e t) \end{pmatrix} \tag{2.22}$$

An arbitrary phase θ can be introduced to the pulse, modifying the rotation matrix to

$$\mathbf{R}(\Omega, \omega_1, \theta, t) = \mathbf{R}_z(\theta)\mathbf{R}(\Omega, \omega_1, t)\mathbf{R}_z(-\theta), \tag{2.23}$$

where $\mathbf{R}_z(\theta)$ denotes the rotation matrix that rotates a vector by the angle θ around the z-axis. Analogous to the quantum-mechanical description, more complex pulses can be simulated by assuming a piece-wise constant RF-field. Thus, any given RF pulse can be simulated by the consecutive application of the rotation matrix defined in formula 2.23.

2.2 Single-voxel NMR spectroscopy

Single-voxel spectroscopy (SVS) aims to measure the concentration of chemical compounds within a predefined region. When applied to the brain, multiple metabolites can be measured. As the spins of all nuclei contribute to the magnetization, all metabolites' signals are measured simultaneously. These signals can be discriminated by the molecule-dependent time evolution of magnetization.

2.2.1 NMR signal equation and acquisition

The changing magnetization of the subject induces currents in the receiver coil of the scanner. This current is proportional to the transversal magnetization. It is convenient to consider a complex transversal magnetization

$$M_{xy}(\vec{r},t) = M_x(\vec{r},t) + iM_y(\vec{r},t) \propto \left\langle \hat{I}_x \right\rangle (\vec{r},t) + i \left\langle \hat{I}_y \right\rangle (\vec{r},t). \tag{2.24}$$

However, the receiver cannot measure the magnetization space dependently. Instead, the integrated signal

$$S(t) \propto \int \mathrm{d}^3 r \, \rho(\vec{r}) M_{xy}(\vec{r},t) \tag{2.25}$$

is measured. Here, $\rho(\vec{r})$ is the coil sensitivity. Using quadrature, the signal is split into a real and imaginary components which are separately analyzed by an analog-to-digital converter (ADC). Due to this procedure, only $p = -1$ coherences can be measured. All coherences of all metabolites are measured simultaneously and decay with their respective T_2^*.

Modern MR scanners are equipped with array coils. Multiple coils measure the magnetization simultaneously, with vastly different sensitivity profiles, and the final measurement is a combination of these individually magnetization measurements. Following equation 2.25, the measured signal of the j-th coil is described as

$$S_j(t) \propto \int \mathrm{d}^3 \rho_j(\vec{r}) M_{xy}(\vec{r},t), \tag{2.26}$$

where ρ_j is the coil sensitivity of the individual coil. As the coil elements are placed around the head, their sensitivity profile is vastly different, and consequently, dominant coils depend on the measured brain regions.

In a single-voxel experiment, no gradient is applied during the signal acquisition. The dwell time t_{dwell}, which is the time between two individual ADC events, and the total time of signal acquisition t_{ADC} define the spectral bandwidth ν_{BW} and the frequency step $\Delta\nu$ via

$$\begin{aligned} t_{\mathrm{dwell}} \cdot \nu_{\mathrm{BW}} &= 1 \\ t_{\mathrm{ADC}} \cdot \Delta\nu &= 1. \end{aligned} \tag{2.27}$$

2.2.2 Free induction decay

The free induction decay (FID) is the simplest possible Fourier-based NMR approach. An RF pulse is used to create transversal magnetization, and the signal acquisition starts directly afterwards. This method was introduced in 1966 by Richard Ernst [3].

Assuming an IS_2 system and an RF pulse in x-direction, the resulting density matrix transforms to

$$I_z \rightarrow I_y \tag{2.28}$$

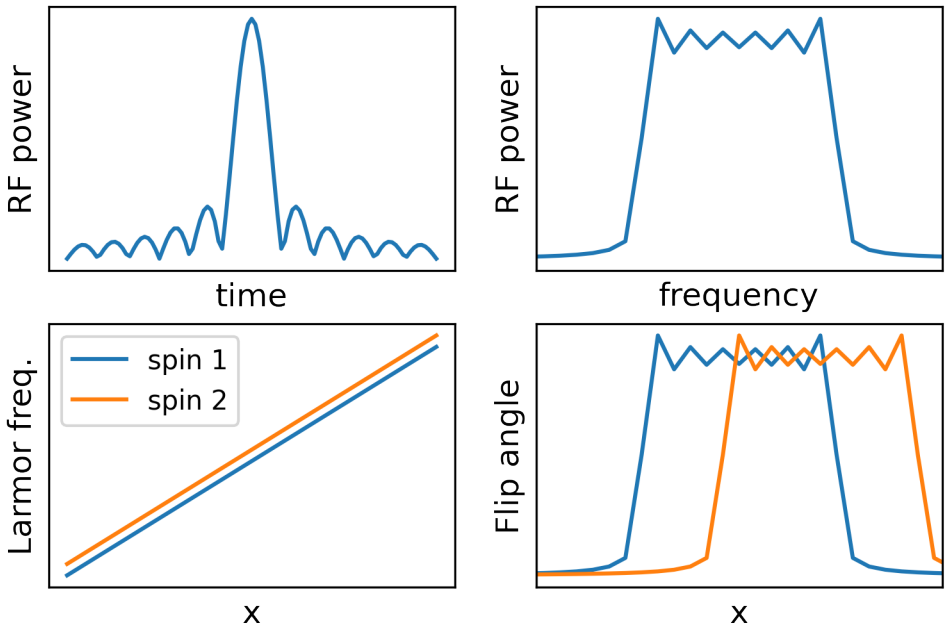

Figure 2.2: Depiction of the slice selection process. A sinc-shaped RF-pulse (top left) is applied to the spin ensemble. This pulse has an approximately rectangular frequency response (top right). Simultaneously, a magnetic field gradient causes the Larmor frequency to linearly depend on one spatial dimension (bottom left). There will be a different frequency offset for each spin type, depicted in blue and orange. These two effects cause a slice selective flip angle. Note, that there is a shift in spatial position of the selected slice.

at the start of the acquisition. Note that the starting condition is I_z, meaning the net magnetization is aligned to the z-axis.

2.2.3 Slice Selection and Chemical shift displacement

It is possible to manipulate spins within only a slice of the subject. This is called slice selection and was introduced by Mansfield in 1976 [35]. Two things are required. First, a gradient field that causes the Larmor frequency to be linearly spatially dependent and, secondly, an RF pulse with an approximately rectangular frequency response. Following small the tip-angle approximation, this is achieved by a sinc-shaped pulse. An excitation pulse will introduce a spatially linear phase in the magnetization. This phase must be compensated for, using a subsequent rephase gradient. High flip angle pulses are usually numerically optimized.

Figure 2.2 shows the working principle of the slice selection. The edges of the selected slice are defined by the frequency span of the RF pulse. The position of the slice is displaced for different nuclei due to their chemical shift. The slice thickness x_{thick} and the chemical shift displacement Δ_x are given by

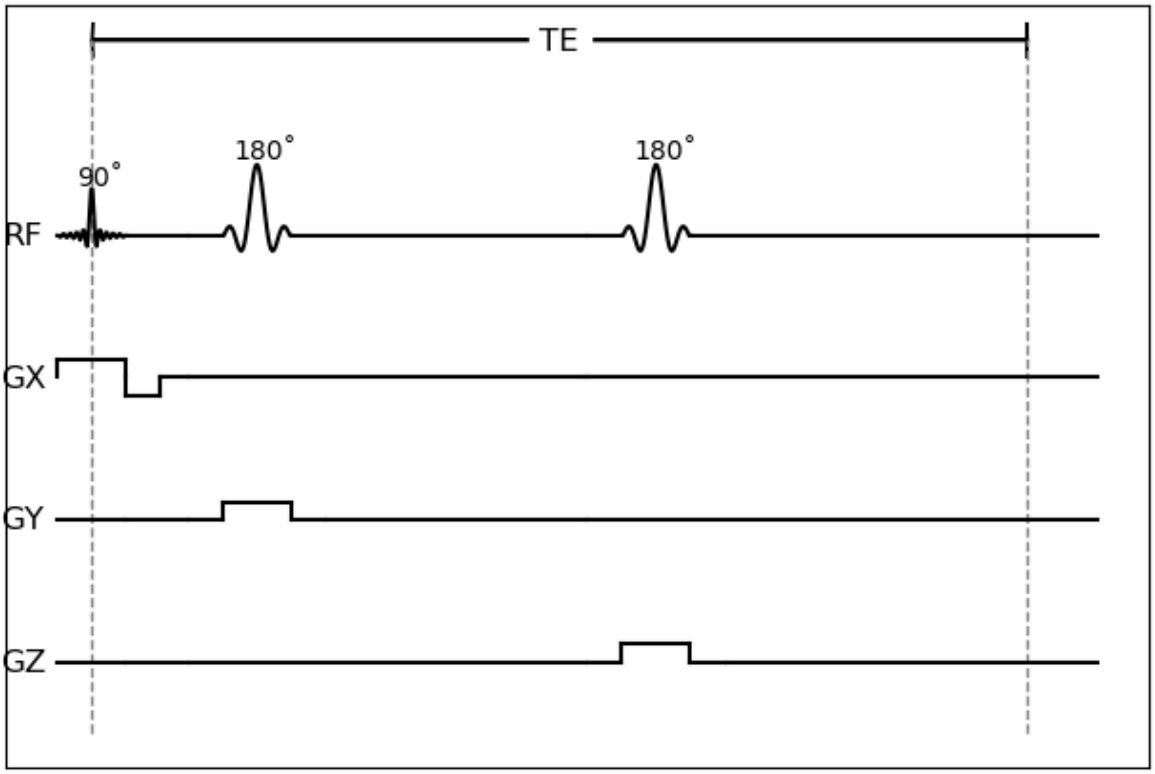

Figure 2.3: Diagram of the PRESS pulse sequence, Two slice selective refocusing pulse follow a slice selective excitation pulse. Thus, a voxel in the intersection of the three orthogonal slices is selected

$$\begin{aligned} x_{\text{thick}} &= \frac{2\pi\Delta\nu_{\text{RF}}}{\gamma G} \text{ and} \\ \Delta_x &= \frac{2\pi\Delta\nu_{\text{CS}}}{\gamma G}, \end{aligned} \tag{2.29}$$

where $\Delta\nu_{\text{RF}}$ is the pulse bandwidth, $\Delta\nu_{\text{CS}}$ the difference in Larmor frequency between the two nuclei, and G the gradient strength. As the Larmor frequency increases with higher field strength, the chemical shift displacement also increases.

2.2.4 Point Resolved Spectroscopy

Point Resolved Spectroscopy (PRESS) is a method for localized spectroscopy and was introduced in 1986 [36]. Three slice selective RF pulses are applied successively, selecting orthogonal slices. A sequence diagram can be found in figure 2.3.

Its working principle is most easily explained classically. The excitation pulse creates transversal magnetization, which begins to dephase. Using a 180° pulse, the phase of the magnetization is inverted, causing a rephasing of the magnetization. This creates a spin echo and

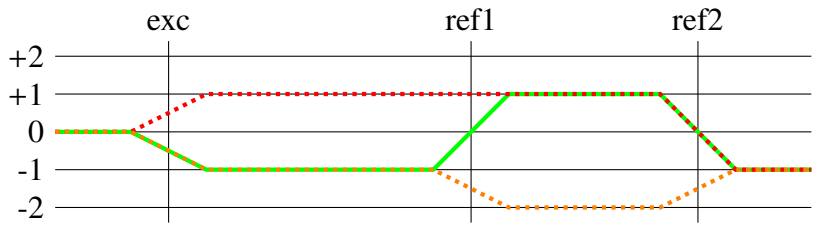

Figure 2.4: Possible coherence pathway during a PRESS sequence. In green, the wanted coherence pathway is depicted. The excitation pulse creates coherences of order ±1 (only -1 shown). Both refocusing pulses invert the coherence order. The red dotted line shows an unwanted coherence pathway. After the excitation pulse, +1 coherences are created. The coherence remains unaffected by the excitation pulse and is inverted by the second refocusing pulse. Outside the spectroscopic voxel, this coherence pathway would exist even in a perfect sequence. The orange dotted line depicts a coherence pathway, which only exist in an imperfect sequence

afterwards, the magnetization dephases again. This is inverted once again and in the moment of the second echo, data acquisition starts. These pulses are called refocusing pulses. This time evolution of the magnetization is only experienced by spins within the intersection of all three slices. Consequently, the signal from a cuboid voxel is selected. For an IS_2 system, one gets

$$I_z \rightarrow -\cos^2(2\pi T_E J) I_y + 4\sin^2(\pi T_E J) I_y S_{1,z} S_{2,z} + 2\cos(\pi T_E J)\sin(\pi T_E J)(I_x S_{1,z} + I_x S_{2,z}), \quad (2.30)$$

where T_E is the echo time, which is the time between the excitation pulse and the measured echo. As the magnetization is prepared in different coherences, depending on the echo time, different resonance shapes can be realized. Note that, in the case of GABA, the magnetization evolution of the S nuclei cannot accurately be described using an IS_2 model.

2.2.5 Coherence pathway selection

The calculation of the resonance shape assumes perfect pulses and focuses only on the spins within the region of interest. However, in a real experiment, spins from outside the region of interest will contribute to the measured magnetization. Furthermore, pulse imperfections, especially in the presence of B_1 inhomogeneities, will lead to unwanted coherence even inside the region of interest.

Within the product operator formalism, the coherence order can only be changed by an RF pulse [30]. A perfect 90° pulse changes the coherence order by 1, while a perfect 180° inverts the coherence order. Figure 2.4 depicts some possible coherence pathways in a PRESS experiment. All coherence pathways start at 0, as there is no transverse magnetization, and end with -1, as all other coherences are removed by the quadrature measurement. Next to the wanted coherence pathway (green), other coherences might add signal, corrupting the spectroscopic measurement.

Two main methods for coherence pathway selection exist. Phase cycling [37] and spoiler gradients [38]. Phase cycling splits the measurements into several subspectra. In each subspectrum, the phases of the pulses φ_i are different. This introduces a phase of the measured

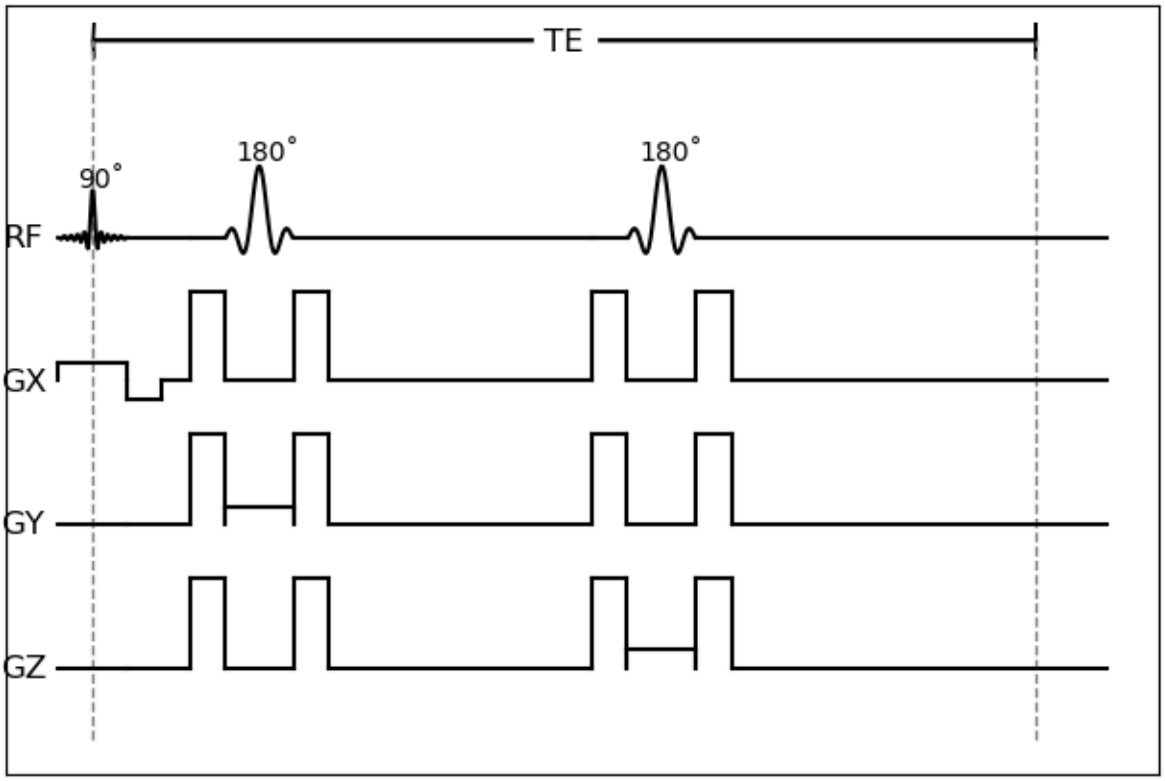

Figure 2.5: Sequence diagram PRESS, including coherence pathway selection. This is performed by symmetrically placing gradient pulses around the refocusing pulses.

magnetization $\Delta\varphi$, dependent on the change of coherence order Δp_i as

$$\Delta\varphi = \Delta p_i \varphi_i. \tag{2.31}$$

If phase cycling is applied correctly, the signal of the wanted coherence pathway adds up constructively, while the signals of all other coherence pathways add up destructively when the signals of all subspectra are combined.

Spoiler gradients take a different approach. Gradient pulses between the RF pulses introduce a position and coherence order dependent phase

$$\Delta\varphi_i(\vec{x}) = p_i \gamma \int \mathrm{d}t \vec{G}(t)\vec{x}. \tag{2.32}$$

The phases introduced by all spoiler gradients cancel each other for the wanted coherence pathway, while remain position dependent for all others if the phase increments are placed correctly. The measured signal is proportional to the volume integral magnetization (see formula 2.25). Thus, the signal of unwanted coherences cancels. Figure 2.5 depicts a PRESS sequence with spoiler gradients.

2.2.6 Water suppression

During an ^{1}H NMR experiment, the signals of every hydrogen-containing chemical substance are measured simultaneously. Obviously, the water signal is the largest signal by several orders of magnitude and completely overshadows every other signal. Therefore, it is beneficial to suppress this signal. In this thesis, VAPOR [39] is used, which is an adaption of the WET technique [40], that is less affected by B_1 and B_0 inhomogeneities.

The technique is based on selectively exciting the water resonance prior to the spectroscopic sequence. Small bandwidth excitation pulses are applied to the water resonance, followed by a dephasing gradient. Pulses with two different flip angles are used and the time between these pulses is numerically optimized such that at the time of the excitation pulse the water resonance contributes as little as possible to the net magnetization [39].

2.2.7 MEGA-PRESS

MEGA-PRESS is a modification of the PRESS sequence that contains a pair of MEGA pulses, which are named after their inventors, Mescher and Garwood [19]. These pulses are applied spectrally selective to a certain resonance within the molecule and have a flip angle of 180°. Due to coupling mechanisms, the time evolutions of the magnetization of other resonances are affected. This is called J-editing. During a MEGA-PRESS experiment, two sub-spectra are acquired. One with enabled editing pulses (edit-on) and one without (edit-off). Resonances without a coupling partner, which is affected by the editing pulse vanish by subtracting both subspectra.

A sequence diagram is depicted in Figure 2.6. Two MEGA pulses are added to the PRESS sequence. Here, pulse timing is important for optimal function. The time between the editing pulses should be half the echo time, and they need to be placed symmetrically around the last refocusing pulse. If these conditions are fulfilled, the magnetization of an IS_2 system can be described by

$$I_z \rightarrow I_y \tag{2.33}$$

in the edit-on subspectrum. As the edit-off acquisition is unaffected by the editing pulses, the magnetization is identical in a PRESS and a MEGA-PRESS sequence. To maximize the difference signal, the echo time is set to $T_E = 1/(2J)$. Thus, the magnetization in the edit-off case can be described as

$$I_z \rightarrow I_y S_{1,z} S_{2,z}. \tag{2.34}$$

In the case of GABA, the 1.89 ppm resonance is exposed to the MEGA pulse, and the 3.01 ppm resonance is coupled to this. Therefore, the 3.01 ppm resonance behaves differently in both subspectra. The overlapping creatine resonance, however, is not affected by J-editing and, thus, vanishes in the subtraction.

MEGA pulses can additionally be used as an additional water suppression technique [19]. The crusher gradient scheme is created such that resonances, directly inverted by the editing pulses, are removed. By using dual-band editing pulses, one band is tuned to the GABA resonance

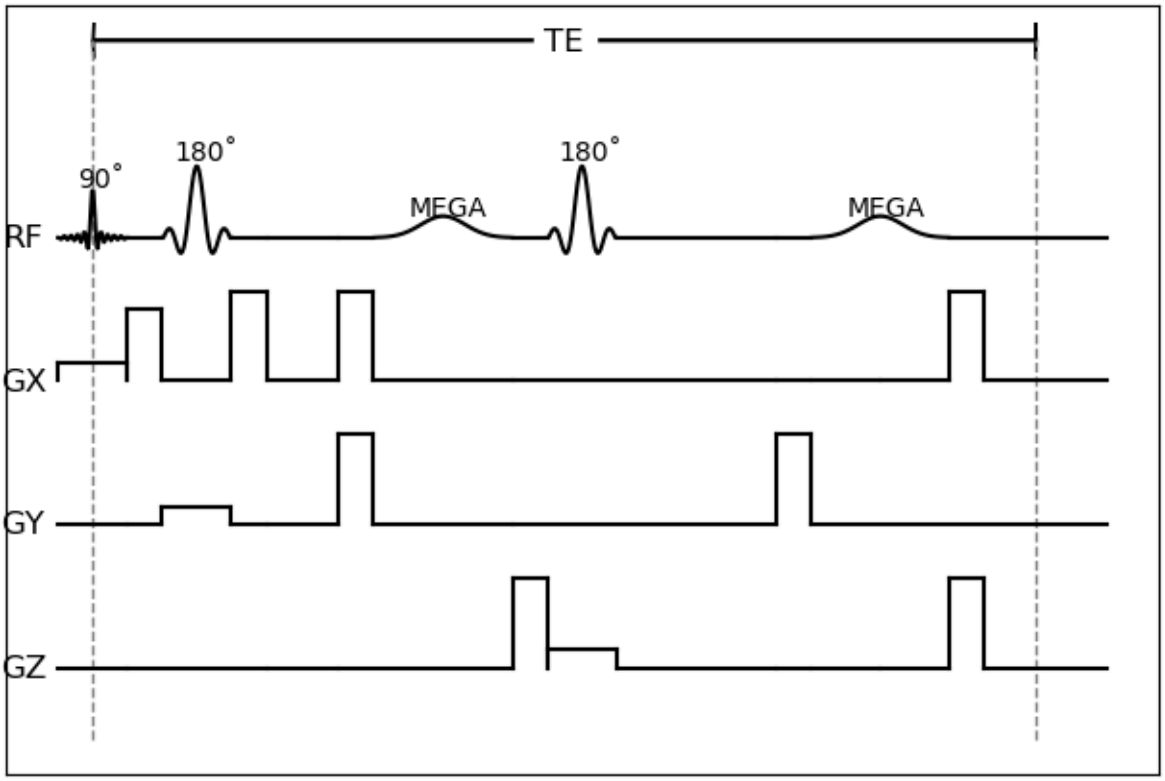

Figure 2.6: Sequence diagram of a MEGA-PRESS sequence. MEGA pulses are included around the last refocusing pulse

to perform J-editing while the other band is on-resonant to the water resonance to suppress its signal.

In *J*-editing GABA experiments, the region of interest of the 3.01 ppm resonance can be divided into four compartments that all experience different magnetization evolution, depending on the refocusing profile of the 1.89 ppm resonance. The first compartment is influenced by both refocusing pulses, the second one only by the first refocusing, the third compartment is only influenced by the second pulse, and, finally, the fourth compartment is influenced by neither pulse. This 4-compartment artifact [41] minimizes the efficiency of the editing signal.

2.2.8 Adiabatic Full Passages

Adiabatic pulses [42, 43] can perform broadband, B_1 insensitive magnetization inversions by utilizing amplitude and frequency modulation. Their working principle can best be explained using the effective field [44].

The effective field consists of a longitudinal $\Omega_0(t)/\gamma = (\omega_0 - \omega_{\mathrm{RF}}(t))/\gamma$ and a transversal component $B_1(t)$. The orientation of this effective field is given by the angle

$$\alpha(t) = \arctan2(\gamma B_1(t), \Omega_0(t)). \tag{2.35}$$

The magnetization rotates around this effective field. An adiabatic pulse starts with a large detuning causing an effective field parallel (or anti-parallel) to the main magnetic field. The detuning is slowly reduced, and consequently, the orientation of the effective field becomes perpendicular to the main magnetic field. Afterwards, the pulse frequency is detuned further until the effective field stands anti-parallel (or parallel) on the external field. If this rotation is slow enough, meaning the adiabatic condition

$$\kappa = \left| \frac{\dot{\alpha}(t)}{\gamma B_1(t)} \right| << 1 \tag{2.36}$$

is fulfilled for all t the longitudinal magnetization is inverted after this pulse. The phase of the transversal magnetization depends non-linearly on the off-center frequency, rendering slice selective refocusing impossible [45]. However, this non-linearity can be compensated for by a second, identical pulse [45].

The most used adiabatic pulse is based on a hyperbolic secant [42, 43]. A more SAR-efficient version is the GOIA-WURST pulse [46] which uses a WURST-modulated [47] gradient pulse and a gradient-modulated offset-independent adiabaticity (GOIA) RF-pulse [44]. This pulse is defined by

$$\begin{aligned} B_1(t) &= B_1^{\max}\left(1 - \left|\sin\left(\frac{\pi}{2}\frac{2t - T_p}{T_p}\right)\right|^n\right) \\ G(t) &= G^{\max}\left((1-f) + f\left|\sin\left(\frac{\pi}{2}\frac{2t - T_p}{T_p}\right)\right|^m\right) \\ \omega_{\mathrm{RF}}(t) &= \frac{G(t)}{Q}\int_0^t \frac{B_1(\tau)^2}{G(\tau)}\mathrm{d}\tau - \omega_c, \end{aligned} \tag{2.37}$$

where ω_c is the center frequency of the pulse and Q must be defined such that the frequency sweep covers the bandwidth of the pulse. 5 parameters can be chosen freely. Namely, the strength of the gradient drop f, the GOIA exponents (n, m) and the pulse bandwidth (indirectly defined via Q), and the maximal B_1 amplitude.

2.2.9 MEGA-sLASER

Due to the higher Larmor frequency, the chemical shift, and by extension, the 4-compartment artifact, becomes more problematic at 7 Tesla. Therefore, sequences exploiting adiabatic pulses have been proposed. Most notably, the semiLASER sequence [48], which uses a classical excitation pulse and two pairs of adiabatic refocusing pulses.

The MEGA-sLASER [49] sequence incorporates J-editing into semiLASER. Figure 2.7 shows the sequence diagram, including the crusher gradient scheme that is used for coherence pathway selection. The pulse timing follows the original implementation presented in [49]. Using the product operator formalism, the magnetization of a weakly coupled IS_2-system is prepared in exactly the same states as presented in chapter 2.2.7, including the 4-compartment artifact.

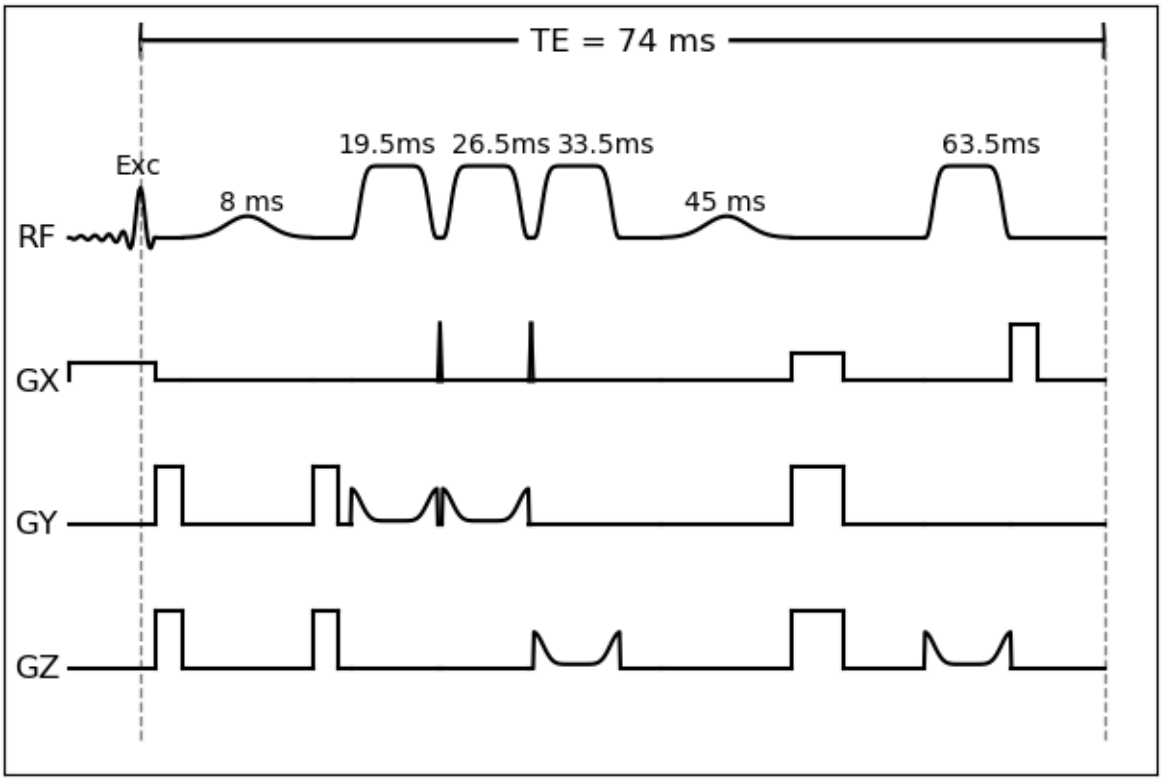

Figure 2.7: Sequence diagram of the used MEGA-sLASER sequence. An asymmetric excitation pulse is followed by two pairs of slice-selective adiabatic refocusing pulses. Dual-band MEGA pulses are placed between the excitation and the first refocusing pulse, as well as in between the second pair of refocusing pulses. The pulse timing is shown above the respective pulses.

Normally, in an NMR experiment, multiple repetitions are performed. Due to finite T_1, the longitudinal magnetization has not completely relaxed when the subsequent excitation pulse is played out. This limits the longitudinal magnetization at the start of each MEGA-sLASER sequence depending on the repetition time T_R. After a couple of repetitions, a steady-state transversal magnetization M_{ss}, directly after the excitation pulse is described by [3, 50]:

$$M_{ss} = \frac{(1 - E_1)\sin\varphi}{1 - E_1\cos\varphi}, \text{ with } E_1 = \exp\left(\frac{T_1}{T_R}\right), \tag{2.38}$$

Note that this formula is not only valid for MEGA-sLASER sequences but all sequences mentioned in this thesis.

2.2.10 Macro-molecular correction

The creatine signal that overlaps with the GABA signal is removed by subtracting both subspectra. However, this is not the case for some macromolecular resonances. Coupling between macromolecular resonances at 1.72 ppm and 3.00 ppm is present [51]. The 1.72 ppm resonance

is affected by the editing pulse. Therefore, the 3.00 ppm resonance overlaps with the GABA resonance in the difference spectrum.

By placing the frequencies of the editing pulses symmetrically around the 1.72 ppm resonance, the macromolecular contamination of the GABA signal can be minimized [52]. The GABA signal remains unaffected by the editing pulse, while the contaminating macromolecular resonance is editing with the same efficiency in the edit-on and edit-off subspectra. Thus, the signal vanishes in the difference. However, this method significantly reduces the reproducibility of GABA quantification [53].

2.3 Magnetic Resonance Spectroscopic Imaging

Magnetic resonance imaging (MRSI) combines MR spectroscopy with techniques from MR imaging. This allows for measuring the spatial distribution of the concentrations of the metabolites.

2.3.1 Signal equation and *k*-space

Using gradient pulses, a position-dependent phase can be enforced on the magnetization. As only coherence with the order of -1 can be measured, the spatial distribution of the magnetization is

$$M(\vec{r}) = M_0(\vec{r}) \exp\left(-i\vec{r} \underbrace{\int \mathrm{d}t\gamma\vec{G}(t)}_{\vec{k}}\right) = M_0(\vec{r}) \exp\left(-i\vec{k}\vec{r}\right), \tag{2.39}$$

where $M_0(\vec{r})$ is the magnetization without these gradient pulses. However, as explained in chapter 2.2.1, the receiver does not measure the spatial distribution of the magnetization. Following formula 2.25, the measured signal as function of $\vec{k}$ is given by

$$S(\vec{k}, t) = \int \mathrm{d}^3 r M_0(\vec{r}, t)\rho(\vec{r}) \exp\left(-i\vec{k}\vec{r}\right). \tag{2.40}$$

Interestingly, this is the very definition of the inverse Fourier transform of the spatial distribution of the magnetization, weighted by the coil sensitivity. Therefore, the spatial distribution of the magnetization can be inferred by Fourier transforming $S(\vec{k}, t)$. Consequently, the task in MR imaging is to sample the signal in the complete *k*-space. MR imaging can also be applied in only two spatial dimensions. By selectively exciting a slice and perform *k*-space sampling only within this slice.

Due to the connection via Fourier transformation, there are simple connections between the dimensions of the volume, which is reconstructed and the measured *k*-space. The reconstructed volume is called field of view (FoV) from now on. The size of the field of view is given by the inverse of the spacing between the *k* space points Δk while the number of voxels is identical in both spaces.

2.3.2 Phase encoded MRSI

Phase encoded MRSI adds gradients to the measurement sequence and acquires a spectrum for each required k-space point [54]. During the data acquisition, no gradient is played out. Image reconstruction can be performed for each time point individually.

This method is usually rather slow because only one k-space point can be measured for each excitation. Only a small number of k-space points can be acquired in reasonable measurement time, limiting the achievable resolution. However, combined with an FID-based approach, which can be performed with a very short repetition time, a very high resolution can be achieved using this approach [55].

2.3.3 Echo-Planar Spectroscopic imaging

Echo-Planar Spectroscopic imaging (EPSI) [13] is a technique that speeds up the k-space sampling by not measuring one k-space point per excitation but a k-space line. This method is based on Echo-Planar Imaging which was introduced by Mansfield in 1977 [56].

In one spatial direction (phase direction), a phase encoding gradient is used to select the k-space line that is to be sampled in that excitation. In the other direction (read direction) a prephase gradient ensures $k_r = -k_r^{\max}$ at the beginning of the readout. Data acquisition is performed during the flattop time of a trapezoid gradient pulse for each point of the k space line, such that at the end of the flat-top time $k_r = +k_r^{\max}$ is fulfilled. Afterwards, the k-space line is sampled again using an inverted gradient pulse. Note that this sampling is performed in reverse order. This process is repeated for each time point. This is shown in Figure 2.8.

While this method is much faster compared to phase-encoded MRSI, it does aggravate image reconstruction. The time points in which the signal is sampled vary along the readout direction. During this time difference, the spin system does evolve. Furthermore, to ensure high spectral resolution, the k-space sampling has to be fast. Therefore, high gradient strength and, thus, steep gradient slopes have to be implemented. This causes eddy currents within all conducting parts of the scanner. These problems have to be tackled using data processing which will be explained in more detail in chapter 3.1.2.

2.4 NMR spectroscopy of the human brain

In an NMR experiment, the magnetization of the subject is measured. All resonances of all chemical compounds contribute to this. Multiple compounds, including numerous brain metabolites, are detectable in the human brain using hydrogen spectroscopy. The exact resonance shapes depend on the molecule and the measurement sequence. Therefore, similar molecules often lead to similar resonance shapes. A complete spectrum can be seen in Figure 2.9.

2.4.1 The main metabolites

In an MR spectrum from healthy human brain tissue, three singlet peaks are prominent when no J-editing is performed. These peaks arise from the main metabolites NAA, creatine, and

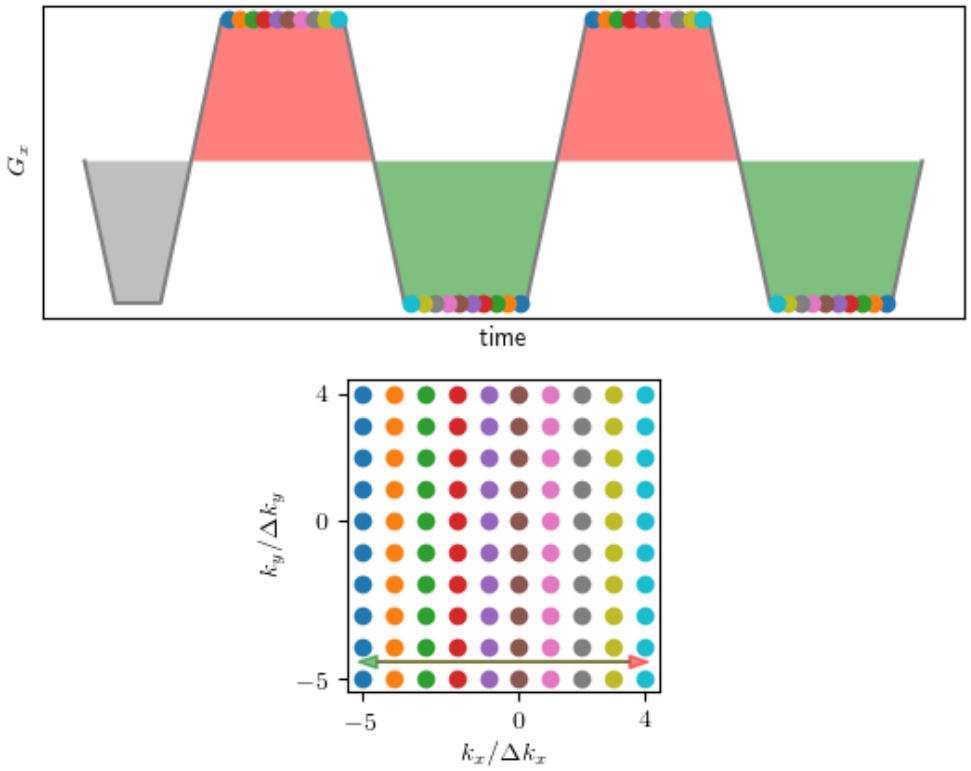

Figure 2.8: Diagram of an EPSI readout. A prephase gradient (gray) prepares the k-space at $-k_{\max}$. During a readout gradient (red), one k-space line is sampled. By inverting the readout gradient (green), the same k-space line is sampled again for a second FID point. This process repeats until the FID is completely sampled.

choline. However, none of these peaks arises from a single metabolite.

The choline signal is composed of the signals of phosphocholine (PCho, 3.208 ppm) and glycerophosphocholine (GPC, 3.212 ppm). The creatine signal (Cr, 3.027 ppm) overlaps with the phosphocreatine (PCr, 3.029) signal. Similarly, the N-Acetylaspartic acid (NAA) signal (2.008 ppm) overlaps with the N-Acetylaspartylglutamic acid (NAAG) (2.042 ppm). Due to the high spectral dispersion of ultra-high field spectroscopy, these resonances are partially resolved in Figure 2.9, where the NAAG resonance is visible as a bump on the flank of the NAA resonance. As a consequence of the substantial overlap, the signal strength total choline (PCho), total creatine (TCr), and total NAA (tNAA) is calculated. All resonance frequencies are taken from the TARQUIN source code [10, 57].

The largest peak in healthy human brain tissue is caused by NAA. While the exact role of NAA is still disputed, its concentration can be linked to many pathologies and is often interpreted as a non-specific marker of neuronal health [58, 59]. Creatine, and phosphocreatine in particular, play an important role in the energy consumption of the brain [60]. Because of its relatively stable concentration, TCr is often used as a reference compound, and other metabolic

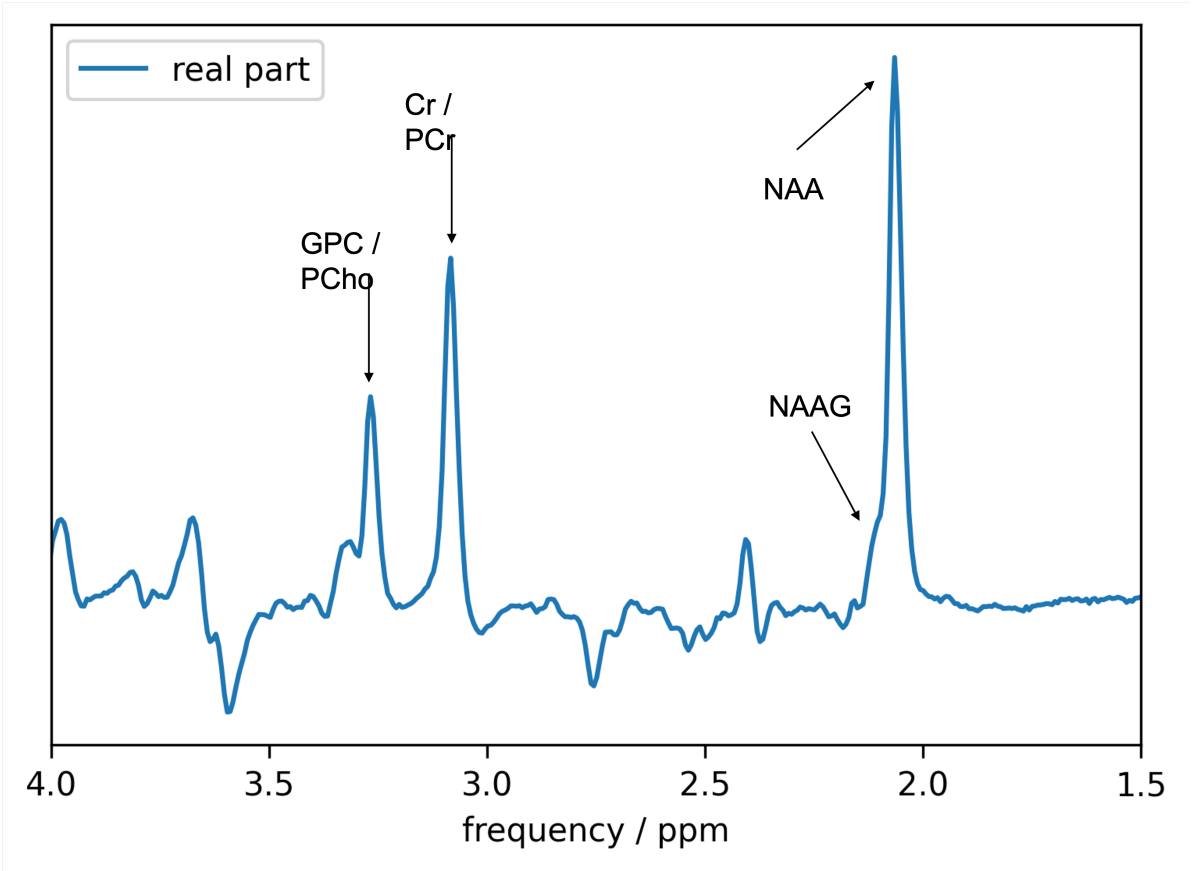

Figure 2.9: Real part of a measured *in vivo* edit-off spectrum MEGA-sLASER spectrum acquired in the posterior cingulate cortex. The singlet resonances of the main metabolites are labeled.

concentrations are given in fractions of TCr signal. It is important to note that this assumption is by no means perfect [59]. The TCho signal correlates with the cell density in the VoI [61].

A very detailed description of the biological roles of multiple brain metabolites, including their synthesis and transportation processes can be found in [59].

2.4.2 GABA

In 1950 γ-amino butric acid (GABA) was first discovered in a mouse brain [62]. For decades GABA has been known as the dominant inhibitory neurotransmitter in the mammalian brain [14]. It can bind to two different kinds of neuronal GABA receptors [63]. $GABA_A$ receptors open Cl^- and $GABA_B$ open K^+ [63] channels at the neuronal membranes. This lowers the membrane potential and, thus, inhibits neurotransmission. More recently, it was discovered that GABA is also produced, accumulated, and released by glia cells, acting as a gliotransmitter [15].

Only a small portion of GABA molecules is responsible for synaptic activity, while the larger portion remains within the neuronal and astrocytic cells [64]. Concentration changes of synaptic GABA happen on a timescale of below 500 µs [65], which is lower than timescales in MRS.

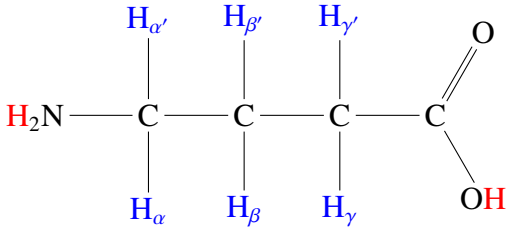

Figure 2.10: GABA molecule with NMR active hydrogen nuclei H_α, H_β, H_γ marked in blue. Hydrogen atoms marked in red are in rapid exchange and thus do not contribute to the NMR spectrum.

The aforementioned review paper [59] includes an excellent description of the biological role of GABA.

A wide variety of different pathologies could be linked to changes in GABA concentration, such as depression [18], Parkinson's disease [16], and epilepsy [66]. In a healthy human brain, the GABA concentration is higher in gray matter than in white matter [67, 68].

The GABA molecule and its NMR signal

A structural formula of the GABA molecule can be found in Figure 2.10. The hydrogen atoms within the outermost NH_2 and OOH group are in rapid chemical exchange with the surrounding water. Therefore, their nuclei do not give an NMR signal. This leaves three CH_2 groups. The hydrogen nuclei within these groups have different chemical shifts, and coupling between them is present. As explained in chapter 2.1.1, J-coupling is strongly distance dependent. Therefore, the coupling between H_α and H_γ can be omitted. The nuclei are approximately magnetically equivalent within their respective group.

In Table 2.1 the resonance frequencies and coupling constants, measured by three different groups, are summarized. The resonance frequencies are in excellent agreement. The measured coupling strengths, however, differ significantly. Furthermore, only one group included coupling between nuclei within the same group. In all simulations in this thesis, the GABA NMR parameters found by Near et al [69] were used.

GABA editing

The GABA molecule can be approximated as a weakly coupled spin system, where the product operator approach is applicable. As there is no coupling between H_α and H_γ nuclei, their time evolution is independent of each other. For the same reason, the time evolution of both H_α nuclei is independent. Thus, it is sufficient for the time evolution of the H_α spin to treat GABA as a spin system with one H_α and two H_β, which is referred to as an IS_2 spin system. Note that this will not yield to accurate calculation for the H_β nuclei.

Figure 2.11 depicts a simulated 3.01 ppm MEGA-sLASER GABA signal. On the left-hand side, the small coupling approximation is used, and the signal is described by formulae 2.33 (edit-on) and 2.34 (edit-off). In the edit-off case, a perfectly symmetric triplet signal arises, while the edit-on signal is described by a perfectly symmetric anti-phase triplet, which has inverted outer peaks. Therefore, the difference signal is reminiscent of a doublet signal and is,

	Near [69]	Kaiser [70]	Govindaraju [71]
δ_α / ppm	3.013	3.012	3.013
δ_β / ppm	1.888	1.888	1.889
δ_γ / ppm	2.284	2.284	2.284
$J_{\alpha\alpha'}$ / Hz	-14.062	0	0
$J_{\alpha\beta}$ / Hz	8.510	6.377	5.372
$J_{\alpha\beta'}$ / Hz	6.503	8.139	7.127
$J_{\alpha'\beta}$ / Hz	6.503	7.960	10.578
$J_{\alpha'\beta'}$ / Hz	8.510	7.495	6.982
$J_{\beta\beta'}$ / Hz	-15.000	0	0
$J_{\beta\gamma}$ / Hz	7.678	7.352	7.755
$J_{\beta\gamma'}$ / Hz	6.980	7.352	7.432
$J_{\beta'\gamma}$ / Hz	6.980	7.352	6.173
$J_{\beta'\gamma'}$ / Hz	7.678	7.352	7.933
$J_{\gamma\gamma'}$ / Hz	-15.938	0	0

Table 2.1: Resonance frequencies δ_i and coupling strengths J_{ij} within the GABA molecule measured by three different groups.

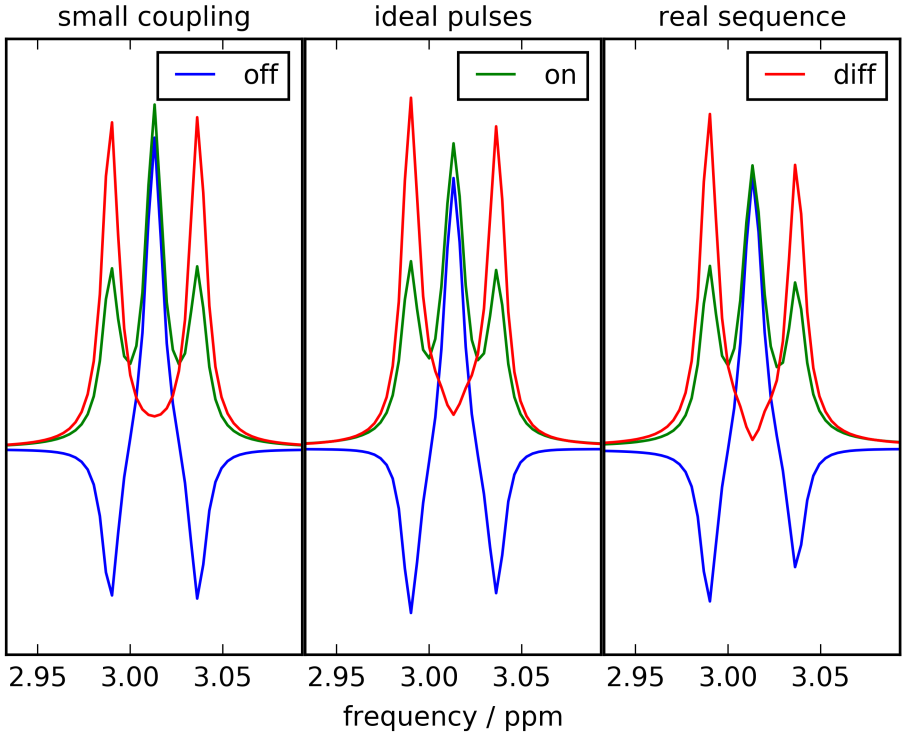

Figure 2.11: Simulated edit-off (blue), edit-on (green), and difference (red) spectra of the GABA 3.01 ppm resonance using (from left to right): The small coupling approximation and ideal pulses, the fully simulated GABA molecule and ideal pulses and the fully simulated GABA molecule and the pulse scheme that is used in this thesis. Each signal has a purely Lorentzian line shape with a 10 Hz line width.

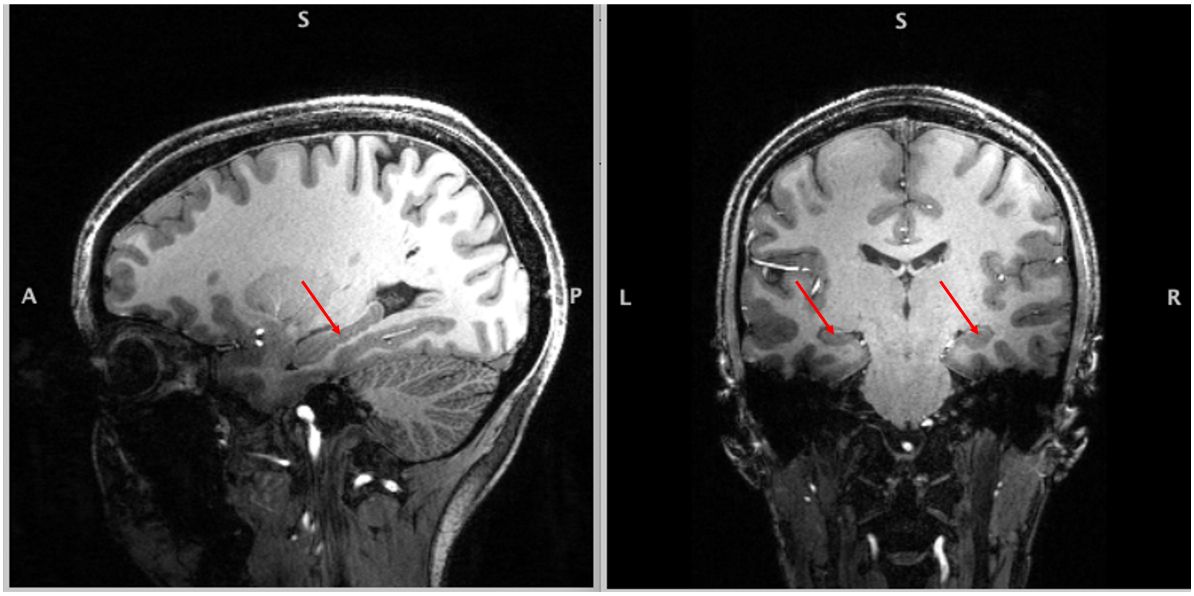

Figure 2.12: Sagital (left), and coronal (right) slice of a T_1 weighted MP-RAGE[74] acquisition of the human brain. The positions of the hippocampi are marked with green arrows

thus, referred to as a pseudo-doublet in this thesis. For the central plot, the complete GABA molecule was simulated, but the pulses were still treated as instantaneous rotations. The signals look very similar. The only difference is an asymmetry in the peak amplitudes. The right plot shows the GABA signal when the complete molecule and the pulses are simulated, which are used in this thesis. Again, the spectra look similar to the previous examples. However, a small drop in signal strength can be seen in the edit-on signal, indicating slightly imperfect editing efficiency. In summary, the spectra calculated with the product operator are a reasonable approximation for the MEGA-sLASER spectra. However, a full simulation will be needed for sequence optimization.

2.4.3 The hippocampus

The hippocampus is the main target region in this thesis. It plays a key role in memory and learning [72] and its function, and integrity can be linked to multiple pathologies, including Alzheimeir's disease [73]. Hippocampus atrophy, which is part of the aging process, is accelerated in Alzheimer's patients. Furthermore, the rate of atrophy correlates with the progression of cognitive impairment [73].

The hippocampus is an elongated grey matter structure in the human brain. In a T_1 weighted image, like the MP-RAGE [74] acquisition shown in Figure 2.12, it appears darker than the surrounding tissue. One hippocampus is present in each brain hemisphere. The positions of the hippocampi in the human brain are marked with red arrows. Air cavities within the sphenoid sinus and petrous bone create susceptibility discontinuities in the proximity of the hippocampi. These susceptibility discontinuities cause strong B_0 inhomogeneities and, consequently, a short T_2^*, which hampers NMR spectroscopy in this brain region.

Astrocytes, one type of glia cells, seem to play a pivotal role in Alzheimer's disease [75]. In special areas of the hippocampus, a large proportion of astrocytes contain GABA [76]. In animal models of Alzheimer's disease, these astrocytes increasingly release GABA [77, 78]. This makes the hippocampus a very interesting brain region for GABA spectroscopy. Because of the difficulties that arise from the short T_2^*, no J editing has previously been reported in the hippocampus.

2.5 Experimental challenges in ultra-high field *in-vivo* NMR spectroscopy

Due to stronger main magnetic field, the Larmor frequency increases from 123 Hz (3 Tesla) to 297 Hz (7 Tesla). This gives some benefits but is not without problems. Some of these are already mentioned in this thesis. The higher Larmor frequency leads to more signal, as the net-magnetization is larger (see formula 2.5). However, the same *RF* pulses cause a higher SAR compared to lower field strength (see formula 2.8). This limits the amounts of pulses that can be applied in a certain time. Furthermore, higher Larmor frequency increases the frequency between resonances but increases the CSDE.

2.5.1 Static field inhomogeneities

The main magnetic field and the RF-field are not perfectly homogeneous and become less homogeneous,the greater the field strength. This causes some challenges when using an ultra-high field MR scanner. In the following, the effects of these inhomogeneous fields and some compensation methods are briefly introduced.

B_1 and B_0 mapping

All compensation methods require estimates of the spatial distribution of the B_0 and B_1 field. The quantification of the field distributions cannot be inferred from a single measurement. Instead, both B_0 and B_1 maps require two measurements with different settings.

To measure the B_1 distribution two MR images using different nominal flip angles are necessary. The actual flip angle distribution, and therefore the B1, can be inferred from the two measured signal strengths. The DREAM sequence [79] combines both acquisitions within one excitation. The magnetization is measured after an excitation pulse. Afterwards, the magnetization is refocused by another pulse and measured again. From the signal intensity of these two measurements, the flip angle distribution can be inferred. In this thesis, a modified 3DREAM version [80] is used, which speeds up the acquisition by using a 3-dimensional readout. The B_1 amplitude can be adjusted by scaling the voltage applied to the transmit coil.

Similarly, the B_0 distribution can be inferred from two MR images conducted with different echo times. The different echo times result in a phase difference proportional to the offset frequency, which is caused by B_0 variations [81].

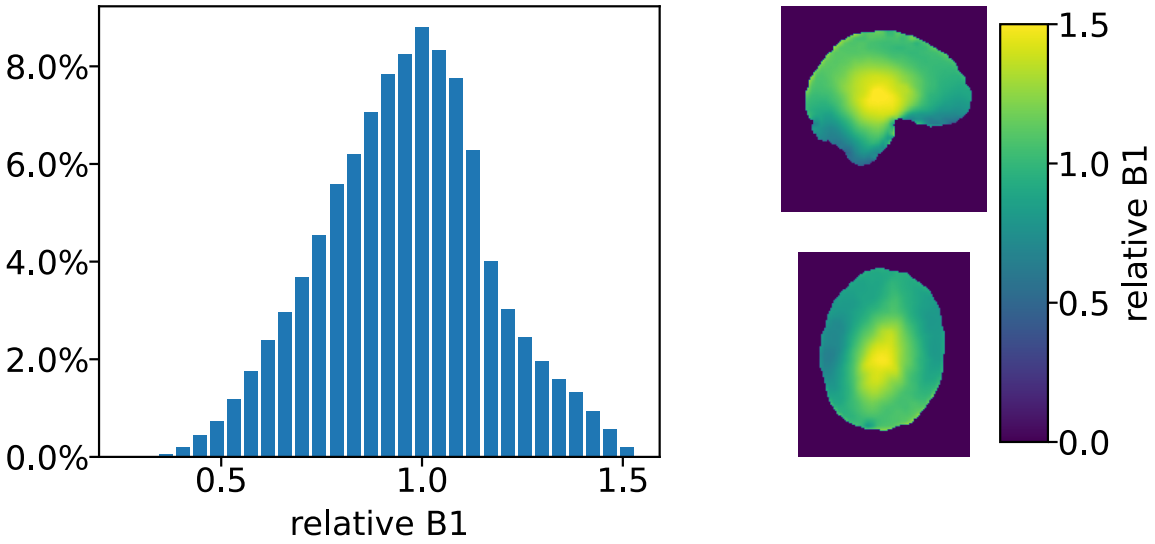

Figure 2.13: Histogram of the measured B_1 distribution within the human head (left). The B_1 amplitude can differ up to 50 % from its nominal value in some parts of the brain. A sagital (top right) and a coronal (bottom right) show the spatial distribution of the B_1 field. B_1 is elevated in the central parts of the brain and decreased in the outer parts.

B_1 inhomogeneity

The increased RF frequency that is required in a 7 Tesla scanner causes the wavelength to be shorter. Therefore, reflections occur, and a B_1 profile is created, which depends on the geometry of the subject. These effects are also present at lower field strengths but become more pronounced at 7 Tesla. Figure 2.13 shows this profile in one subject. In the central parts of the brain, the B_1 amplitude is highest, and the farther outside, the lower the B_1 amplitude. Variations of up to 50 % from the nominal value can be observed. In J-editing experiments, optimal editing efficiency can only be achieved if the flip angle of the editing pulses is correct. This means that the editing efficiency, and therefore the measured GABA signal will become spatially dependent.

In an MRSI experiment, the VoI is usually a large part of the brain, at least in two dimensions. Therefore, the inhomogeneous editing efficiency will introduce a systematic error in the GABA concentration estimates, which has to be compensated for (see chapter 3.3.1).

In an SVS experiment, the VoI is rather small, and the intra-voxel B_1 inhomogeneity is less problematic. The applied voltage to the RF coil can be adjusted to optimize the flip angle and thus, the editing efficiency. Low B_1 regions, like major parts of the cerebellum, require very high voltages. This causes significant SAR deposition. Consequently, these brain regions are hardly accessible with high SAR spectroscopic sequences, like semiLASER.

B_0 inhomogeneity and shimming

Various tissue types have different magnetic susceptibility. This creates B_0 field inhomogeneities. Obviously, these inhomogeneities increase in amplitude due to a higher external field. Intra-voxel field variation cause an accelerated signal decay. This leads to reduced SNR and line broadening and aggravates accurate quantification. As the voxel size in an SVS experiment is usually much larger compared to MRSI, SVS is more severely affected by this.

The inhomogeneous B_0 also causes the Larmor frequencies to be spatially dependent. In a J-editing experiment, the editing efficiency will depend on the Larmor frequency of the edited resonance. Therefore, large inter-voxel field variations will also introduce a systematic error in the GABA concentration estimate.

B_0 shimming is a method to counter these field inhomogeneities. Using specially designed shim coils, a magnetic field can be superposed to the main magnetic field, which minimizes the spatial variation of the magnetic field. If one assumes that the external field points perfectly in z-direction, the Laplace equation $\Delta B_z = 0$ has to be fulfilled. Consequently, the magnetization can be written as

$$B_z(\vec{r}) = \sum_{n=1}^{\infty} \sum_{m=-1}^{1} c_{n,m} Y_{n,m}(\phi, \theta) r^n, \tag{2.41}$$

where $Y_{n,m}$ are the tesseral spherical harmonics, a real valued representation of the spherical harmonics. Modern MR scanners are equipped with multiple shim coils that create magnetic fields, which point in z-direction and have an amplitude that is proportional to one $Y_{n,m}(\phi, \theta) r^n$. From a measured B_0 map, a set of $c_{n,m}$ that maximizes the field homogeneity. The voltage, which is applied to the individual shim coils, can be adapted to create the required correction field.

When multiple transmitter coils are used, B_1 shimming can be performed by adapting the phases and amplitudes of the individual coils to homogenize the B_1 field in a similar fashion. As only a single transmitter coil is used in this thesis, B_0 shimming will only be referred to as shimming from now on.

2.5.2 Dynamic field changes

Additional to static field inhomogeneities, magnetic fields can also change within small time-frames.

Subject-induced field fluctuation

Major rigid movement of the examined body part causes a shift of the region of interest, which cannot be compensated for using data processing techniques. However, as head movement is restricted within the scanner, this usually does not occur.

Minor movement of the subject causes field fluctuation. These movements include movements of body parts and physiological changes like heartbeat and respiration. Consequently, these fluctuations are inevitable to some extent. These field fluctuations can be compensated for during data processing, as explained in chapter 3.1.5.

Eddy currents

Switching of the gradient coils induces eddy currents in all conducting material of the scanner. These eddy currents create magnetic fields and, thus, disturb the main magnetic field. This disturbance is time-dependent and distorts the magnetization measurement. Modern MR-Scanners use a Scanner model to calculate the expected eddy currents of an MR sequence and compensate for their effects on the measured magnetization to some extent.

CHAPTER 3

Optimized data processing for *J*-edited GABA spectroscopy

3.1 Preprocessing

The metabolites' concentration can be inferred by fitting a data-fitting process called spectral quantification. In this thesis, all data processing steps that are performed beforehand are called preprocessing, and all processing steps that follow are called postprocessing.

3.1.1 Coil Combination

As explained in chapter 2.2.1, multiple individual coils are used to measure the magnetization of the subject. Multiple methods have been proposed to obtain the coil combined signal $S(t)$ by a linear combination of the individual coil signals $\vec{s}(t)$. In this thesis of these methods, Adaptively Optimized Combination (AOC) [82] is used, where

$$S(t) = \vec{w} \cdot \vec{s}(t), \text{ with } \vec{w} = \mathcal{N}^{-1}\vec{c}, \tag{3.1}$$

where $\mathcal{N}$ is the noise correlation matrix and $\vec{c}$ is the measured coil sensitivity. While $\mathcal{N}$ can easily be extracted from the spectroscopic data by selecting a spectral regime without any resonance, accurate measurements of the coil sensitivity require a water unsuppressed signal. AOC was shown to outperform other noise decorrelation methods [83].

3.1.2 Image reconstruction for EPSI

As explained in chapter 2.3.1, image space and k-space representation of the NMR signal are connected via Fourier transformation. This process is impaired by an EPSI sampling as the signal of each k-space point is measured with a different timing. Furthermore, the steep gradient slopes required in the k-space trajectory cause eddy currents which distort this trajectory. These problems can be overcome by shifting the center of mass of the k-space [84]. For each time point n, the center of mass is defined as

$$\begin{aligned} CM_x(n) &= \frac{\sum_{k_x,k_y} k_x |S(k_x,k_y,n)|}{\sum_{k_x,k_y} |S(k_x,k_y,n)|} \text{ and} \\ CM_y(n) &= \frac{\sum_{k_x,k_y} k_y |S(k_x,k_y,n)|}{\sum_{k_x,k_y} |S(k_x,k_y,n)|}. \end{aligned} \tag{3.2}$$

Using the Fourier shift theorem, the center of mass can be moved to the center of the k-space.

3.1.3 k-space filter

As only a finite number of k-space points are sampled, the k-space is truncated. Thus, the point spread function will contain side lobes. This effect can be removed by multiplying the data with a filter function that weights the central k-space points more strongly. It was shown that the hamming window function is optimal for this task [85] which is defined as

$$H(k) = 0.54 + 0.46 \cos\left(\frac{\pi k}{2k_{\max}}\right). \tag{3.3}$$

3.1.4 Eddy current compensation

Modern MR scanners are equipped with an automated compensation for eddy current, very efficiently removing their effects on the measured signal. Many recent MRS studies, including a recent large-scale study that aims for standardization of GABA spectroscopy at 3 Tesla [53], do not perform any additional compensation for eddy currents. However, additional eddy current compensation was necessary in this thesis.

Using a water reference scan with the very same gradient sequence, the effect of the eddy currents can be disentangled from the spectroscopic data [86]. Field distortions created by eddy currents are strongly time-dependent and thus create a non-linear phase evolution in the spectroscopic data. The water signal, however, contains only a single resonance. Therefore, every non-linear phase evolution is artificial. Multiplying the measured signal by

$$E(t) = \exp(-i \arg(S_{\text{wat}}(t))), \tag{3.4}$$

where $S_{\text{wat}}(t)$ is the coil combined water signal, removes the effect of eddy currents from the spectroscopic data. This process is exemplarily shown in Figure 3.1.

3.1.5 Frequency and Phase Adjustment

Subtle movements of the subject, including respiration, affect the phase and frequency of the signal of individual excitation. These variations can be compensated for by modifying the signal of the individual excitations $S_j(t)$ to

$$S_j^{\text{PFC}}(t) = S_j(t) \exp\Big(i(2\pi\nu_j t + \phi_j)\Big). \tag{3.5}$$

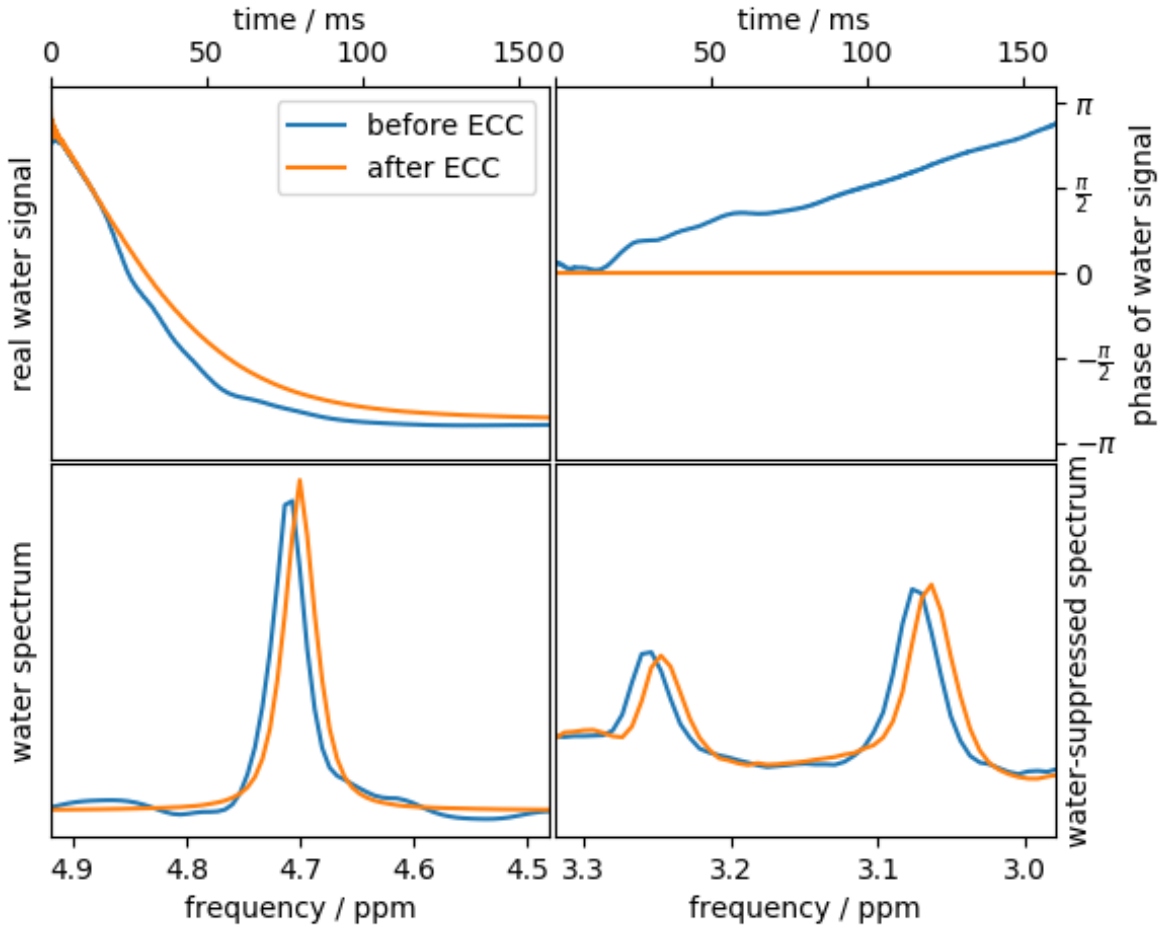

Figure 3.1: Principle of eddy current compensation. The blue and orange lines represent before and after ECC, respectively. The water signal (top left) shows a couple of bumps, which are removed by ECC. The origin of these bumps is a non-linear phase evolution which can be seen on the top right. This phase evolution line shape distortion in the water spectrum (bottom left). In the water-suppressed spectrum (bottom right), these distortions are more difficult to see.

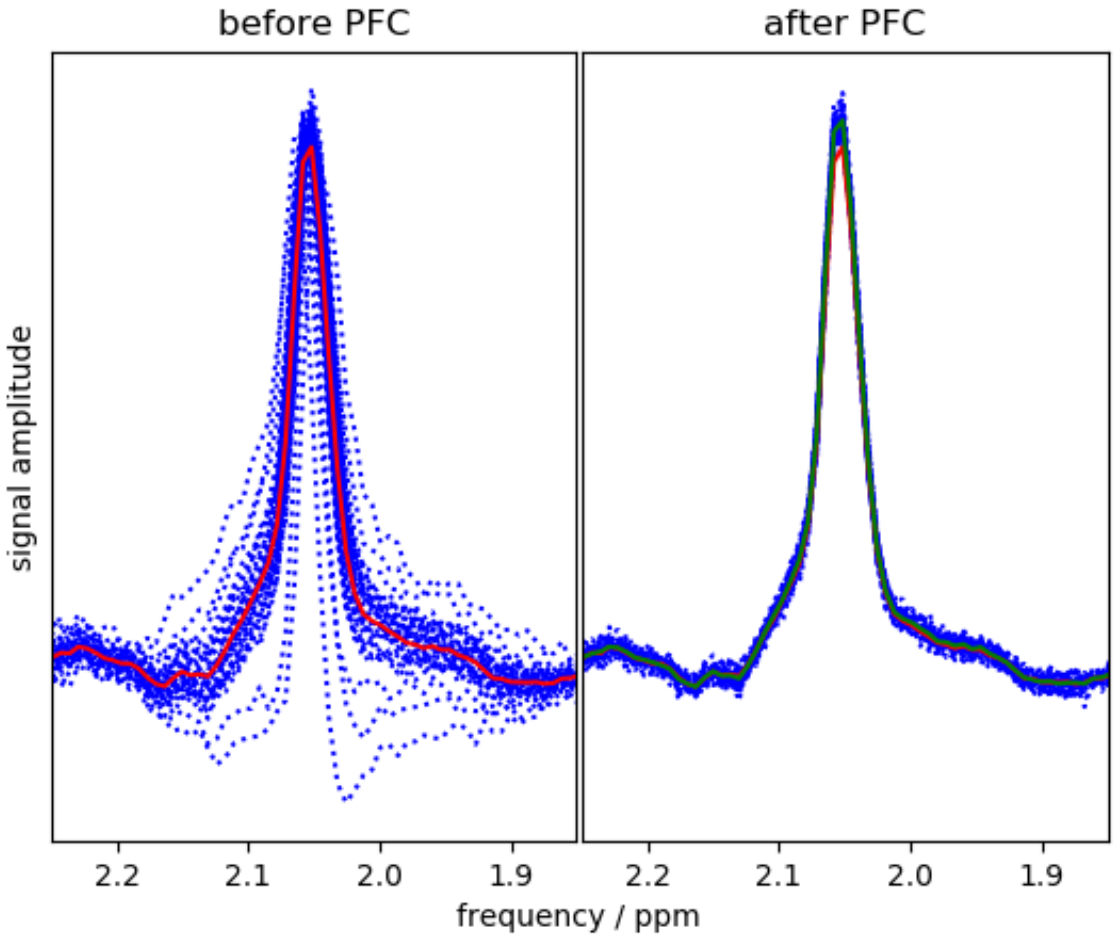

Figure 3.2: Principle of phase and frequency correction. In the left plot, the NAA resonance of individual excitations is shown with blue dotted lines. The average of these spectra is depicted in red. On the right-hand side, the phase and frequencies of the individual signal have been corrected. The average of the phase and frequency corrected spectra are depicted in green. In red, the average of the not corrected spectra is shown. Utilizing PFC, the SNR is boosted, and the line width becomes narrower.

This process is exemplarily shown in Figure 3.2. Multiple methods have been proposed to obtain each (ϕ_j, ν_j). Some used the residual water signal [87, 88] or additional measurements [89]. Another method is to fit a Lorentzian line shape of the creatine resonance of every excitation and thus obtain (ϕ_j, ν_j) [90].

Recently, spectral registration (SR) [91], which is a model-free approach, became the most commonly used method. Using a reference signal $R(t)$, the individual phase and frequency offset is calculated by solving the minimization problem

$$(\phi_j, \nu_j) = \underset{\phi,\nu}{\operatorname{argmin}} \|S_j^{\mathrm{PF}}(t, \phi, \nu) - R(t)\|_2. \tag{3.6}$$

In this thesis, two different types of reference signals are used. The averaged edit-off signal and the averaged edit-on signal can be used for the registration of respective excitations (SRind).

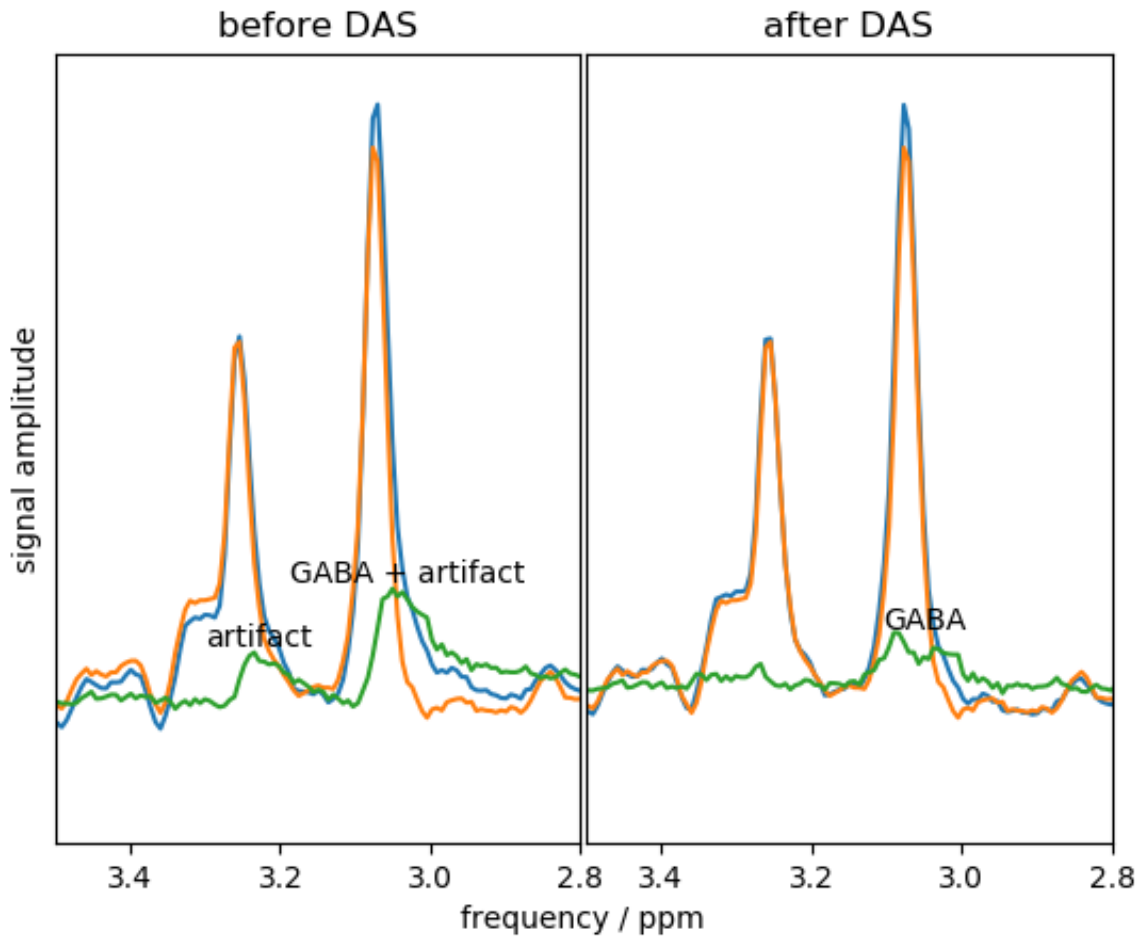

Figure 3.3: Principle of difference artifact suppression. On the left-hand side, a small frequency and phase difference between the edit-on and edit-off spectrum causes residual signal after subtraction. The residual choline signal is clearly visible. Residual creatine signal overlaps with the GABA signal and thus falsifies the GABA quantification. On the right-hand side, the phase and frequency difference is vanished. No residual choline signal is visible, indicating less residual creatine signal overlaps with the GABA signal.

Alternatively, the averaged edit-off signal is used as the reference for all excitations (SRmeo). Note that by bandpass filtering both the signal and the reference, a frequency span can be selected [91].

3.1.6 Difference Artifact Suppression

Difference artifacts arise from a phase or frequency mismatch of the two subspectra. This mismatch causes residual a creatine signal after the subtraction that cannot be separated from the GABA signal during spectral quantification. The phase and frequency of the edit-on signal are adapted analogously to 3.2 prior to the subtraction. This procedure is depicted in figure 3.3.

It is possible to use the spectral registration framework [91] to obtain the needed frequency

and phase ($\phi_{\text{on}}, \nu_{\text{on}}$). In order to perform spectral registration spectrally selectively, the frequency span (2.5 ppm,3.5 ppm) is selected. In this regime, the GABA signal is the only expected resonance in the difference. This spectral registration based difference artifact suppression will be referred to as DAS from now on. Difference optimization (DO) [22] is an alternative approach that uses a different minimization problem. Here, the phase and frequency offset is defined as

$$(\phi_{\text{on}}, \nu_{\text{on}}) = \underset{\phi,\nu}{\text{argmin}} \| S_{\text{on}}^{\text{PFC}}(t, \phi, \nu) - S_{\text{off}}(t) \|_1. \tag{3.7}$$

3.2 Spectral Quantification

In MR spectroscopy, the signals of all metabolites are measured simultaneously. In order to measure the concentrations of the individual metabolites, these signals have to be disentangled, which is a non-trivial task. There are multiple existing toolboxes available, most notably LCModel [7], Gannet [8], jMRUI [9], and TARQUIN [10]. All of these were shown to give comparably reproducible GABA concentrations using MEGA-PRESS at 3 Tesla [92].

In this thesis, TARQUIN is used, which is an open-source C++ toolbox that performs fully automated spectral quantification. A quantum mechanical simulation of an idealized measurement sequence leads to the expected signals of each metabolite, which are used as a basis function. A linear combination of these basis functions is fitted to the measured data that defines the concentration of each metabolite. The signal decay is modeled by an individual Lorentzian decay for each metabolite and a joined Gaussian decay, that mimics the effect of inter-voxel field inhomogeneities.

This simulation is not performed for the quantification of the difference signal. Here, all signals are treated as singlet signals. Furthermore, not all metabolites are considered, but only those who have an expected signal. The GABA signal is modeled by two individually treated signals. In this thesis, an adaptation of this model is used, where more co-edited signals are modeled by additional resonances (2.5 ppm, 2.66 ppm, 2.68 ppm).

Several parameters can be adjusted. This includes n_s, which is the first time point that is considered in the fitting process, and β_s, which is the starting value of the strength of the Gaussian decay.

3.3 Post Processing

While data processing is completed for an SVS experiment, this does not hold true for spectroscopic imaging. The inhomogeneous B_1 distribution renders further processing necessary.

3.3.1 Editing efficiency compensation

Due to the large region of interest in an MRSI experiment, the B_1 variations will be substantial, especially at 7 Tesla. Due to the adiabatic pulses, the semiLASER sequence itself does not suffer severely from these variations. However, this does not hold true for the editing pulses.

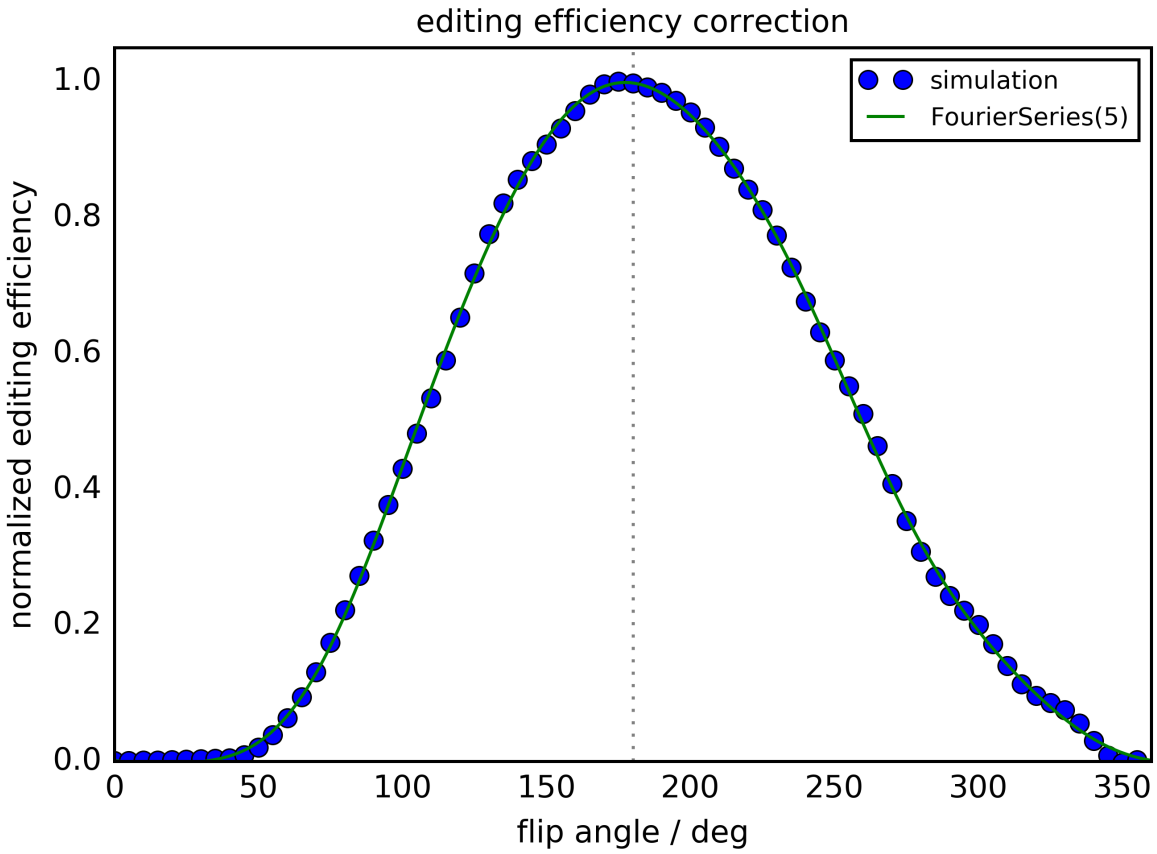

Figure 3.4: Simulated editing efficiency as a function of B_1 amplitude. As the flip angle varies from 180°, the editing efficiency drops. A 4th-order Fourier series was calculated to obtain the editing efficiency correction factor as a continuous function of the flip angle.

As the editing efficiency depends on the flip angle, a systematic, position-dependent error is introduced to the edit-on and thus, the difference signal. The compensation method used in this thesis is similar to the method presented in [93].

For various nominal flip angles between 0 ° and 360 °, the GABA signal was simulated in a 2-dimensional 20x20 grid. The size of the grid was matched to the region of interest to also include edge effects. Perfect excitation was assumed, and the true gradient scheme was used in the imaging plane. The signal was afterwards averaged over the grid, and the editing efficiency was defined as the sum of the real part of the GABA 3.01 ppm signal. A 4th-order Fourier series describes the editing efficiency continuously as a function of the flip angle $\eta_{\text{edit}}(\phi)$. This function is shown in figure 3.4.

An additional measurement is needed to obtain the local flip angle. From a B_1 map, the mean flip angle in each voxel ϕ can be inferred, and an editing efficiency map $\eta_{\text{edit}}(\vec{r})$ can be defined. Thus, the corrected GABA concentration is given by

$$c^{\text{cor}}_{\text{GABA}}(\vec{r}) = \frac{c_{\text{GABA}}(\vec{r})}{\eta_{\text{edit}}(\vec{r})}. \tag{3.8}$$

3.4 Quality Assessment

Quality assessment (QA) is an integral part of MR spectroscopy. Prior to automated quality assessment methods, a visual inspection of all spectra is carried out. This is important to check for any artifacts, like spurious echoes and difference artifacts, that are not easily detectable by automated processes.

Due to the very high SNR of the water resonance, its signal is an obvious choice for quantitative QA. The most straightforward quality metrics are T_2^* and the FWHM. Due to the inevitable presence of line shape distortions, T_2^* is here defined as the time point in which the absolute water signal drops below $1/e$ of its maximum value. Similarly, the FWHM is defined as the time between the frequencies at which the absolute value drops below half of its maximum value.

The water signal is measured separately from the spectroscopic data. Thus, a QA based on the water-suppressed data is generally preferred. However, two main problems arise. First, the SNR is much smaller compared to the water signal, and second, multiple resonances are measured simultaneously. Therefore, the QA is based on the fit obtained during spectral quantification. TARQUIN automatically outputs the FWHM of the most prominent resonance, which arises from the NAA signal in healthy brain tissue. Furthermore, it gives the Cramer-Rao lower bounds (CRLB) for the concentration of each metabolite. Minimal quality requirements are usually defined by an FWHM < 0.1 ppm [94–96], while concentration measures with CRLB $> 50\%$ are considered unreliable [95, 96].

3.5 Summary

The complete data processing routine developed in this thesis is depicted in Figure 3.5 for both SVS and EPSI experiments. The analysis of SVS experiments does not require any additional measurement. In the first step, the raw data is read in and split into water-suppressed and water-unsuppressed data. From these, the noise correlation matrix and the coil sensitivity are calculated. Afterwards, the coil weights are calculated and applied to both the spectroscopic data and the water reference.

As there is only a single voxel, no image reconstruction is required. In the next step, the eddy current correction function is calculated from the water reference and applied to the spectroscopic data. This is followed by phase and frequency correction. The data is further split into edit-on and edit-off data. From these, the reference signals are also calculated, and phase and frequency variations are minimized prior to averaging the signals using spectral registration.

Afterwards, the summed edit-on signal is frequency and phase corrected with respect to the summed edit-off for subtraction artifact suppression. The final signals are then exported in the jMRUI data format [9]. These files are read in by TARQUIN, which performs spectral quantification.

Data processing is slightly more complex in the case of EPSI. An SVS experiment is performed on the same region of interest. From this, the coil weights are calculated and applied to the EPSI data, which is again split into water-suppressed and water-unsuppressed data.

Afterwards, the water-unsuppressed data is used to compensate for k-space distortions created by eddy currents. This correction is applied to both water-suppressed and water-unsuppressed

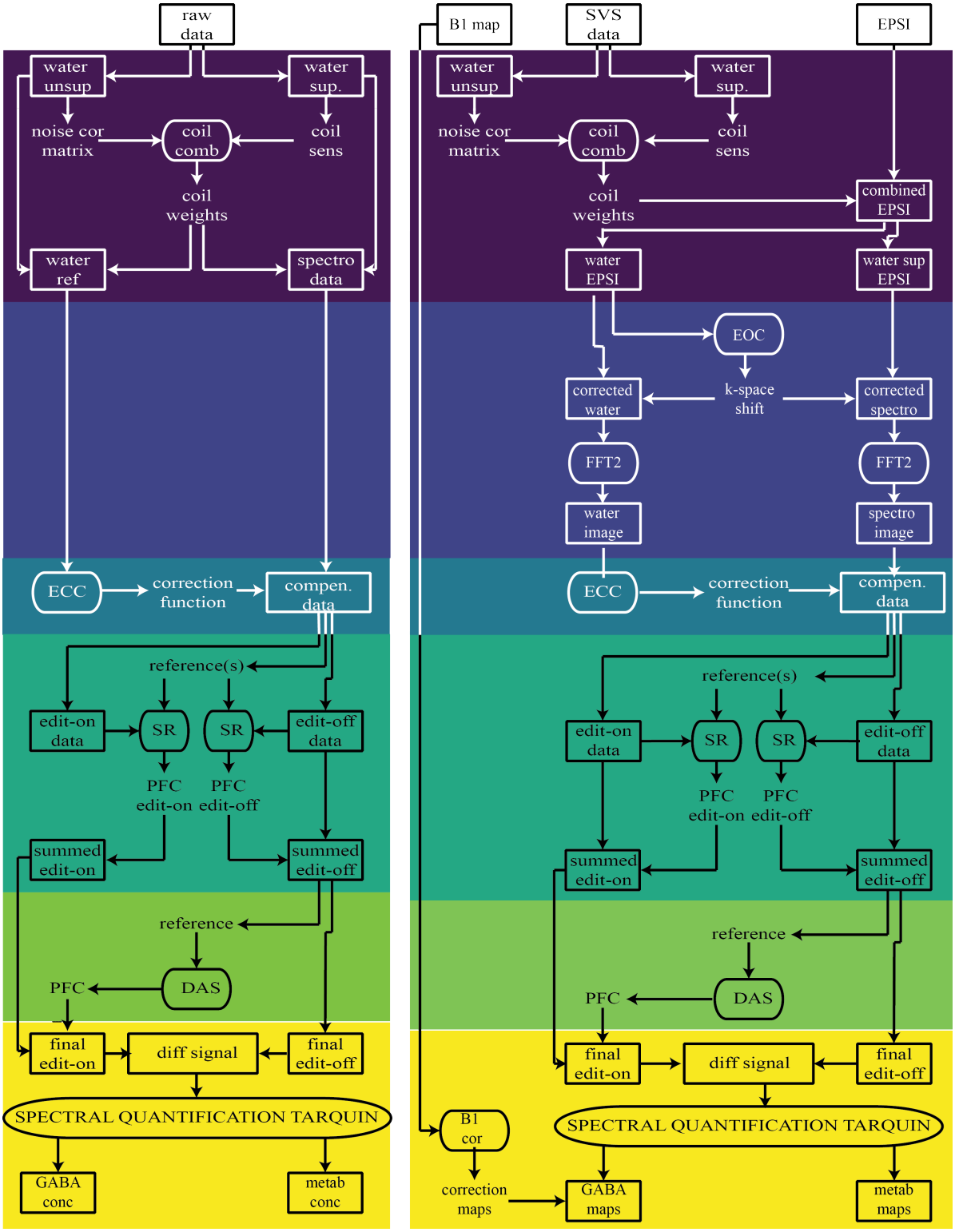

Figure 3.5: Complete Data processing pipelines for single voxel spectroscopy (left) and Echo Planar Imaging (right). The different colors represent different processing steps. From top to bottom: coil combination, image reconstruction, eddy current compensation, phase and frequency correction, difference artifact suppression, spectral quantification. Spectroscopic data is accompanied by a rectangular frame, algorithms by a rounded frame, and auxiliary variables remain unaccompanied.

data. Using a 2-dimensional Fourier transformation, image reconstruction is concluded.

Next, data processing is performed analogously to the SVS case for each voxel individually until a GABA map is calculated. Using the B_1 map, the GABA concentration of each voxel is corrected for editing efficiency variations caused by B_1 inhomogeneities. This, finally, leads to a corrected GABA map.

CHAPTER 4

Single-Voxel GABA spectroscopy at 7 Tesla

4.1 Motivation

Single-voxel spectroscopy (SVS) measures the time evolution of the magnetization of one cuboid region, the voxel of interest (VOI). Because of their different spectral properties, it is possible to discriminate chemical compounds and measure their concentrations. In the human brain, the concentration of numerous metabolites can be measured. This includes γ-amino butric acid (GABA), the main inhibitory neurotransmitter.

Because of the low concentration of GABA, relatively large VOIs have to be measured. Consequently, SVS is exceptionally prone to inter-voxel field inhomogeneities, which cause accelerated signal dephasing and, thus, reduced SNR. The main target region in this chapter is the hippocampus. This brain region is linked to memory processes, and changes in the hippocampus can be observed in Alzheimer's patients. As explained in chapter 2.4.3, the hippocampus lies in proximity to susceptibility discontinuities that introduce strong B_0 inhomogeneities. This makes the hippocampus a challenging region to do spectroscopy and requires a careful shimming process.

Two preparatory experiments will be described in this chapter. First, the RF pulses are optimized to increase the measured GABA signal using simulation. Next, the different shimming processes were tested to obtain a fast, reliable, and accurate homogenization of the B_0 field.

Finally, these optimizations are applied to *in-vivo* GABA spectroscopy in the hippocampus. In this part data processing is optimized to increase the reproducibility of hippocampus GABA spectroscopy as far as possible.

4.2 Experimental setup

All experiments in this, and the following, chapter were conducted with a 7T Magneton (Siemens Healthineers, Erlangen, Germany), utilizing a 32-channel head coil (Nova medical, Wilmington, USA). The gradient is equipped with an SC72 gradient system. This system allows a maximum

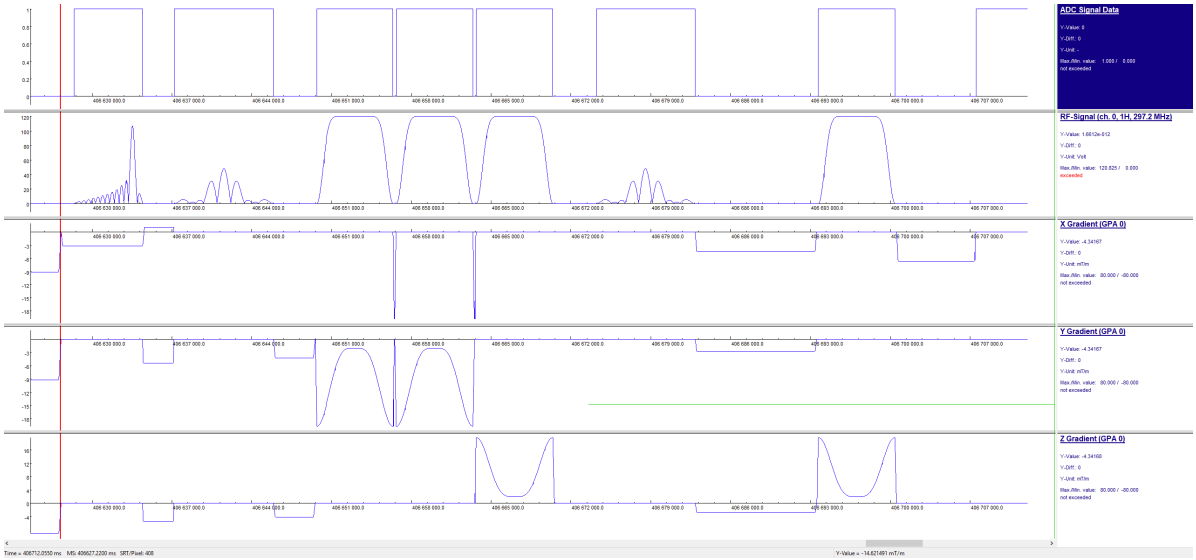

Figure 4.1: One repetition of a MEGA-sLASER sequence, simulated using the IDEA VB17 framework. The red line marks the end of the preceding water suppression module (not shown) and the beginning of the MEGA-sLASER sequence. The pulse timing follows the original MEGA-sLASER implementation [49].

nominal gradient strength of 70 mT/m and a maximal gradient slope rate of 200 mT/m. This gradient system is also used as the first-order coils for B_0 shimming. The scanner has further shim-coils for the 2nd order and four 3rd-order field components. Furthermore, SAR supervision is automatically performed by the scanner. The measured signal is eddy-current compensated using a scanner model.

Phantom measurements were performed in a self-made GABA phantom. A 500 ml PET bottle was filled with an aqueous GABA solution, following the GANNET recipe [97]. Human subjects were scanned in accordance with the local ethics committee, requiring written informed consent before each examination.

Sequence development was performed with the Siemens IDEA framework (version B17). This C++ based framework allows total control over the RF and gradient pulse sequence and can also be used to simulate the sequence. Figure 4.1 shows a screenshot of a simulated MEGA-sLASER measurement. The pulse timing is identical to the sequence diagram in figure 2.7. In the beginning parts of the final spoiler of the preceding VAPOR water suppression is visible. The red line marks the beginning of the sequence.

A vendor provided-asymmetric excitation pulse (*asym90exc*) is used as the excitation pulse. Refocusing is performed using GOIA-WURST pulses (see chapter 4.3.2). MEGA-editing is performed using small bandwidth dual-band pulses (see chapter 4.3.2). Note that figure 4.1 shows the pulse amplitude only and not the phase. The strong sine-like variations are caused by the beat of both frequencies. In between the pulses, spoiler gradients are played out for coherence pathway selection.

This sequence can also contain a water reference scan. In the very first repetition of the sequence, neither the VAPOR water suppression nor the MEGA-editing pulses are applied.

Consequently, a water unsuppressed spectrum is acquired with identical settings.

Not shown is the 16-step phase-cycling that is performed if the number of excitations is dividable by 16. The phases of the pulses and the readout can be found in table A.1 in the appendix. Note that the phase of the MEGA pulses remains unchanged during the phase cycle.

All pulses are implemented as a pulse object. Slice selection is performed by automatically shifting the resonance frequency according to the gradient strength. In the case of GOIA-WURST pulses, the gradient strength changes. The resulting change of center frequency is also automatically considered in the framework. An additional off-center frequency can be added to the pulses to change the center frequency to a certain resonance. As the MEGA-sLASER sequence will depend on the refocusing of the GABA 3.01 ppm and the 1.89 ppm, the center frequency will be set to 2.4 ppm for the refocusing and the excitation pulses. This causes a detuning of the GABA signal of around 181 Hz, while the water resonance is detuned by 683 Hz.

A semi-automated shim process is performed using a third-party tool (*WIP1441B*). This tool will be referred to as shimWIP during the course of this thesis. It contains a gradient echo (GRE) based B_0 mapping sequence and an automated script, that reads in the measured B_0 map and automatically calculates the required shim currents to optimally apply a correction field. This script optimizes the field homogeneity within a user defined, cuboid adjustment volume, that might differ from the voxel of interest. It is possible to use this method in a repetitive fashion by measuring a B_0 map, calculating the shim currents and measuring a new B_0 map using these updated shim currents. Although the scanner is equipped with some 3rd-order shim coils, the usage of these shim coils is optional. If the 3rd-order shim is activated, the script calculates the shim currents up to 2nd order. Afterwards, the 3rd-order shim currents can be calculated using an additional GUI.

4.3 Optimization of the acquisition sequence

4.3.1 Motivation

The MEGA-sLASER sequence contains different kinds of RF pulses. These pulses can be optimized in order to boost the available GABA signal and, thus, improve signal quantification. Both, the adiabatic refocusing pulses and the editing pulses are optimized based on simulated the GABA signal.

No optimization of the excitation pulse was performed, as the pulse shape is defined and the pulse duration is the only parameter, which can be varied in the sequence. The shorter the pulse, the higher its bandwidth. However, decreasing the pulse duration increases the required pulse amplitude, which is limited. A pulse duration of 4.2 ms was chosen in order to not reach this limit during hippocampus spectroscopy.

As explained in chapter 2.2.8, adiabatic pulses can be used to refocus the magnetization, independent of B_1, if a certain amplitude threshold is reached. However, finding this amplitude threshold is not obvious, especially for detuned RF frequencies. If this threshold is not reached, incomplete refocusing causes a loss of signal strength. If the RF-amplitude is set too high, unnecessarily high SAR deposition enforces a long repetition time and, consequently, a loss of signal.

pulse duration [ms]	pulse bandwidth [kHz]	pulse amplitude [μT]
3.5, 4	33.6 (1% CSDE)	integer
4.5, 5	16.8 (2% CSDE)	values
5.5, 6	11.1 (3% CSDE	between
6.5, 6.7	8.4 (4% CSDE)	0 and 24

Table 4.1: Parameter pool of adiabatic pulses during simulation of the GABA signal after an sLASER sequence, containing eight pulse durations, four pulse bandwidths, and 25 pulse amplitudes

The editing pulses are refocusing pulses, which should only perturb the spins of the GABA H_β nuclei (see chapter 2.2.7). Therefore, they have to be spectrally narrow. In an *in-vivo* experiment, the Larmor frequency slightly changes due to physiological changes, such as subtle movement or respiration. Thus, optimal editing pulses are immune to small frequency offsets. Inefficient editing causes a loss of signal. Moreover, a strong frequency dependence on the editing efficiency might cause systematic errors in the GABA concentration estimate caused by subject motion.

4.3.2 Methods

GOIA-WURST pulses

In this thesis, GOIA-WURST pulses were used for adiabatic refocusing. As explained in chapter 2.2.8, this pulse type has six free parameters, of which three are used uniformly in literature. For the optimization of the duration τ, the bandwidth $\Delta\nu_{\mathrm{RF}}$, and the maximal RF field amplitude B_1^{max} a classical simulation was used, which numerically solves the Bloch equation.

In this simulation, an accurate gradient scheme was used, and perfect excitation was assumed. As the pulse frequency in the used sequence is placed between the outermost GABA resonances, the GABA 3.01 resonance has a detuning of 181 Hz while the water resonance is detuned by 683 Hz. The magnetization at time T_E was simulated in a 200x200 points grid that matched the VOI by numerically solving the Bloch equation for each point in the grid. Relaxation effects were not considered. The signal strength is defined as the averaged transversal magnetization. Table 4.1 summarizes the simulated pulse settings.

Editing pulses

J-difference editing exploits internal coupling processes within the GABA molecule. As there is no classical description of this process, a quantum mechanical simulation is needed. Similarly to the simulation to calculate the editing efficiency in chapter 3.3.1, the pyGamma [98] framework was used.

Using the optimized GOIA-WURST pulses, the GABA edit-on and edit-off spectrum was calculated in a 20x20 pixel grid. Again, the signal was averaged over the grid, and the integrated signal of the 3.01 ppm difference signal was defined as editing efficiency. This procedure was repeated for various off-center frequencies between -0.5 ppm and +0.5 ppm, which is more than the expected frequency variation during an *in vivo* acquisition. Different types of pulses

were tested. Gaussian pulses are the most used editing pulses and were tested with different bandwidths. Siemens provides fat suppression pulses. These pulses are low-bandwidth slice selection pulses and have, thus, a more constant frequency response for low detuning.

Phantom validation

To validate the simulation results, experiments were performed in a GABA phantom. In addition to the optimized editing pulses, the optimized refocusing pulse duration and bandwidth were used, and pulse amplitudes between 5 μT and 18 μT were used. This experiment was performed for water and GABA. In the case of GABA, the complete MEGA-sLASER sequence was applied, while the water signal was extracted from a measurement with deactivated water suppression. A (2x2x2) cm^3 VOI was selected in the center of the phantom.

The signal amplitude is defined by the integrated signal of the absolute values of the water resonance and the GABA 3.01 ppm resonance, respectively. The water and GABA signals were additionally simulated using the same classical simulation, as for the GOIA pulse optimization. The amplitude of the measured values was scaled to the simulated values.

4.3.3 Results and Discussion

GOIA-WURST pulses

In Figure 4.2, the simulated GABA signal strength is depicted as a function of B_1^{max} for all tested pulse parameters. Qualitatively, the behavior is very similar for these parameters. For low B_1^{max} the signal is completely dispersed. Afterwards, the signal rises until a plateau is reached. However, the achievable maximal signal strength, as well as the needed B_1^{max} to reach this value, depends on the pulse setting.

This dependence is depicted in Figure 4.3. In the top plot, the maximal signal strength is shown as a function of pulse duration for all tested pulse bandwidths. The higher the bandwidth and the longer the pulse duration, the higher the maximal achievable GABA signal. The bottom plot shows the threshold B_1, which is defined as the B_1^{max} needed to achieve 95 % of the maximal amplitude. The threshold B_1 decreases for longer pulses and lower bandwidth.

These findings can easily be explained by the definition of κ in equation 2.36 in chapter 2.2.8. Longer pulse duration obviously leads to a slower change in the effective field, reducing κ and thus improving the adiabatic refocusing.

In contrast, high pulse bandwidth pulses require a faster frequency sweep and, thus, increase κ. Consequently, the adiabatic refocusing is impaired, and a reduced maximal achievable signal would be expected. However, as explained in chapter 2.2.8, the shape of the frequency swipe function is defined such that it is steeper the farther off-center the frequency is, reducing maximal κ. Because of the different resonance frequencies of GABA, the pulse frequency is detuned, which renders this reduction less effective. High bandwidth pulses are affected less severely by this off-center effect, and higher signals can be achieved with these pulses.

More B_1 amplitude is needed for higher bandwidth pulses to compensate for the steeper frequency sweep.

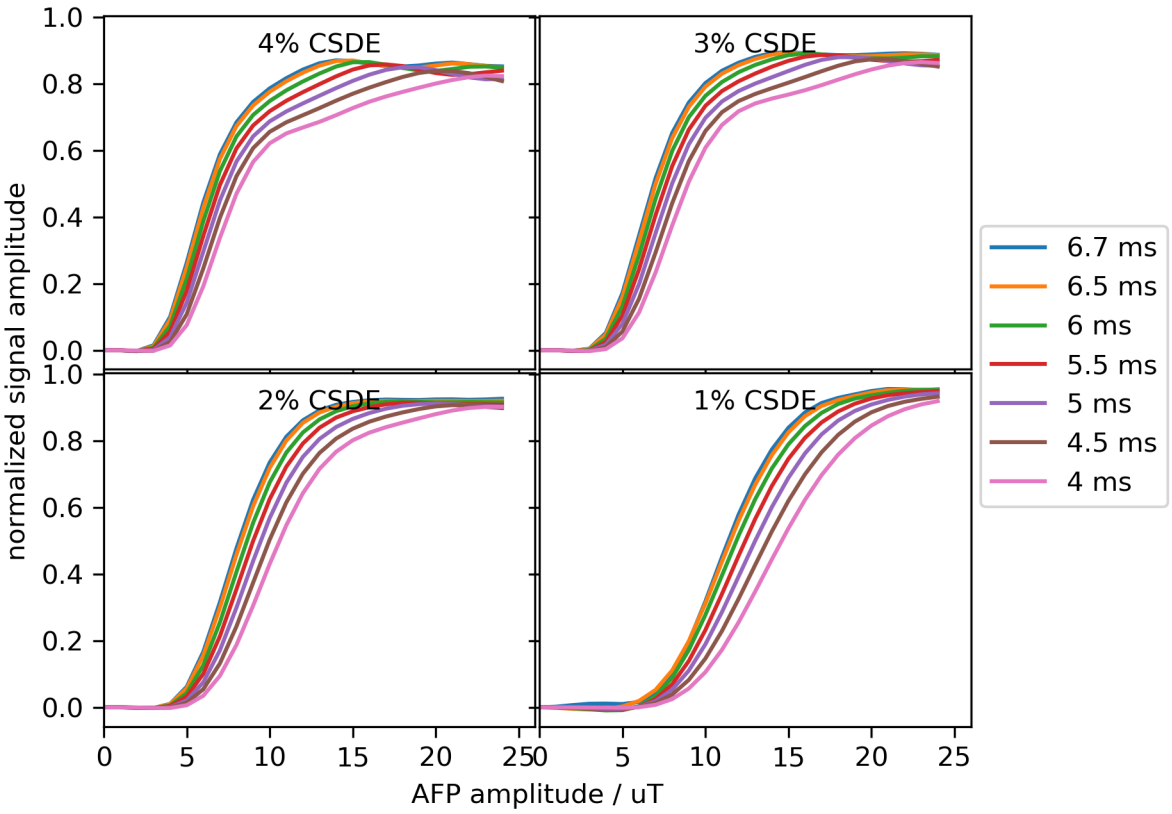

Figure 4.2: Simulated signal strength of the GABA resonance after semi-LASER localization as a function of the duration, bandwidth and maximal amplitude of the adiabatic pulses.

For these reasons, it was decided to use pulses with a duration of 6.7 ms. The 1 % CSDE pulses require too much B_1^{max}, and thus, 2 % CSDE pulses were selected. These settings have a threshold B_1 of 13 μT. However, these simulations do not include any B_1 inhomogeneities. Therefore, a larger B_1^{max} was selected to ensure effective refocusing within the complete region of interest.

Editing Pulses

The editing efficiency of each simulated pulse is depicted in Figure 4.4 as function of the off-center frequency. The frequency dependence of the Gaussian pulses looks Gaussian at first glance. This is not obvious, as the editing efficiency depends non-linearly on the flip-angle (see chapter 3.3.1). Interestingly, the maximum of the editing efficiency is slightly shifted towards the water frequency. This shift increases with pulse bandwidth.

The editing efficiency depends very differently on detuning, if the fat pulse is used. In stark contrast to the Gaussian pulses, the frequency dependence is very asymmetric. The maximal editing efficiency is with a detuning of 0.15 ppm away from the GABA resonance. Although the

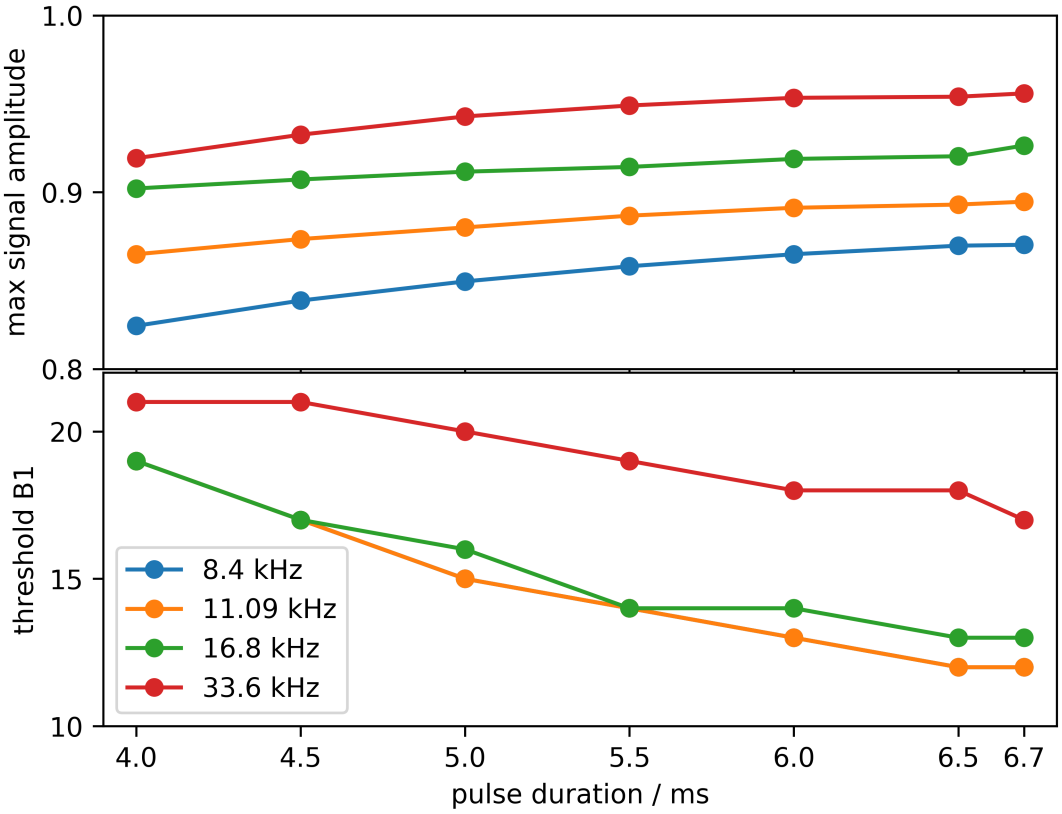

Figure 4.3: Top: Maximal achievable signal strength (top) and the threshold B_1 amplitude (bottom) as functions of pulse duration, and bandwidth.

pulse is designed to be a slice-selective pulse, it has a poor slice profile because of its narrow bandwidth. However, it has a steeper drop-off for outer frequencies. For detuning of less than 0.1 ppm, the frequency response is almost linear while lower than the Gaussian pulses.

The GABA resonance at 2.28 ppm is slightly influenced by the editing pulses. Apparently, it is much more affected by the fat pulse when it is on-resonant, limiting the editing efficiency. By further detuning the editing pulse, the effect on this resonance can be minimized. For all pulses, the maximally achievable editing efficiency is comparable. However, this shift would cause the macromolecular resonance, that has a coupling partner at 3.0 ppm, to be almost on-resonant and, consequently, increase the macromolecular contribution to the measured GABA signal.

Frequency fluctuations will introduce a systematic error in the GABA measurement if they affect the editing efficiency. Therefore, fat pulses were selected, as it produces an editing efficiency that is less affected by frequency fluctuations within the expected range of frequency drift. To not further increase the macromolecular contribution, the editing pulses were played out on-resonant. This leads to a small drop in SNR, compared to the use of Gaussian pulses.

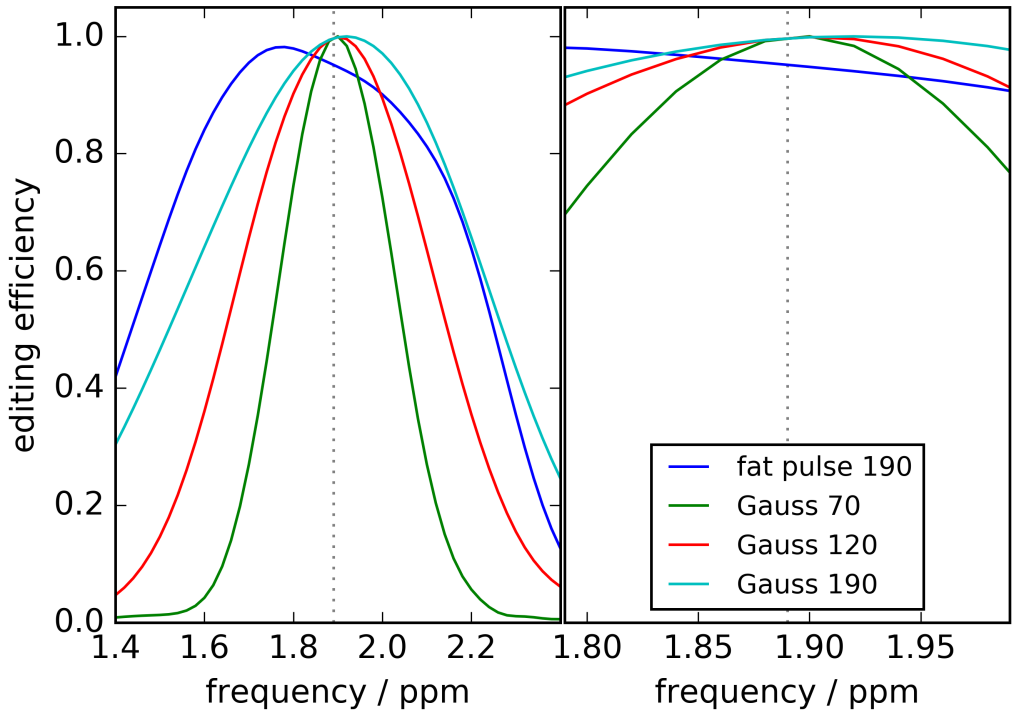

Figure 4.4: Editing efficiency of Gaussian pulses with different bandwidths, as well as the fat suppression pulse as a function of detuning. The editing efficiency is normalized to the highest value of all pulses. The dotted line marks the targeted GABA resonance at 1.89 ppm. On the left-hand side, variations of up to 0.5 ppm from the GABA resonance are depicted. On the right hand-side, only variations of 0.1 ppm are depicted.

Phantom validation

In Figure 4.5 a comparison between the simulated signal and the measured signal is depicted as a function of $B_1^{\max}$. Both, the GABA signal and the water signal, agree with the simulations satisfactorily, although the simulations do not include intra-voxel variations for B_0 and B_1, or coupling effects.

4.4 Optimization of the shimming process

4.4.1 Motivation

In this thesis, the hippocampus is the primary target for GABA spectroscopy. However, severe susceptibility differences and, therefore, B_0 inhomogeneities are present in this region. Additionally, the hippocampus is an elongated structure. Therefore, the VOI has to have to rather large in one dimension to include the complete hippocampus. This makes shimming in this region even more complicated.

The scanner is equipped with 12 shim coils, which can create an additional static field to mitigate these inhomogeneities to some extent (see chapter 2.5.1). Optimal B_0 shimming

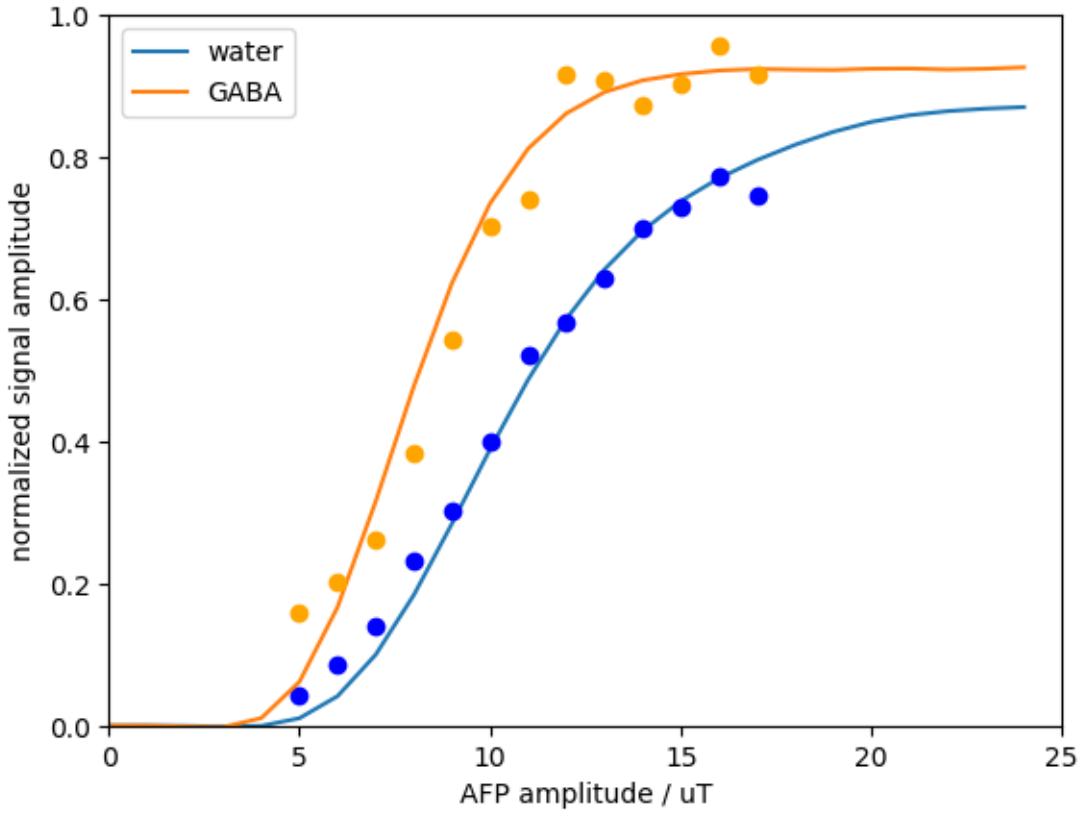

Figure 4.5: Simulated and measured GABA (orange) and water (blue) signal strength, pulses with 16.8 kHz bandwidth and 6.7 ms duration as a function of B_1^{max}.

is essential for reliable hippocampus spectroscopy, as it prolongs the T_2^* and, consequently, improves the SNR. The shimWIP allows a semi-automatically calculation of the optimal shim currents from acquired B_0 maps. The shimWIP can be applied iteratively. Furthermore, the performance of the optimization might depend on the resolution of the used B_0 map.

The aim of this experiment is to identify the optimal shimming procedure for hippocampus spectroscopy. The final goal of this thesis is to provide a measurement technique for routine use in clinical studies. Therefore, it is very important that the shimming process works reliably, as the rejection of measurements is problematic due to the limited number of potential subjects.

This study was conducted together with Yvonne Kilian. More information can be found in her Bachelor thesis [99].

4.4.2 Methods

The scanner has a predefined set of default shim currents called the tune-up shim. Using these shim currents and the shimWIP, a whole-brain B_0 map with 4 mm isotropic resolution was acquired. A (2x2x5) cm^3 region of interest and a concentric (2.5x2.5x5.5) cm^3 adjustment volume were defined, which contain the complete hippocampus. Shim currents that minimize B_0 inhomogeneities within the adjustment volume were calculated using the script provided

by the shimWIP. Utilizing these shim values, a water-unsuppressed spectrum was acquired using the MEGA-sLASER sequence with the parameters optimized in the previous chapter. Using the optimized shim currents, an otherwise identical B_0 map was acquired. A second optimization of the shim currents was performed based on this map. Again a water-unsuppressed spectrum was acquired. This was repeated, resulting in a third water-unsuppressed spectrum. This process, starting from tune-up shim, was repeated for other B_0 field map resolutions (3 mm, 2 mm, 1.8 mm).

Two different studies were concluded using this layout. First, seven young, healthy volunteers participated in a study, in which only used second-order shim coils were used. Afterwards, eight young, healthy volunteers participated in a study, in which the third-order shim coils were used as well. In the 3rd-order study the measurements were stopped twice due to technical problems. Additionally, one measurement was stopped on the subject's wish.

The FWHM and the T_2^* of each water signal of each subject were calculated and used as metrics of shim quality.

4.4.3 Results and Discussion

The measured T_2^* and FWHM of the water resonances are summarized in Figures 4.6 and 4.7, respectively. Using a Friedman test, no significant differences between the different 2nd-order shim procedures were present either in the T_2^* ($p = 0.777$) or in the FWHM ($p = 0.509$). In the case of 3rd-order shimming, the first iteration of shim values leads to very poor results. A Friedman test of the remaining eight shimming procedures shows some significant differences in the T_2^* ($p = 0.018$), but not in the FWHM ($p = 0.056$).

Furthermore, 3rd-order shimming outperforms 2nd-order shimming significantly. As indicated in Figures 4.6 and 4.7, the median T_2^* is higher for each shimming procedure if 3rd order shimming is enabled. The median FWHM is lower for 7 out of 8 shimming procedures. For the majority of shimming procedures, this difference is statistically significant.

Due to possible stability issues and the requirement of an additional GUI, which makes the 3rd-order shimming process prone to faulty usage, only 2nd-order shimming will be performed from now on. Obviously, 3rd-order shimming is an interesting option to further improve the presented method. For technical reasons, the adjustment volume will match the region of interest from now on. This change facilitates the automatization of the shimming process. Although no significant effects could be measured using only 2nd-order shimming, the results for 3rd-order shimming clearly indicate the benefits of repetitive shimming. As it costs only one minute of measurement time, a 2-step repetition is used from now on. As no statistically significant differences in shimming quality could be found when different field map resolutions were tested, further studies will be performed using field maps with 4 mm isotropic resolution. This is done to minimize the time spent on shimming.

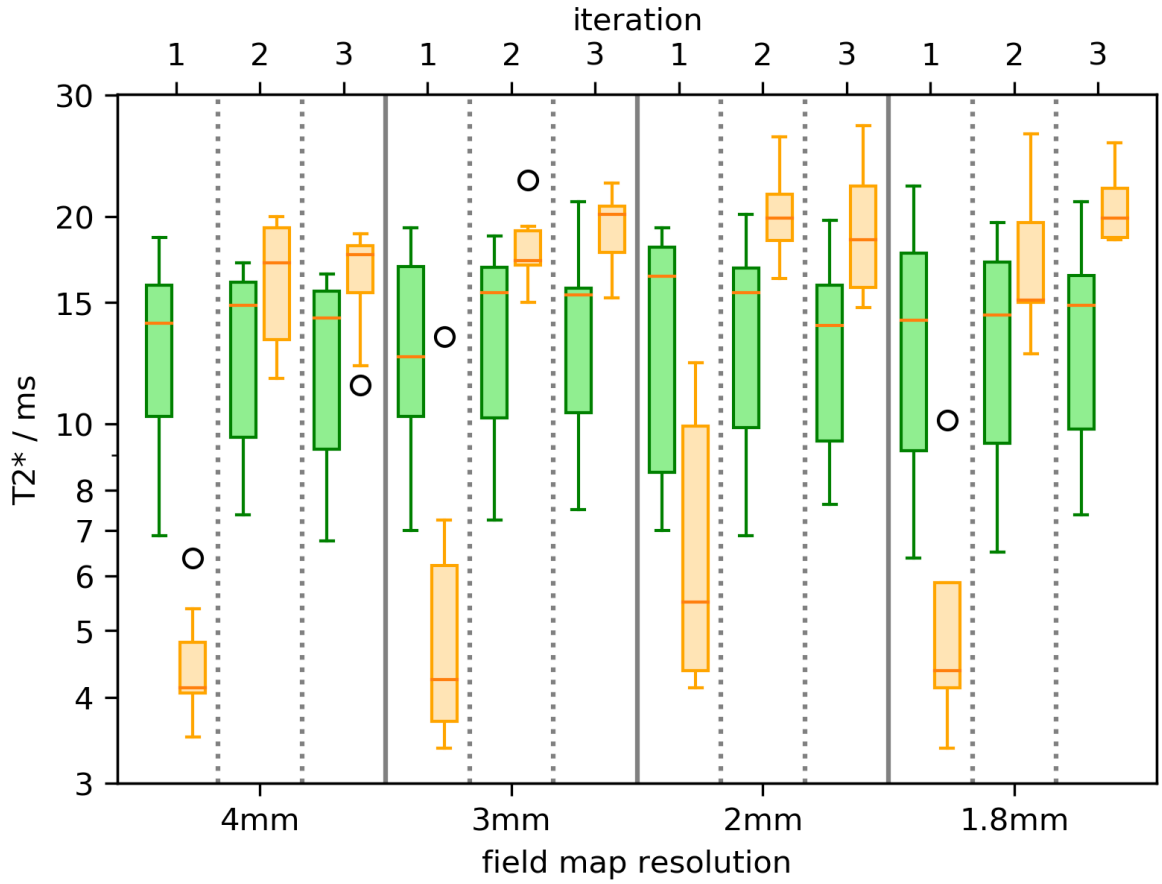

Figure 4.6: Boxplots of the T_2^* of the water reference spectrum using different shimming routines. For each B_0 map resolution, the optimal shim currents were calculated in a 3-step repetition using either 2nd-order (green) or 3rd-order shimming (orange). The orange line in each boxplot represents the median value.

4.5 Reproducibility of GABA Spectroscopy in the Hippocampus

4.5.1 Motivation

Before the hippocampal GABA spectroscopy can be performed in clinical studies, it is important to know the precession of the method in order to estimate the expected variation within the measured cohort. To optimize the reproducibility of the hippocampal GABA quantification, multiple MEGA-sLASER measurements, utilizing all the optimizations presented in the course of this chapter, were performed within the same session. Optimizations in the preprocessing approach and in the spectral quantification process were performed to increase the reproducibility of GABA quantification even further.

The results of this study were partially published in a Magma paper [24].

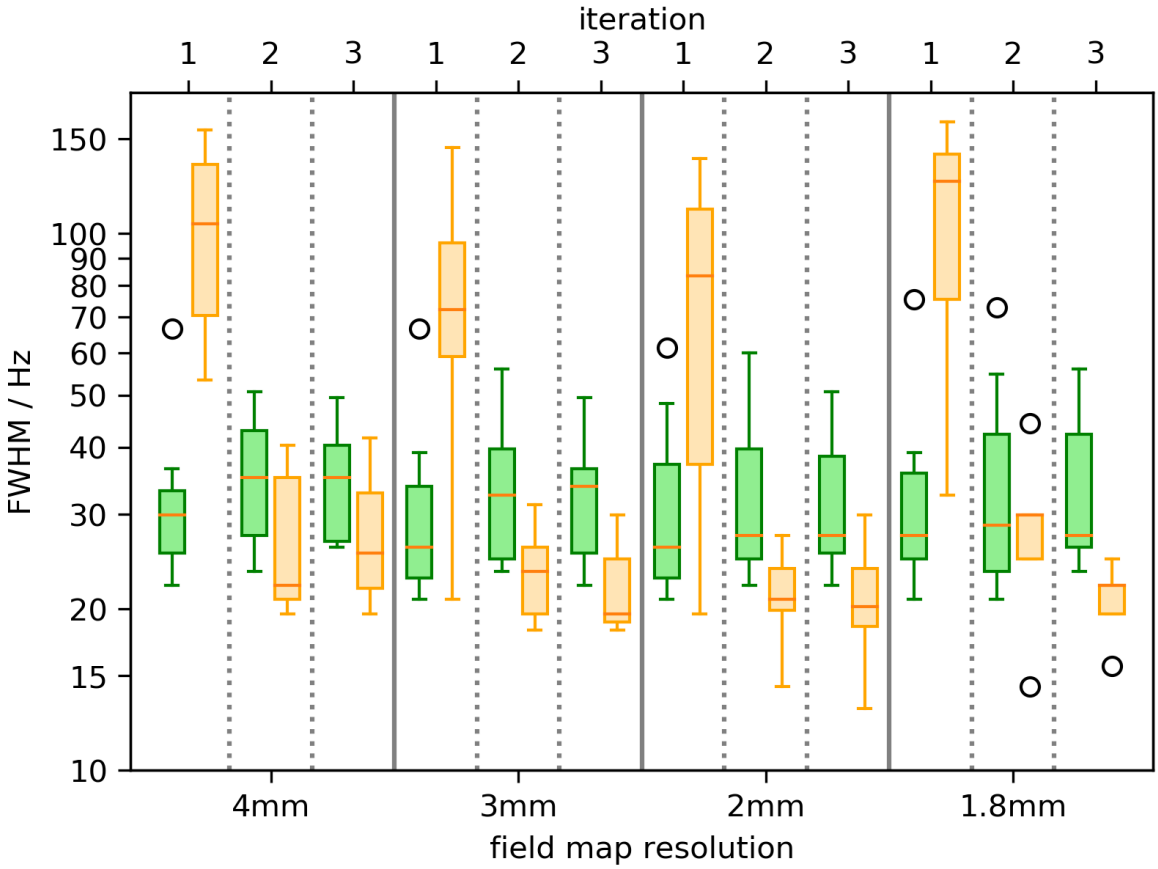

Figure 4.7: Boxplots of the FWHM of the water reference spectrum using different shimming routines. For each B_0 map resolution, the optimal shim currents were calculated in a 3-step repetition using either 2nd order (green) or 3rd order shimming (orange). The orange line in each boxplot represents the median value.

4.5.2 Methods

Data Acquisition

Ten young, healthy volunteers (26.6±4.7 years, 5 male, 5 female) participated in this study. Before the spectroscopic measurements, a whole-brain T1-weighted image, using MP-RAGE [74], and a whole-brain B_1 map, using DREAM [80], were acquired. A (2x2x5) cm^3 region of interest, centered around the hippocampus, was selected based on the MP-RAGE image. The B_1 adjustment was manually performed. Circular regions, concentric to the region of interest, were defined in each direction, and the reference voltage was calculated for these regions. The median voltage was manually set. Afterwards, shimming was performed, using a 2-step repetitive process as explained in chapter 4.4.

Finally, three spectroscopic measurements were performed using the MEGA-sLASER sequence with the optimizations presented in chapter 4.3. Because of SAR restrictions, T_R=7 s was necessary. The acquisition time of each measurement was 8:03 min. This time includes

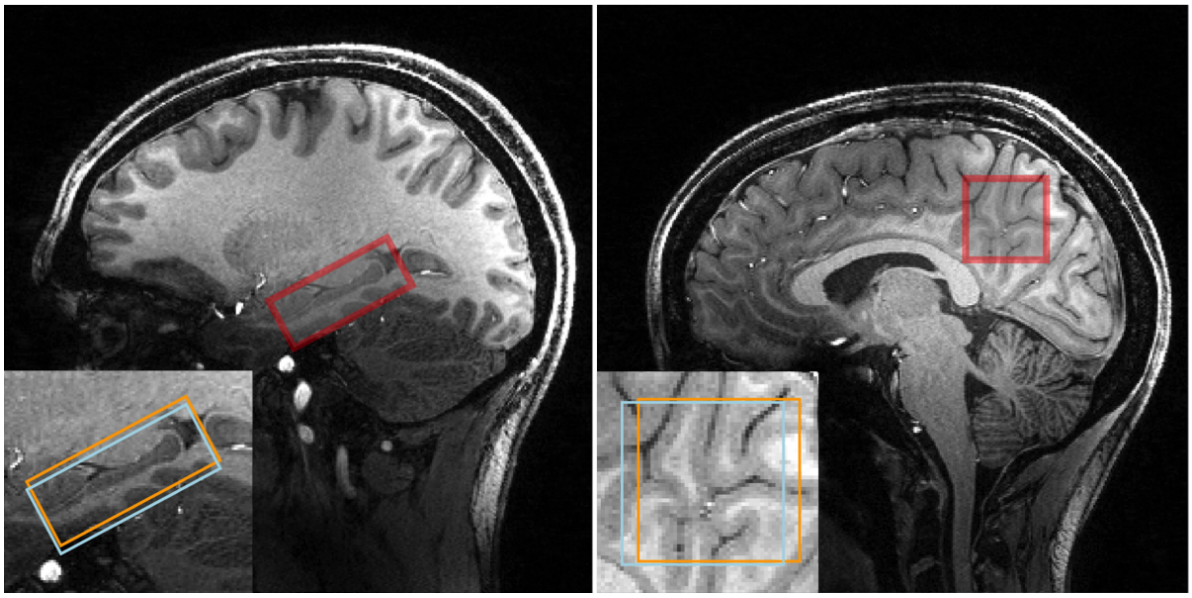

Figure 4.8: MP-RAGE images from one subject from the hippocampus data set (left) and one subject from the PCC data set (right). The nominal positions of the selected voxel are indicated by the red box. The (2x2x5) cm^3 voxel is placed at the center of the hippocampus and aligned such that the long axis of the hippocampus is parallel to the voxel. A non-oblique (3x3x3) cm^3 voxel is placed in the PCC. The insert shows the voxel positions of the GABA 3.0 ppm and the GABA 1.9 ppm resonance.

a water reference scan, 4 dummy excitations, as well as 32 edit-on and 32 edit-off excitations. During testing, it became apparent that the MEGA-sLASER sequence is prone to spurious echoes. These echoes stem from imperfect coherence pathway selection. Consequently, spoiler gradient amplitudes were maximized within the hardware limits.

As a comparison for spectral quality, a small reference study was conducted in the posterior cingulate cortex (PCC) using the same acquisition protocol. Following the largest ever conducted GABA study at 3 Tesla [53], a (3x3x3) cm^3 region of interest was selected. Three young healthy volunteers participated in this study (28.3 ± 2.1 years, 1 male, 2 female). Both regions of interest are depicted in Figure 4.8.

Data processing

The complete preprocessing pipeline is explained in detail in chapter 3 and is summarized in Figure 3.5. This includes coil combination (CC), eddy current compensation (ECC), spectral registration (SR), difference artifact suppression (DAS) or difference optimization (DO), and spectral quantification (SQ). In principle, a preprocessing only containing CC and SQ leads to an estimation of the GABA concentration. To assess the importance of various processing steps, different approaches were tested. Processing pipeline with the following additional steps were tested:

1. None
2. ECC

3. SR
4. ECC+SR
5. SR+DAS
6. ECC+SR+DAS
7. SR+DO
8. ECC+SR+DAS

As approaches 3-8 can be performed with two different references during the SR step (mean edit-off signal (SRmeo) and individual signal (SRind)), 14 different approaches were tested in total.

TARQUIN parameter optimization

As explained in chapter 3.2, TARQUIN has multiple parameters that can be adjusted. The optimization of these TARQUIN parameters was performed in a two-step process. The starting value of the Gaussian signal decay β_s was optimized first, followed by the optimization of the starting time-point n_s of the quantification process. Both steps were concluded using only a subset of the 14 preprocessing approaches. Ten different β_s values between 200 and 5000 were tested, and 13 different values of n_s between 1 and 50. Note that the calculation of the GABA / total creatine requires two different quantification processes. This leads to $13 \times 13 = 169$ pairs of n_s.

In both quantification steps, the GABA / total creatine ratio (GCR) was calculated for each subject and each measurement. As no significant change in GABA concentration is expected within the timeframe of an MR session, all variations of the measured GABA concentration are considered to be caused by measurement instabilities. Therefore, the mean intra-session coefficient of variation $mCoV^{\text{intra}}$, defined as

$$mCoV^{\text{intra}} = N^{-1} \sum_i \frac{\sqrt{(M-1)^{-1} \sum_j (R_{ij} - \bar{R}_j)^2}}{\bar{R}_j}, \text{ with } \bar{R}_j = M^{-1} \sum_i R_{ij}, \tag{4.1}$$

should be minimal. Here, N is the number of subjects, M is the number of measurements per subject, and R_{ij} is the GABA / total creatine ratio measured in the j-the measurement of the i-th subject.

During the optimization of β_s, two preprocessing approaches were used. Standard processing (SRmeo) is similar to the processing routine used in the large GABA study [53]. Additionally, a more elaborate (ECC+SRmeo+DAS) preprocessing pipeline is used. For each value of β_s, the $mCoV^{\text{intra}}$ was calculated for both pipelines and every pair of n_s. For both pipelines separately, the median value of these coefficients was calculated for each β_s. The value of β_s that minimizes the average median value of both pipelines is considered optimal.

In the second processing step, only the optimized β_s was used. The $mCoV^{\text{intra}}$ was calculated for each pair of n_s, as well as all preprocessing routines that deal with difference artifacts. Note

that this includes approaches where SRmeo is used even if neither DO nor DAS is used. The pair of n_s that minimizes the median value of these coefficients is considered optimal.

It is important to ensure that there is no artificial dependence of the measured GABA concentration on the TARQUIN parameters that would introduce a systematic quantification error. Therefore, the measured GCR was plotted against n_s for various preprocessing approaches to identify possible sources of quantification error.

Optimization of the preprocessing routine

Finally, the preprocessing routine, which optimizes the hippocampal GABA quantification was identified. In this step, the mean inter-subject coefficient of variation $mCoV^{\text{intra}}$, defined as

$$mCoV^{\text{inter}} = M^{-1} \sum_j \frac{\sqrt{(N-1)^{-1} \sum_i (R_{ij} - \bar{R}_i)^2}}{\bar{R}_i}, \text{ with } \bar{R}_i = N^{-1} \sum_j R_{ij}, \tag{4.2}$$

is also considered. The inter-subject variation of the measured GABA concentration is composed of real physiological differences, as well as differences in setup, like voxel placement or shim, and inaccurate quantification. This value is an estimate of the expected variation within a cohort in a clinical study and is, therefore, the more important metric in this optimization step.

Two different quality metrics were used. First, the $mCoV^{\text{inter}}$ was only calculated using the optimized TARQUIN parameters. As a second quality metric, only the optimized β_s was used, and the top decile of $mCoV^{\text{inter}}$ was inferred from all 169 pairs of n_s to minimize the effect of possible statistical outliers. As a comparison, the same was also performed for the $mCoV^{\text{intra}}$.

4.5.3 Results

Spectral Quality

Every measured spectrum was visually inspected. No artifacts were found in the PCC dataset and in 9 out of 10 subject hippocampus subjects. However, spurious echoes were found in one subject. Data from this subject were reacquired. In Figure A.1 in the appendix, all acquired hippocampus spectra of all subjects can be found.

Figure 4.9 shows the edit-on, edit-off, and difference spectra from one subject from each dataset. The edit-off spectrum contains three prominent singlet signals. These signals arise from the main metabolites NAA, creatine, and choline. Multiple additional resonances from various metabolites are seen. In the edit-on spectra, no NAA signal is detectable. This is because it is completely refocused by the MEGA pulses. Therefore, it has a different coherence pathway and is suppressed because of the coherence pathway selection. The choline signal is completely unaffected by the MEGA pulses and, thus, looks exactly the same in both subspectra. Creatine is also unaffected by the MEGA pulses, and the difference between in edit-on and edit-off signal is caused by GABA. Multiple edited signals, including GABA and Glx, which is glutamine and glutamate, whose signals cannot be separated, are also visible in the difference spectra.

As expected, due to the severe B_0 field inhomogeneities within the hippocampus region of interest, data quality is reduced. The mean NAA line widths in the hippocampus (edit-off:

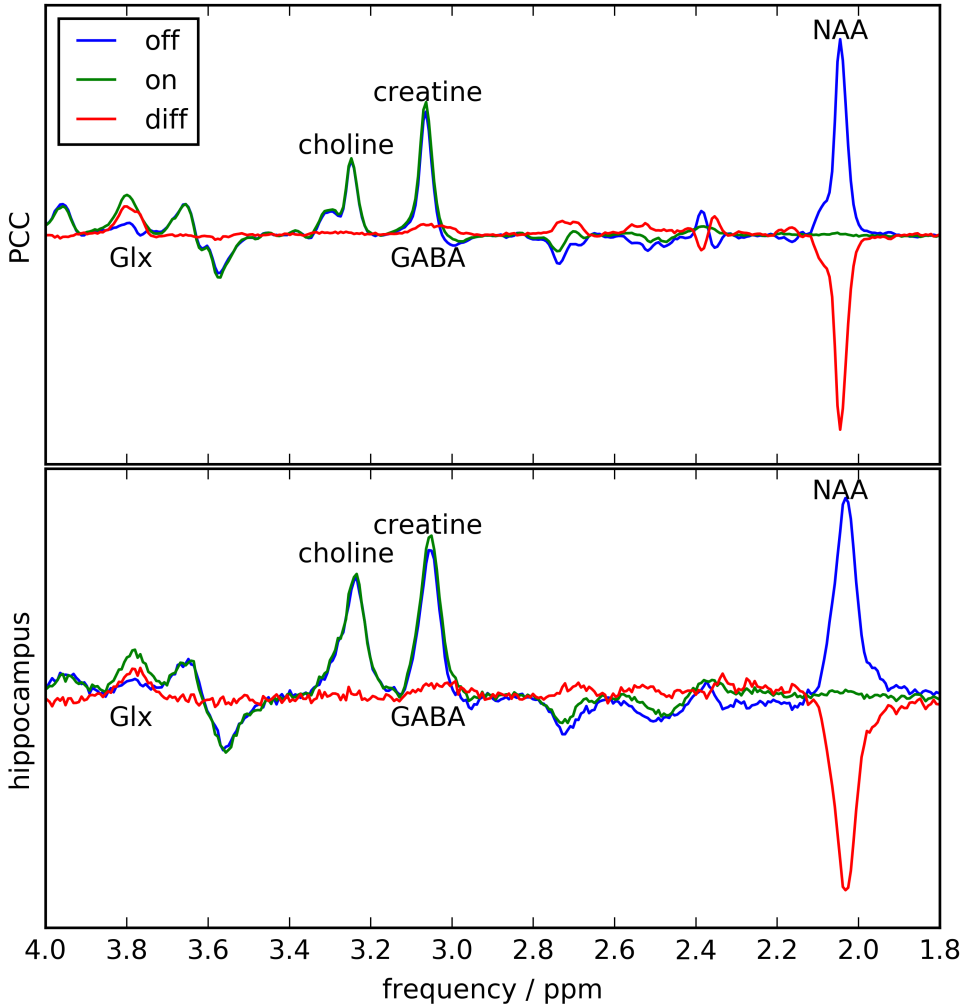

Figure 4.9: Edit-off (blue), edit-on (green), and difference spectra (red) of one subject in the PCC data set (top) and one subject in the hippocampus data set (bottom). Asides from a much broader line width and decreased SNR, the results of both brain regions look very compatible.

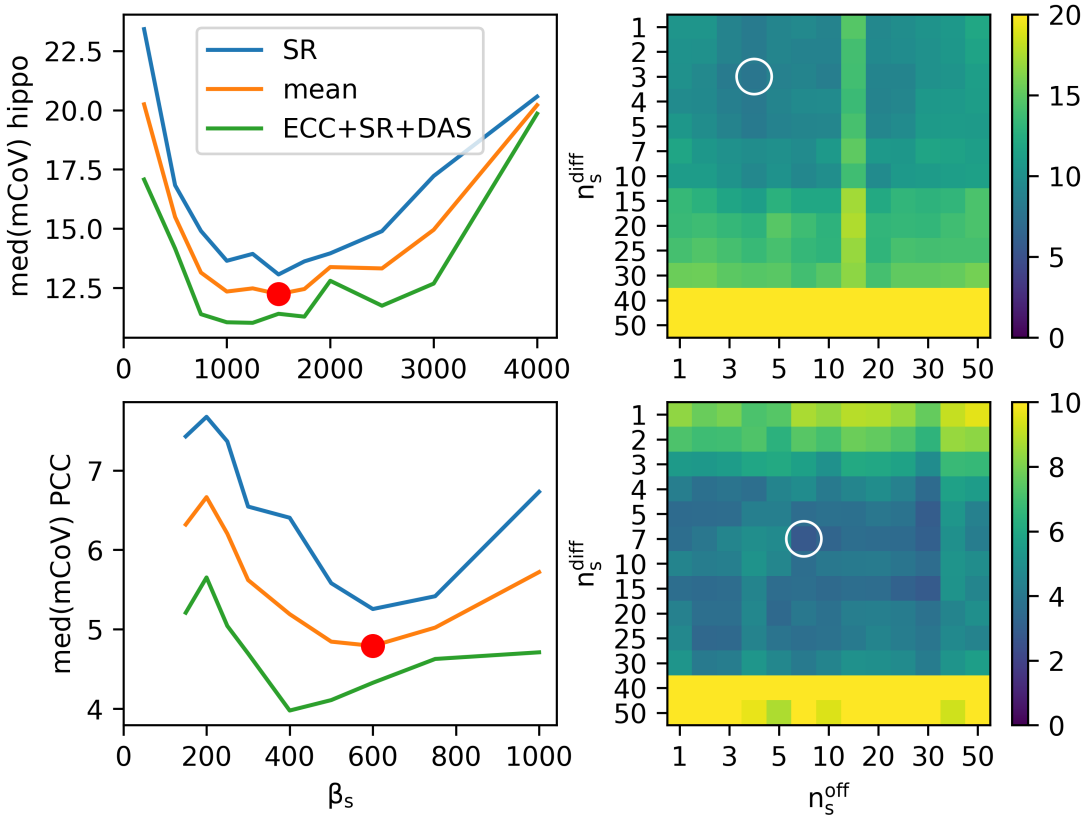

Figure 4.10: Results of the TARQUIN parameter optimization for the hippocampus (top) and PCC dataset (bottom). On the left-hand side, the optimization of β_s is shown. The median value of the intra-session CoVs of all 169 pairs of n_s is shown as a function of β_s. This is done for two data processing approaches, and the minimum of the average of this two is marked with a red dot. On the right-hand side, the optimization of n_s is shown. The median value of the intra-session COVs of all feasible data processing routines is shown as a function of n_s. The optimal values are marked with a white circle.

22.26 Hz, difference: 22.74 Hz) are far wider than the mean NAA line widths in the PCC (edit-off: 8.88 Hz, difference: 8.68 Hz). The measured NAA line width from the edit-off and the difference signal differ slightly. This is to be expected as it is extracted from different spectral quantification processes. The basis function of the NAA molecule is different in these two quantification steps.

Similarly, the NAA-SNR is significantly reduced in the hippocampus (edit-off: 43.3, difference: 35.1) compared to the PCC data (edit-off: 204.0, difference: 168.0). The SNR of the edit-off spectra is higher than the SNR of the difference spectra. This is due to the subtraction of two noise signals. The volume difference (1.35) and the difference in FWHM (2.51) explain an SNR discrepancy of a factor of roughly 3.4. The measured factor is 4.7.

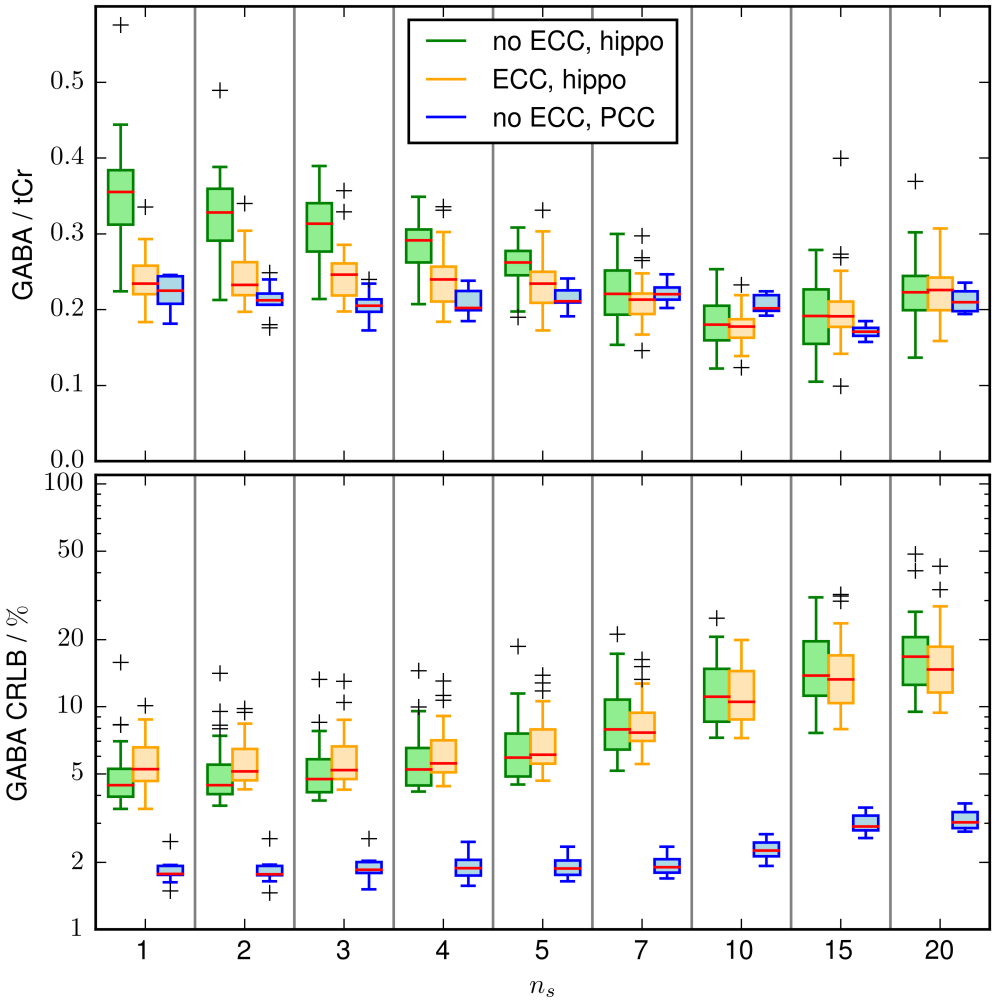

Figure 4.11: Top: Boxplots of the measured GABA / total creatine ratio as a function of n_s. Data from two preprocessing approaches are shown for the hippocampus data: SRmeo+DAS (green) and ECC+SRmeo+DAS (orange). Additionally, data from the PCC dataset is shown (SRmeo+DAS, blue). Bottom: CRLB of the GABA concentration, depicted in the same fashion.

TARQUIN parameter optimization

Figure 4.10 summarizes the results of the parameter optimization. On the left-hand, side the optimization of β_s is depicted. Advanced processing leads to reduced median $mCoV^{\text{intra}}$ for each value of β_s in both regions. The intra-session reproducible was affected by β_s, and optimal values were found at $\beta_s = 1500$ (hippocampus) and $\beta_s = 600$ (PCC).

Multiple pairs of n_s lead to comparable $mCoV^{\text{intra}}$. However, the very high $mCoV^{\text{intra}}$ indicates that values of $n_s > 30$ lead to unreliable quantification. In the PCC dataset, also very small n_s lead to a significant increase of $mCoV^{\text{intra}}$, which cannot be observed in the hippocampus dataset. Minimal $mCoV^{\text{intra}}$ is given by $n_s^{\text{off}}, n_s^{diff} = (4, 3)$ and $n_s^{\text{off}}, n_s^{diff} = (7, 7)$ in the hippocampus and PCC dataset, respectively.

In the top plot of Figure 4.11, the measured GABA / total creatine ratio is depicted as a function of n_s. To simplify the diagram, only the data for the processing pipelines ECC+SRmeo+DAS and SRmeo+DAS are shown for the hippocampus data and SRmeo+DAS for the PCC data. For $n_s < 5$, the measured hippocampal GCR increases when no ECC is performed. This quantification bias cannot be observed in the PCC dataset. However, as smaller values of n_s are identified as optimal for the spectral quantification of the hippocampus data, this is problematic. ECC completely removes this quantification bias.

The bottom plot of Figure 4.11 shows the CRLB as a function of n_s. The omission of the high signal points at the beginning of the FID causes a decrease in frequency space SNR and, consequently, an increase of CRLB. Due to the longer T_2^* in the PCC, there are more high signal points, and thus, the increase of CRLB is slower. For low n_s ECC increases the CRLB of the hippocampal GABA quantification. Note that this is caused by the artificial increase in GABA signal quantification instead of a decrease in the noise level, compared to the data without ECC.

Preprocessing approaches

Figure 4.12 shows the $mCoV^{\text{inter}}$, dependent on the processing pipeline for the hippocampus dataset. The top plot shows $mCoV^{\text{inter}}$ when the optimized TARQUIN parameters are used, while the bottom plot shows the $mCoV^{\text{inter}}$ for the first decile method.

Without phase and frequency correction, the $mCoV^{\text{inter}}$ is around 40 % (optimized parameters), and the first decile is also well above 35 %. SRmeo reduces the $mCoV^{\text{inter}}$ to below 15 %, while SRind hardly changes $mCoV^{\text{inter}}$. Additional suppression of difference artifacts significantly reduces the $mCoV^{\text{inter}}$ after SRind and has little effect after SRmeo. Using SRind the resulting values are still increased compared to SRmeo. DAS consistently leads to lower $mCoV^{\text{inter}}$ than DO.

The red dots in Figure 4.12 mark the preprocessing approach that leads to minimal $mCoV^{\text{inter}}$ for each quality metric. In contrast, the optimized TARQUIN parameter leads to SRmeo+DAS (12.1 %) as optimal, while the first decile identifies ECC+SRmeo+DAS (12.3 %) as the optimal preprocessing approach.

Figure 4.13 shows the $mCoV^{\text{inter}}$ in the PCC, dependent on the preprocessing approach, in the same fashion as Figure 4.12. A similar trend as in the hippocampus can be observed, but with strongly reduced values. Without phase and frequency correction, the $mCoV^{\text{inter}}$ is roughly 30 % (optimized parameters) and roughly 20 % (top decile).

SRmeo reduces the $mCoV^{\text{inter}}$ to around 5 %. The $mCoV^{\text{inter}}$, using optimized parameters, is elevated if ECC is used. Again, this drop is not observable when using SRind.

Additional suppression of difference artifacts further reduces the $mCoV^{\text{inter}}$. Again, using the optimized TARQUIN parameters, ECC leads to increased $mCoV^{\text{inter}}$. Using the first decile, this cannot be observed, and all ECC settings and SR references lead to basically identical $mCoV^{\text{inter}}$ of around 4 %. Again, DAS consistently outperforms DO.

The red dots in Figure 4.13 mark the preprocessing approach that leads to minimal $mCoV^{\text{inter}}$ for each quality metric. The optimized TARQUIN parameter leads to SRind+DAS (3.37 %) as optimal, while the first decile identifies ECC+SRmeo+DAS (3.74 %) as optimal.

In the appendix, Figures A.2 and A.3 depict the $mCoV^{\text{intra}}$ of the hippocampus and PCC dataset, respectively. Compared to the $mCoV^{\text{inter}}$, very similar patterns can be found with reduced

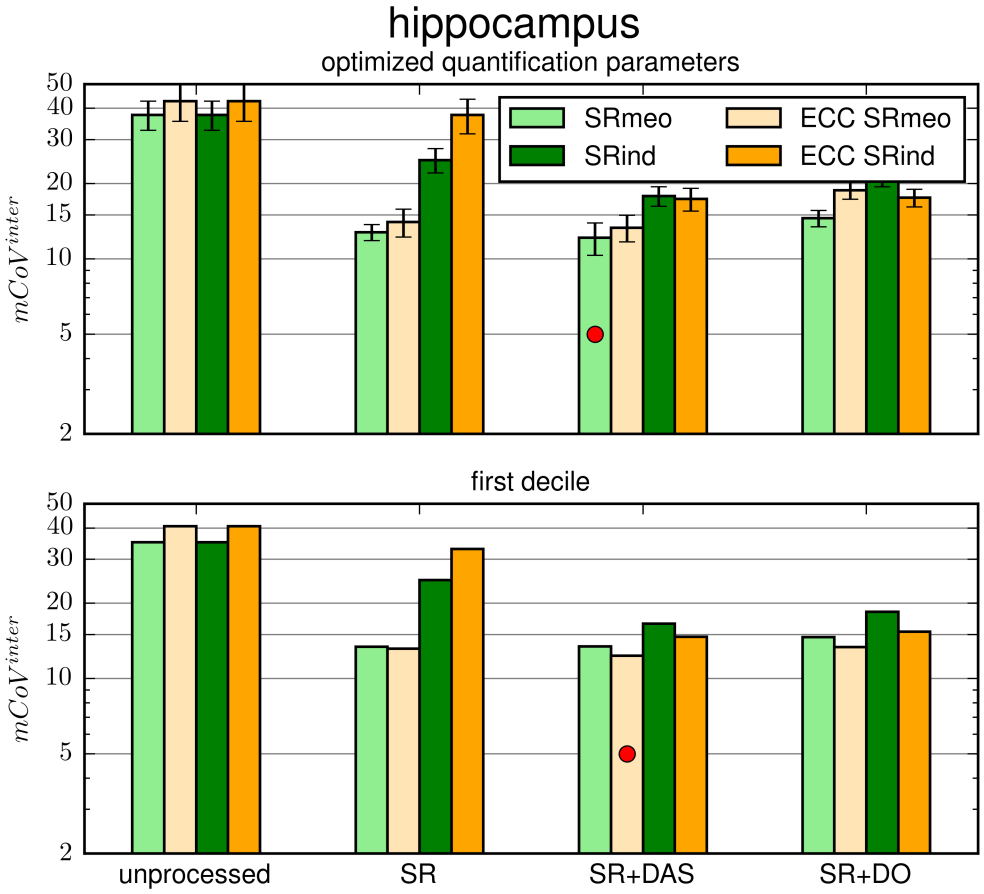

Figure 4.12: $mCoV^{\text{inter}}$ in the hippocampus for all tested data processing approaches. On the x-axis, the phase and frequency correction method is shown (None, SR, SR+DAS, SR+DO), and the bars represent different ECC settings and SR references. The top plot shows the $mCoV^{\text{inter}}$ obtained with the optimal TARQUIN parameters, while the bottom plot shows the top decile of the $mCoV^{\text{inter}}$ of all the 169 pairs of n_s for each data processing routine. The data processing routine that is identified as optimal by either quality metric is marked with a red dot.

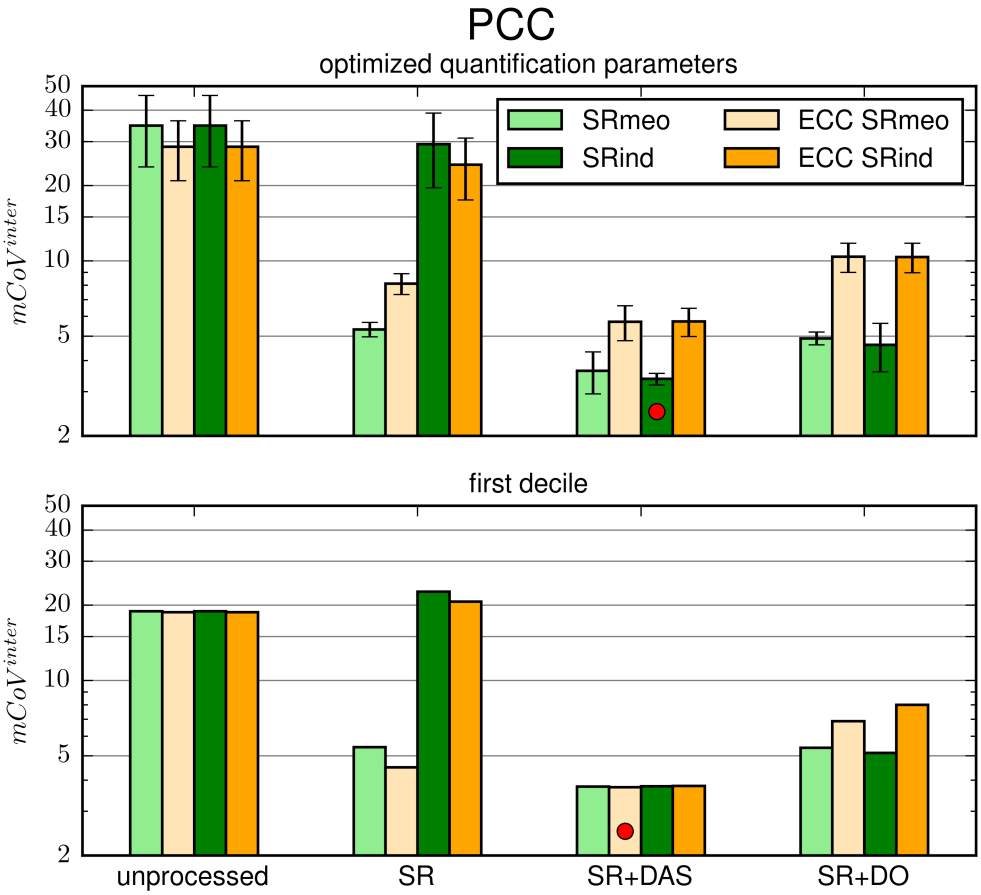

Figure 4.13: $mCoV^{\text{inter}}$ in the PCC for all tested data processing approaches. On the x-axis, the phase and frequency correction method is shown (None, SR, SR+DAS, SR+DO), and the bars represent different ECC settings and SR references. The top plot shows the $mCoV^{\text{inter}}$ obtained with the optimal TARQUIN parameters, while the bottom plot shows the top decile of the $mCoV^{\text{inter}}$ of all the 169 pairs of n_s for each data processing routine. The data processing routine that is identified as optimal by either quality metric is marked with a red dot.

	$mCoV^{\text{intra}}$ optimized	$mCoV^{\text{intra}}$ top decile	$mCoV^{\text{inter}}$ optimized	$mCoV^{\text{inter}}$ top decile
hippocampus	7.25 % ECC SRmeo DAS	8.04 % SRmeo	12.1 % SRmeo DAS	12.3 % ECC SRmeo DAS
PCC	2.95 % SRmeo DAS	2.64 % ECC SRmeo DAS	3.37 % SRind DAS	3.74 % SRmeo DAS

Table 4.2: Minimal mean coefficient of variation for both brain regions and all four quality metrics, including the processing approach that minimizes these values.

values. Using the optimized TARQUIN parameters, the minimal value is 2.95 % (SRmeo+DAS) in the PCC, while a minimum of 2.64 % (ECC+SRmeo+DAS) is reached using the first decile. Again, the values in the hippocampus are much higher. Using optimized TARQUIN parameters, the minimum is 7.25 % (ECC+SRmeo+DAS), and using the first decile, the minimal value is 8.04 % (SRmeo).

Table 4.2 summarizes the minimal $mCoV$ and the processing approach that leads to these values. The results for both coefficient of variations ($mCoV^{\text{intra}}$ and $mCoV^{\text{inter}}$) are shown. Thus, a total of 8 metrics are shown. The optimal processing routine contains SRmeo in 7 out of the 8 metrics, while the last one contains SRind. DAS is also contained in 7 out of the 8 optimal routines, while the last one does not perform any additional difference artifact suppression. Only 3 quality metrics favor ECC.

4.5.4 Discussion

Accurate measurements of the hippocampal GABA concentration can be performed at 7 Tesla with an inter-subject CoV of around 12 %. However, optimizations of the preprocessing and the spectral quantification process are necessary to reduce the inter-subject CoV to this value.

J-editing removes the creatine signal that overlaps with the GABA signal. As explained in chapter 2.2.10, this does not hold true for some macromolecular signals. However, macromolecular suppression (MMC) was shown to significantly reduce the reproducibility of GABA measurements at 3 Tesla [53]. The severe B_0 inhomogeneities already cause a reduction of reproducibility in GABA quantification in the hippocampus. Therefore, no MMC was performed in this study. However, MMC might severely benefit from the increased spectral dispersion of ultra-high fields.

Ultra-high field spectroscopy profits from its increased spectral dispersion. Here, this spectral dispersion enables spectral quantification of signal from a region of interest with severe B_0 inhomogeneities. The maximal NAA line width of 29.3 Hz (0.099 ppm) was just below the suggested limit of 0.1 ppm [94–96]. The expert consensus is to consider concentrations extracted from spectra beyond this limit to be unreliable and omit them. The mean FWHM was way below this threshold. 3rd order shimming might further reduce the FWHM. This would not only improve data quality but also reduce the risk of possible data omission, which would reduce the cohort size in future clinical studies.

The hippocampus lies further within the brain than the PCC. Consequently, the distance between the region of interest and the nearest receive coil is larger. This results in a lower coil sensitivity and, thus, a reduced signal strength. This explains the remaining SNR disparity between the hippocampus and PCC spectra, after considering line width broadening and volume differences.

The MEGA-sLASER sequence is prone to spurious echoes. In order to improve coherence pathway selection, the crusher gradient moment was maximized within the hardware limits. This method is not fail-safe, as spurious echoes still occurred in one of the subjects. Furthermore, these gradients induce strong eddy currents that introduce a quantification bias. This bias can be removed by using subsequent, additional ECC. Interestingly, this quantification bias is only present in the hippocampus data set. Presumably, the reason for this behavior is the short T_2^* of the hippocampus signal. Eddy-current effects are strongly time-dependent and, therefore, only affect the first few time points. The PCC signal consists of more high SNR time points than the hippocampus. As a result, the corrupted points are weighted less severely in the quantification of the PCC data. This explanation is backed up by the fact that the quantification bias vanishes in the hippocampus data when $n_s > 5$.

Spectral registration strongly increases the reproducibility of GABA MRS when registering the edit-on and edit-off excitations onto a common reference. This cannot be observed when individual reference is used, which is because difference artifacts are the main error source for GABA spectroscopy using J-editing. They arise from a frequency and phase mismatch of the mean edit-on and edit-off signals. This mismatch causes an imperfect suppression of the creatine signal in the difference spectrum, which is mistaken as GABA signal during spectral quantification. SRind registers the single excitation signals onto these mismatched references and, thus, preserving the difference artifact. SRmeo registers all individual excitation signals to the same reference and, consequently, reduces the difference artifact indirectly.

Subsequent suppression of these artifacts only has a smaller effect on the reproducibility. However, the vast majority of preprocessing routines, which minimize one of the quality metrics, include DAS (seven out of eight). The same number identifies SRmeo to outperform SRind. This is surprising at first glance. The reference spectrum and the spectra that are corrected are of different shape, when SRmeo is applied to the edit-on spectra. However, SRmeo provides an indirect difference artifact suppression. Presumably, subsequent difference artifact suppression is prone to local minima and, consequently, does not fully remove difference artifacts in all instances. This would also explain the fact that this difference is more pronounced in the hippocampus data, in which the low data quality further complicates the minimization problem.

Only three out of the eight preprocessing routines, which minimize one of the quality metrics, include ECC. However, the removal of the quantification bias is essential for precise measurements of the GABA concentration in the hippocampus. Thus, ECC is considered an essential step in the processing of hippocampal spectra.

Consequently, the processing routine ECC+SRmeo+DAS is identified as the optimal processing routine for hippocampal GABA spectroscopy.

Multiple reproducible studies were performed at 3 Tesla in less challenging brain regions. The inter-subject coefficient of variation is usually around 10 % [53, 100] without MMC. Employing MMC, the coefficient of variation increases to 13-20 % [53, 101]. The test-retest variation can be smaller and strongly depend on the time between measurements [102]. The

inter-subject coefficient of variation includes methodological inaccuracies as well as biological variations. The test-retest approach minimizes the biological variation by measuring the same subjects repeatedly. The $mCoV^{\text{inter}}$, additionally, reduces methodological inaccuracies by using identical shim settings, B_1 calibration, and placement of the region of interest for repeated scans. Therefore, the test-retest reproducibility is expected to lie between the $mCoV^{\text{inter}}$ and the $mCoV^{\text{intra}}$.

Two reproducibility studies reported the test-retest CoV of GABA spectroscopy at 7 Tesla using J-editing. Prinsen et al. reported a test-retest CoV of 9.5 % in the occipital cortex [103], while Wijtenburg et al. reported test-retest CoVs of 16.2 % and 13.4 % in the anterior cingulate and the dorsolateral prefrontal cortex, respectively [104]. Prinsen et al. used a MEGA-sLASER sequence for data acquisition and LC-model for spectral quantification. Wijtenburg et al. used a modified MEGA-PRESS sequence and performed peak integration for quantification. Prinsen et al. reported a mean line width of 12.2 Hz, while Wijtenburg et al. achieved a line width of below 10 Hz in both examined brain regions. Thus, the reproducibility of the hippocampal GABA measurements in this work is comparable to the reported values from other brain regions, despite a much broader line width. However, both studies used macromolecule suppression, which lowers the reproducibility at 3 Tesla [53].

Both, Wijtenburg et al. and Prinsen et al., compared the reproducibility of the GABA quantification when J-editing is used to its quantification based on other spectroscopic techniques. The methods were similarly reproducible. This is enabled by the increased spectral dispersion of ultra-high field spectroscopy, which simplifies the separation of signals. However, the broad line width of the hippocampus spectra cancels this effect. The FWHM in these experiments was roughly 2 times narrower compared to the hippocampus spectra in this thesis. Therefore, the spectral resolution of the hippocampus spectra resembles the 3 Tesla resolution for more easily accessible brain regions. At this field strength, J-editing clearly leads to higher reproducibility [105].

The big difference in reproducibility in both estimated brain regions identifies the data quality of the hippocampus spectra as the main error source. Data quality is corrupted by the difficult shim conditions in the hippocampus. As shown in chapter 4.4, 3rd-order shimming promises decreased line width and, consequently, increased reproducibility.

Adiabatic sequences at 7 Tesla produce much SAR. In this study, safety regulations enforced $T_R = 7$ s. A lower repetition time would lead to a more efficient data acquisition and, thus, higher SNR. The most promising method for SAR minimization is B_1 shimming [106].

Partial volume effects are a limitation of this study. Hippocampus segmentation of the acquired MPRAGE images shows that the hippocampus takes up only around 20 % of the region of interest. Segmentation was performed using FSL [107]. However, the sLASER localization technique is limited to cuboid regions. The shape of the hippocampus requires a larger region of interest. Parallel-transmit-based, subject specific-localization techniques, as presented in [108], could be an approach to minimize partial volume effects. Another promising approach might be spectroscopic imaging. It is possible to combine the signal of multiple voxels. If the signals of all voxels that contain hippocampus tissue are combined, the partial volume effects might be drastically reduced. This method also allows correction for frequency differences prior to the signal combination and consequently reduce the influence of B_0 inhomogeneities.

Besides these limitation the achieved reproducibility will be sufficient to investigate disease-

specific changes in the hippocampal GABA concentration. This will be used in upcoming clinical cohort studies.

4.6 Conclusion

The first part of this chapter describes the implementation, testing and optimization of a MEGA-sLASER for reliable and reproducible GABA spectroscopy. Using classical and quantum mechanical simulations, the pulse sequence was optimized to maximize the GABA signal. To suppress spurious echoes, a 16-step phase cycling was implemented, as well as strong crusher gradients. Furthermore, a 2-step shimming routine was developed using up to 2nd order shim coils.

After these optimizations, the sequence was applied to measure the human hippocampal GABA concentration *in vivo*, which has previously not been reported. Susceptibility discontinuities near the hippocampus cause strong magnetic field inhomogeneities, which cannot be completely compensated for by shimming methods. This leads to an accelerated signal decay and consequently, to reduced spectral quality. A data processing workflow specifically tailored to hippocampus spectroscopy, was developed in the second part of this chapter.

Spectral quantification was performed with TARQUIN. By minimizing the intra-session reproducibility, quantification parameters were optimized. The strong crusher gradients introduced eddy-currents in the measured signal, which could not be completely compensated for by the scanner model. These eddy currents introduced a quantification bias in the hippocampus data, which could be removed by using additional, retrospective eddy current compensation. Phase and frequency variations during scanning caused difference artifacts, which were the main error source for GABA quantification. Spectral registration on a common reference, in combination with additional difference artifact suppression was found to reduce these artifacts best.

This optimized measurement routine and data processing workflow allow measuring the GABA to creatine signal ratio with an inter-subject variation of around 12 % within 8 minutes of measurement time. This is comparable to the variation reported reproducibility in less challenging brain regions at both 3 Tesla and 7 Tesla. A small reference study, using the same measurement routine, was performed in the posterior cingulate cortex. This reference study leads to far higher reproducibility. This indicates that the low spectral quality of the hippocampal spectra, caused by the fast signal decay, is the main source of error in estimating hippocampal GABA concentrations.

The very high reproducibility allows for the routine use of this method to estimate hippocampal GABA concentration in clinical cohort studies.

CHAPTER 5

Spectroscopic Imaging of GABA using MEGA-sLASER EPSI

5.1 Motivation

In the previous chapter, it was shown that the GABA concentration can be reliably measured using single voxel spectroscopy, even in regions with severe B_0 inhomogeneities. However, the spatial distribution of GABA cannot be inferred from this. Reliable GABA MRSI would allow to measuring the *in vivo* GABA concentration of multiple brain regions simultaneously. This would be of great interest for diseases that affect multiple brain regions. Furthermore, it provides a promising approach to limiting the effects of anatomical differences between subjects, which cannot be easily compensated for in an SVS measurement.

Performing *J*-edited GABA MRSI at lower field strength has been proposed in 2D [109] and even in 3D [110]. At 7 Tesla, non-edited MRSI experiments have been performed with increasingly high resolution [55, 111] and the GABA signal is part of the spectral quantification. While this approach works extremely well for more prominent metabolites, the resulting data quality is insufficient for reliable GABA concentration estimates [111]. Analogously to SVS, *J*-editing might facilitate GABA MRSI.

J-editing depends on refocusing pulses, which are prone to B_1 inhomogeneities, which are much stronger at ultra-high field. The small voxel size in an MRSI experiment leads to a reduced SNR compared to SVS.

To explore the feasibility of MEGA-sLASER based GABA MRSI, an EPSI readout scheme was added to the sequence, optimized in the previous chapter. The EPSI readout scheme was derived from the EPI readout, that has been routinely used at the DZNE for several years[112–114]. The resulting MRSI sequence was tested *in-vivo* in one young, healthy volunteer.

5.2 Sequence implementation

A sequence diagram is depicted in Figure 5.1. The RF pulses are identical to the pulses in the MEGA-sLASER sequence developed in the previous chapter (see 2.7). This includes the pules

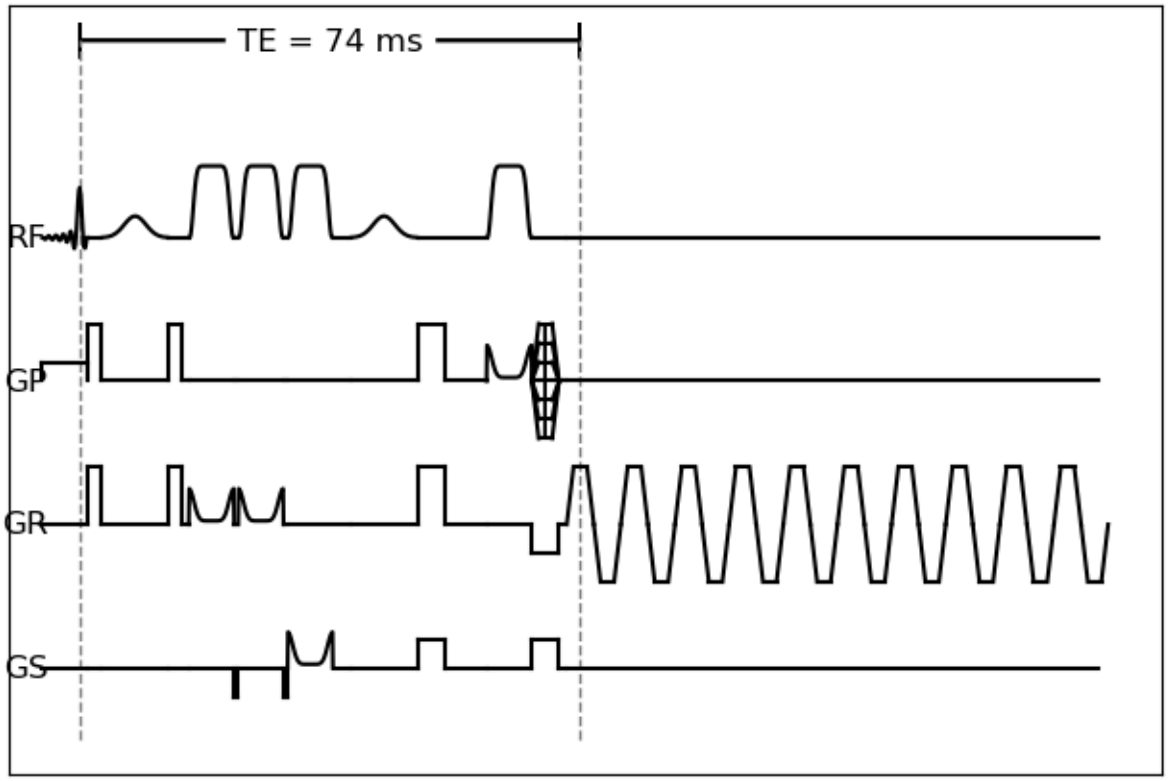

Figure 5.1: Sequence diagram of the MEGA-sLASER sequence developed in this thesis. Up until the last RF pulse the only difference to the SVS version of this sequence is the change of axis in which the spoiler gradients are applied. After the last RF pulse, the spoiler gradient scheme is completed (slice direction), the phase encoding is performed (phase direction), and the EPSI-readout id prepared (readout direction). The EPSI readout is afterwards performed such that the echo time coincides with the first k-space zero crossing.

shown in Figure 5.1 and the preceding water suppression. However, the axes of the spoiler gradients are swapped. This is done for technical reasons. The sequence is implemented as 2-dimensional imaging sequence within the SIEMENS IDEA framework. These sequences define the x, y, z directions as phase, readout, and slice, respectively. The scanner control GUI assumes the respective role of these directions. After the last RF pulse a final spoiler gradient is applied in one direction. In phase direction, the phase encoding gradient has to be played out during this time. Additionally, the prephase gradient is played out in readout direction. Therefore, the final spoiler gradient needs to be played out in slice direction to not coincide with any imaging gradient. The gradient axes are Figure 5.1 are renamed in order to indicate their role in imaging.

Again, the bandwidth of the excitation pulse is much lower compared to the adiabatic pulses. Therefore, one spatial dimension suffers from CSDE more strongly. With the EPSI readout, the spatial distribution of the GABA concentration can be measured in two dimensions, while the signal is not resolved in the 3rd dimension. It is an important design choice if the high CSDE dimension is one of the resolved dimensions. There are two possibilities. The imaging slice can

be defined by the excitation pulse, and both pairs of refocusing pulses define the edges of the ROI within the imaging slice. The second possibility is to excite a slice in one of the imaging direction, and define the imaging slice by one of the pairs of refocusing pulses.

The slice profile of the adiabatic pulses is superior to the excitation pulse. Therefore, the signal at the edges of the excitation slice is reduced. If this slice is one of the imaging dimensions, this signal drop will affect the outermost voxels more severely than the inner voxels. If the excitation slice is not resolved by the EPSI readout, all voxels will experience the same signal drop. Therefore, resolving the excitation slice will boost the signal strength of the central voxel at the expanse of the outer voxel. These outer voxels will not be considered as they will be strongly influenced by imperfect slice profiles and the 4-compartment artifact. If the imaging slice is defined by one pair of the adiabatic pulses, the 4-compartment artifact will reduce the signal strength in each voxel. As very high bandwidth pulses are used in this thesis, this only results in a 2 % drop in SNR. Therefore, it was decided to use one pair of adiabatic pulses to define the imaging slice. It does not matter if the excitation pulse is selective in readout or phase direction. Thus, the excitation is performed selectively in phase direction in order to be as similar to the SVS sequence as possible.

In the second part of the sequence, the EPSI readout is performed as explained in chapter 2.3.3. Simultaneously to the final spoiler gradient, the prephase gradient and the phase-encoding gradient are played out. Afterwards, EPSI sampling of a single *k*-space line is performed. The gradients used for EPSI readout have a flattop time of 250 µs and a ramp time of 60 µs. Thus, the dwell time is 370 µs, instead of the 250 µs in the single voxel experiments. This results in a smaller spectral bandwidth of 2700 Hz. 2048 gradients were played out, resulting in 2048 points in the spectra.

With this sequence, a single *k*-space line can be measured for each excitation. Multiple *k*-space lines have to be acquired in order to completely sample the *k*-space. Furthermore, this has to be done for the edit-on and edit-off subspectra individually. In order to minimize the effects of possible field instabilities, the following sampling order was performed:

1. Dummy excitations
2. Water reference for each *k*-space line
3. One edit-on and one edit-off acquisition of the first *k*-space line
4. Repeat for all other *k*-space lines
5. Possible repetition of editing acquisitions in identical fashion

Difference artifacts are the biggest source of error. While the effects of phase and frequency variations can be mitigated in preprocessing, this does not hold true for possible amplitude changes. Therefore, the order that minimizes the time between identical *k*-space lines for both subspectra was selected. Artifacts in image reconstructions can be introduced by field instabilities between *k*-space lines. Therefore, complete *k*-space coverage was aimed to be as fast as possible to reduce these artifacts. Repetition of the measurement can be used to increase the SNR.

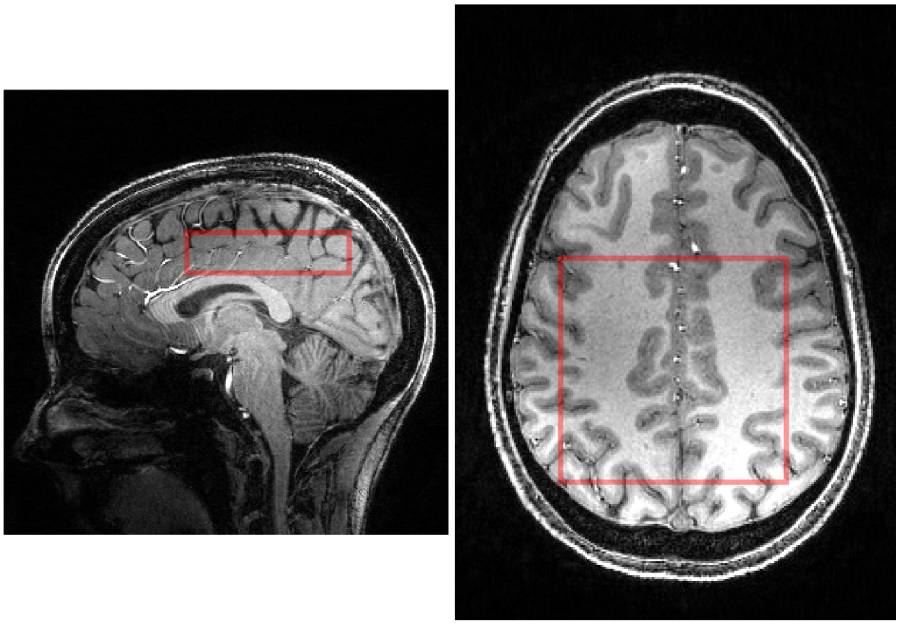

Figure 5.2: T_1-weighted MP-RAGE image from the measured subjec, overlapped with the selected region of interest (in red). The slice is directly placed above the corpus callosum. The region of interest is moved slightly to the back of the head. EPSI readout is performed in left-right direction.

5.3 *In-vivo* application of MEGA-sLASER EPSI

To explore the possible application of spectroscopic imaging of GABA, the MEGA-sLASER EPSI sequence was tested *in-vivo* in one healthy volunteer.

5.3.1 Methods

Data acquisition

Identical to the single voxel experiments, an MP-RAGE sequence was used to acquire a high-resolution, whole-brain T_1 weighted image. Based on this image, a (8x8x2) cm^3 region of interest and a concentric (16x16x2) cm^3 field of view (FOV) was placed. The region of interest can be seen in Figure 5.2. Shim and B_1 calibration was performed identically to the single voxel experiments. Afterwards, a SVS MEGA-sLASER sequence was used to obtain one water reference and one edit-on and edit-off spectrum from the selected region of interest.

A 16x16 voxel EPSI readout was used to sample the FOV, resulting in a resolution of (1x1x2) cm^3. After 4 dummy excitation, a water reference and 12 repetitions of edit-on and edit-off (6 times each) were measured using MEGA-sLASER EPSI. Therefore, $16 \cdot 13 + 4 = 212$ excitation were necessary, while SAR restrictions allowed for $T_R = 5.34$ s. Thus, the total acquisition time was 18:52 min.

Data Processing

Preprocessing was performed using the complete processing pipeline described in chapter 3.5. This includes the MRSI acquisition as well as an additionally acquired SVS water signal with the same ROI and a whole-brain B_1 map.

In the first step, coil combination was performed. Using the SVS data, coil weight were calculated and applied to the MRSI data (see chapter 3.1.1). Image reconstruction (see chapter 3.1.2) was performed with the coil combined data. This included Hamming filtering and center of mass shifting.

After image reconstruction is completed, the signal of every voxel is treated individually, following the optimized data processing pipeline established for the SVS experiments. Using the water reference image, every spectrum is eddy-current corrected (see chapter 3.1.4). As it performed best in the SVS experiments, SRmeo (see chapter 3.1.5) was used to phase and frequency correct the signals of the individual repetitions. Finally, DAS (see chapter 3.1.6) is used to remove residual frequency and phase differences of the averaged edit-on and edit-off spectrum.

TARQUIN was again used for spectral quantification. Identical setting to the reference study was used for the quantification of edit-off and difference spectra.

B_1 correction

The RoI in the MRSI experiment contains a large part of the brain. Therefore, substantial B_1 variations are to be expected between the voxels. However, the voxel size is relatively small (only 2 µl), and the intra-voxel B_1 variation is expected to be negligible. Therefore, the B_1 correction is performed using the averaged intra-voxel B_1.

The acquired B_1 map has a much higher resolution than the EPSI sequence. Therefore, the averaged intra-voxel B_1 can be inferred from all voxels of the B_1 map that at least partially lie inside the respective MRSI voxel. Using these values, the simulated editing efficiency (see chapter 3.3.1) can be calculated for every voxel, and the measured GABA/creatine ratios are scaled accordingly.

Segmentation

The volume of the individual voxels is reduced by more than a factor of 10 compared to the SVS experiments. However, partial volume effects are still present. Using FSL-flirt [107], anatomical images can be segmented into gray-matter, white-matter, and CSF regions. Each voxel of the MPRAGE image is put into one of these groups. As different GABA concentrations in gray matter and white matter have previously been reported, the gray-matter fraction (GMF) of each MRSI voxel is calculated. The GMF is defined as the number of gray matter voxels divided by the combined number of gray matter and white matter voxels.

Quality control

Multiple steps of quality control are performed. In the first step, the spectral quality is inspected analogously to the SVS experiments (see chapter 4.5.3). This includes a visual inspection of the

individual spectra to check for artifacts. Additionally, the SNR and FWHM were extracted from the TARQUIN output. One parameter of the TARQUIN fit is the reference frequency. This is the water frequency to which the spectra are shifted during spectral quantification, which is a measure of local B_0. As ECC shifts the spectra according to the water signal, the data had to be analyzed again without ECC for meaningful measures of the reference frequency.

The most simple image-based quality metric is coefficient of variation of the GCRs within the ROI. However, this metric does not discriminate between variations, which are caused by physiological differences from measurement instabilities or systematic error.

The presented method requires a correction for the inhomogeneous B_1. Consequently, significant B_1 dependence of the corrected GCR might indicate a systematic problem with the B_1 correction. Therefore, a linear fit of both the corrected and the uncorrected GCR to the local B_1 is performed to investigate whether the B_1 correction completely removes any B_1 dependence.

Higher GABA concentration is expected in gray matter. Thus, a linear fit of the B_1 corrected GCR to the GMF of the individual voxels should lead to a significant dependence. Ideally, this contrast is so high that anatomical features can be seen in the GCR map. Note that a possible, anatomically explained correlation between local B_1 and GMF might explain residual B_1 dependence of the measured GCR.

Some additional potential sources of estimation error were investigated similarly. The measured GABA concentration should not depend on the spectral quality or local B_0. Consequently, linear fits of the GCR as a function of FWHM and SNR were performed.

5.3.2 Results

Data quality

Figure 5.3 depicts the acquired edit-on, edit-off, and difference spectra from a central voxel (top) and an edge voxel of the region of interest (bottom). The spectra look similar to the SVS spectra (see Figure 4.9) but with reduced SNR. In the central voxel, the GABA resonance at 3.01 ppm can be clearly seen, while it is difficult to see GABA in the edge voxel. The average NAA line width, extracted from the TARQUIN fit, within the ROI in the difference spectra is 10.5 Hz, and the average SNR is 21.6. When only the central 36 voxels, the average SNR increases to 27.4, and the average FWHM is 10.9 Hz.

Although there is similar line width in the EPSI experiment and the PCC SVS experiments, the measured difference of SNR is a factor of 8, when SNR is averaged over all voxels within the region of interest. When only the central voxels are considered, this drop is only 6.13. The SNR loss is caused by the small voxel size of only 2 cm^3, compared to 27 cm^3 in the PCC experiment, which would lead to an SNR reduction of a factor of 13.5. However, there are multiple effects, which cause an increase of SNR. The signal is averaged over 3 times the excitations, which would result in an increase of SNR by a factor of $\sqrt{3}$, if equal T_R were used. Due to a reduced steady-state magnetization, the SNR increase is only a factor of 1.71. Furthermore, the effective dwell time is longer. Thus, an additional SNR increase of a factor of 1.22 is expected. Combining these effects, an SNR drop of 6.47 would be expected.

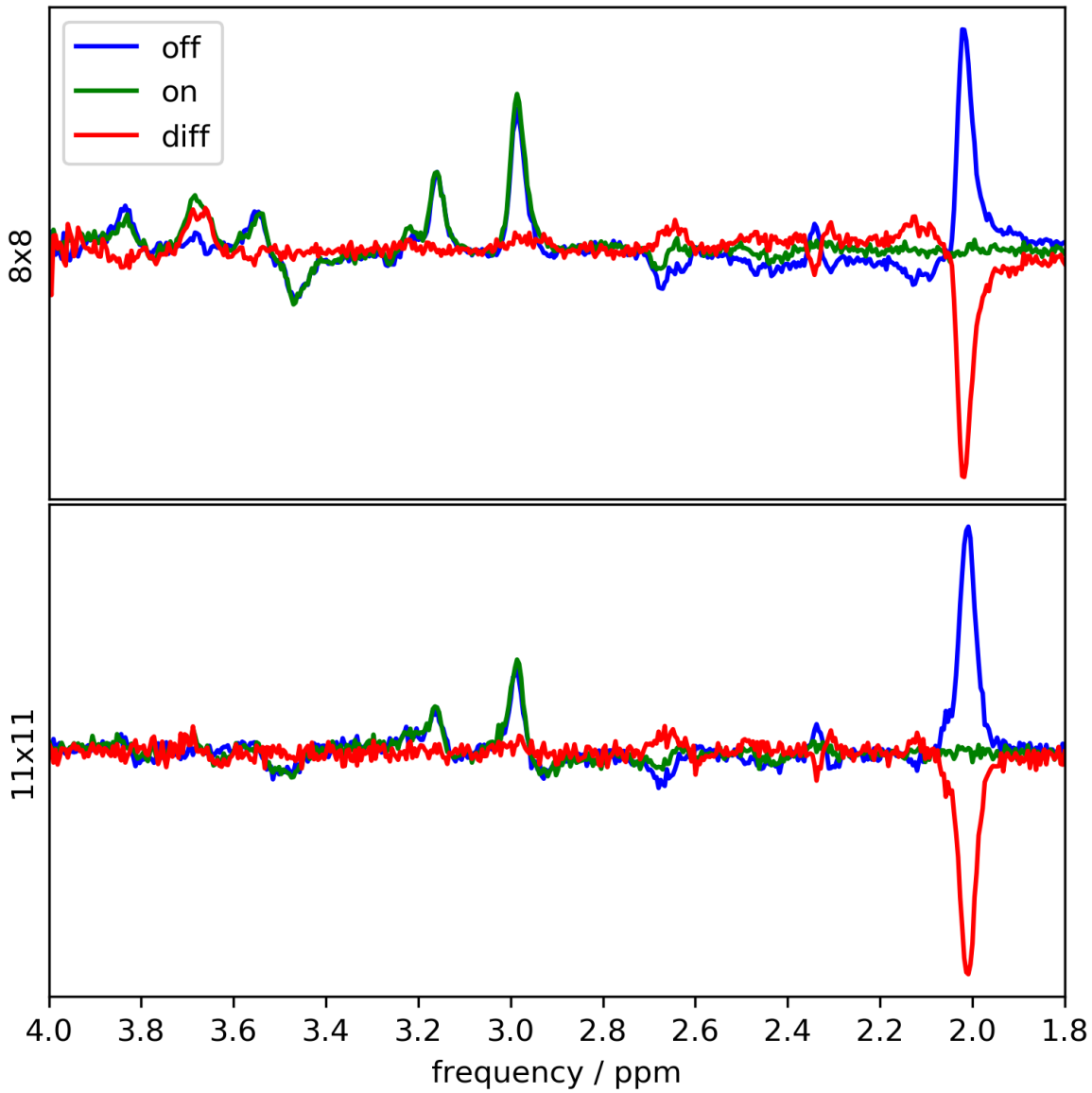

Figure 5.3: Edit-off (blue), edit-on (green), and difference (red) spectra from a central voxel (top) and a voxel at the corner of the region of interest (bottom). Very similar spectra to the SVS experiments were found, but with a much higher noise level. Spectral quality deteriorates in the outer voxel.

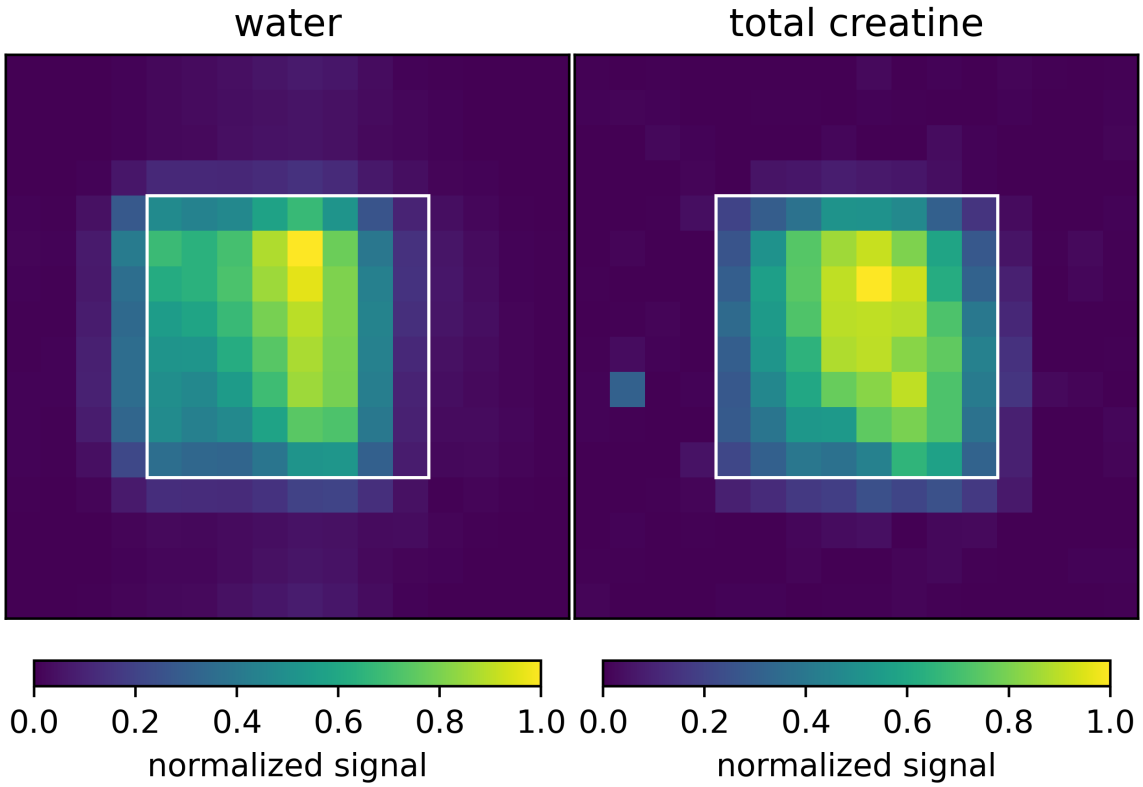

Figure 5.4: Normalized signal strength of the water resonance (left) and creatine signal strength (right). The white box marks the nominal region of interest. The CSDE is clearly seen in left-right direction in the water map.

Water reference and creatine map

Figure 5.4 shows the maximum of the water reference signal and the creatine signal on the left and right sides, respectively. In both maps, the white square marks the nominal position of the region of interest. The water signal is detuned by 2.4 ppm (713 Hz). This corresponds to 21% (1.72 voxels) in phase and 4 % (0.34 voxels) in readout direction. The resulting chemical shift error is clearly visible in the map. The detuning of creatine is much smaller; only 0.43 pixels in phase and 0.08 pixels in readout direction. However, this shift cannot easily be seen in the creatine map.

Both maps feature a similar intensity pattern, which is primarily caused by a combination of two effects. The non-uniform B_1 distribution and different coil sensitivities for the individual voxels. Both effects are more pronounced for the outer voxels, where a poor slice profile causes a further reduction of signal strength. This causes an apparent increase of water and creatine signal in the center of the region of interest.

The imperfect coil combination will scale the GABA signal in the same way as the creatine signal. With the exception of the editing efficiency, the B_1 distribution will also affect GABA and creatine equally. Thus, no correction for the center brightening of the creatine map is needed, as the effect will be canceled, when calculating the signal ratio.

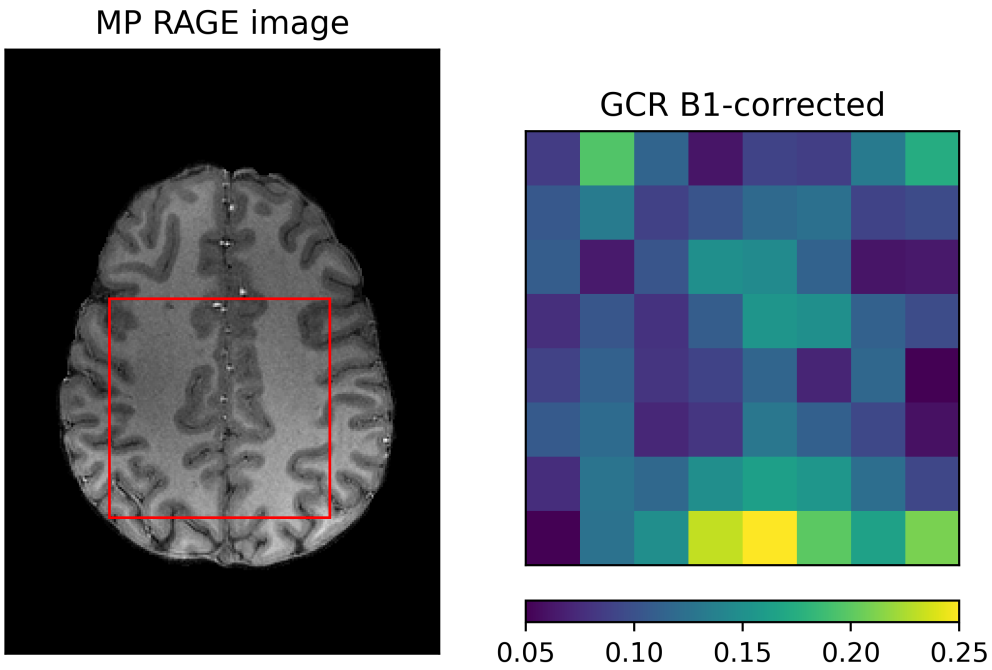

Figure 5.5: Left: One slice of the MPRAGE acquisition that lies in the middle of the ROI of the EPSI sequence, which is indicated by the red box. Right: Map of the B_1 corrected GABA to creatine ratio

In contrast to the SVS experiments, where spurious echoes could be observed, no artifacts could be found in the spectra by visual inspection. Also, no difference artifacts were found, which might have been caused by insufficient frequency and phase correction.

GABA / creatine ratio map

In Figure 5.5, the measured B_1 corrected GCR is plotted (right). On the left-hand side, one slice of the anatomical acquisition is shown. The red square marks the ROI of the MRSI experiment. At the edges of the ROI, very high and very low GCR values can be found, while in the central area, this variation is reduced. However, it is very hard to see any anatomical pattern in the GCR maps outside a small increase of GCR in the central voxels.

When all 64 voxels within the FoV are considered, the CoV of the GCR is 37.1 %. However, The outermost voxels suffer from poor slice profiles and from the 4-compartment artifact. Consequently, the CoV of the GCR is reduced to 24.1 % when only the central 36 voxels are considered. This drop is expected because of the poor slice profile of the excitation pulse and the 4-compartment artifact. Consequently, only the central 36 voxels will be used from now on.

Local B_1 map and resulting editing efficiency

Figure 5.6 shows the flip angle distribution and the resulting editing efficiency of each voxel. The B_1 field is quite stable in the center and drops slightly in amplitude for the outer volumes. The maximal flip angle was around 180 °, and on the edges, it dropped to slightly above 140 °.

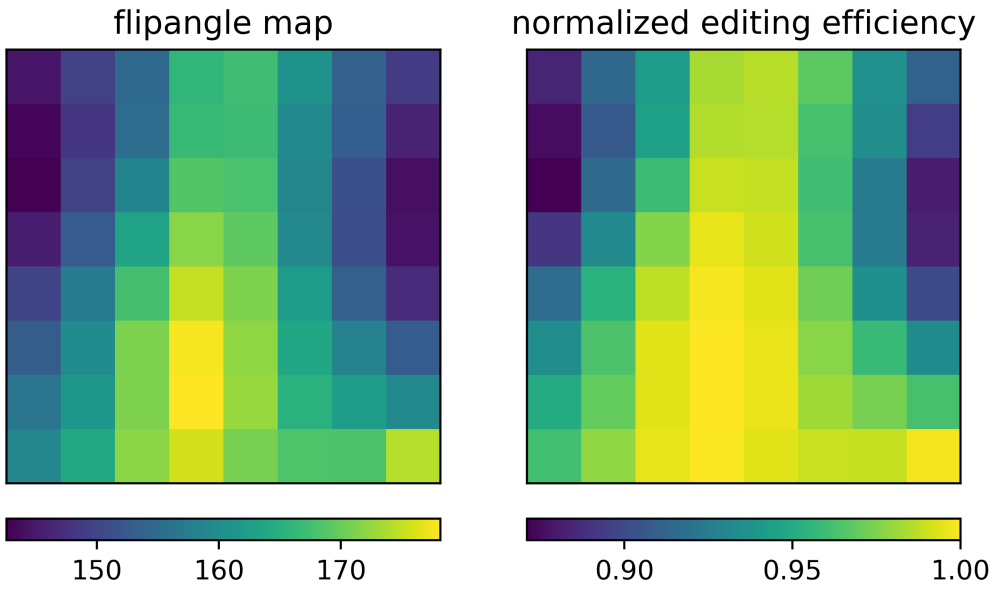

Figure 5.6: Variation of the flip angle (left) and the expected editing efficiency (right) of GABA within the region of interest.

All voxels have an expected relative editing efficiency of above 0.85, and the central 36 are even above 0.9. As expected, the B_1 distribution is roughly symmetrical in left-right direction.

Figure 5.7 shows the GCR maps before (top left) and after (top right) editing efficiency correction. The correction increases the estimated GCR in the outer parts of the FoV. The bottom plot shows the measured GCR before (blue) and after (red) editing efficiency correction. This includes linear fits. Without this correction, a significant trend ($R = 0.36$, $p = 0.034$) can be observed. This trend can be compensated for using editing efficiency correction, and no significant trend can be observed afterwards ($R = 0.27$, $p = 0.12$). Apparently, the B_1 correction removes the effect of inhomogeneous editing efficiency robustly.

Dependence on voxel composition

Figure 5.8 shows the GMF of each voxel in the FoV (top left) and the B_1 corrected GCR map (top right). Very high values can be found in along the central columns, as much gray matter is present near the interhemispheric fissure. As the FoV was manually placed, its center does not lie exactly in the interhemispheric fissure. This causes an asymmetry in the GMR map. The right central column contains more gray matter than the left central column because of this asymmetry. The segmented MPRAGE image can be found in Figure A.4 in the appendix.

The bottom plot shows the GCR as a function of GMF, including the linear regression ($R = 0.49$, $p = 0.0026$). Voxels with high gray matter fractions tend to have higher GABA concentration which is consistent with previously reported findings [67, 68]. This relatively low correlation coefficient indicates that the majority of the variation is caused by measurement instabilities instead of physiological properties. However, a significant dependence of the GCR on the voxel composition can be observed.

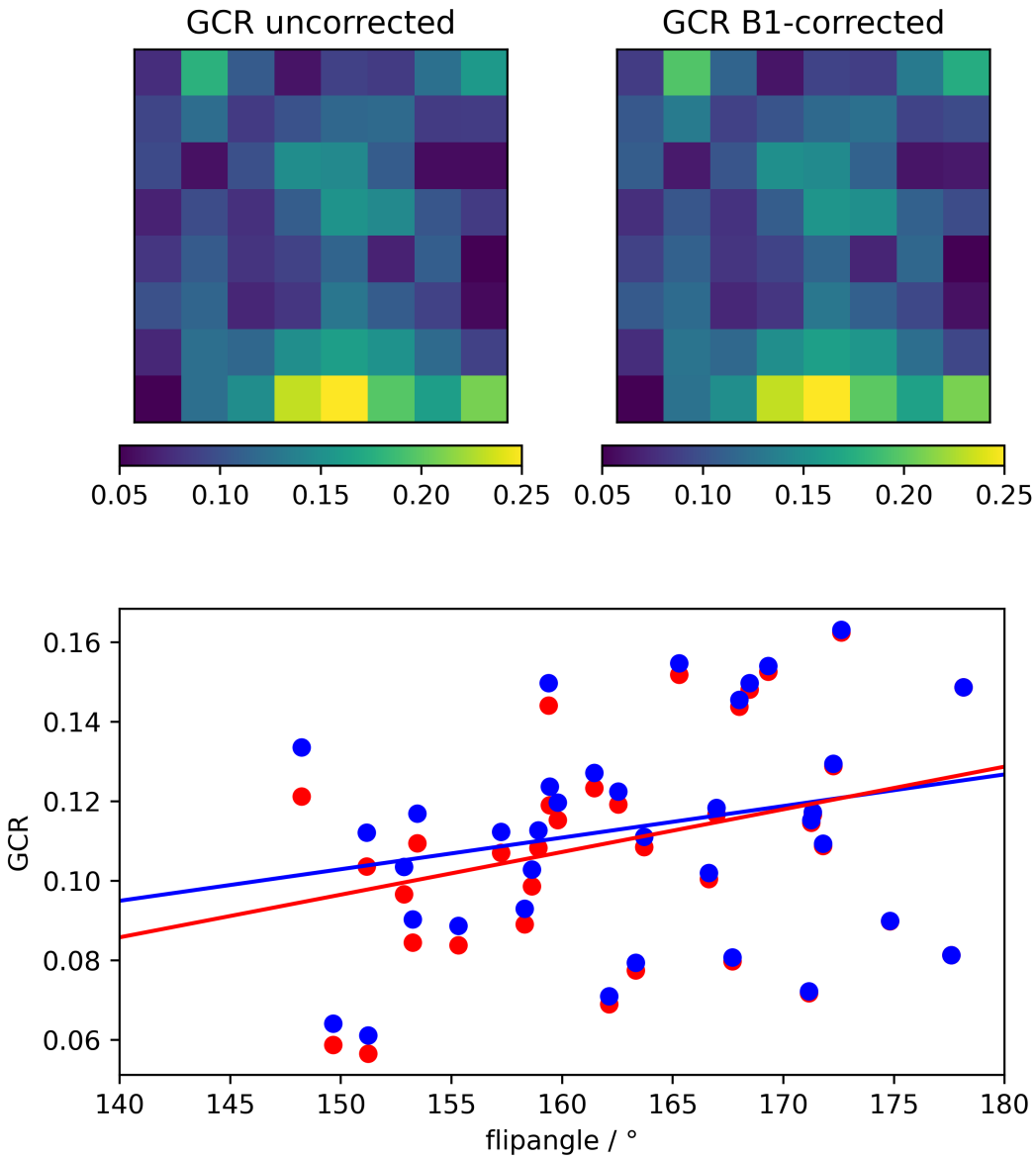

Figure 5.7: Local flip angle of the editing pulses (top left) and map of the B_1 corrected GCR (top right). The bottom shows the GCR as a function of local B_1 for the central 36 voxels. The red line shows the linear regression

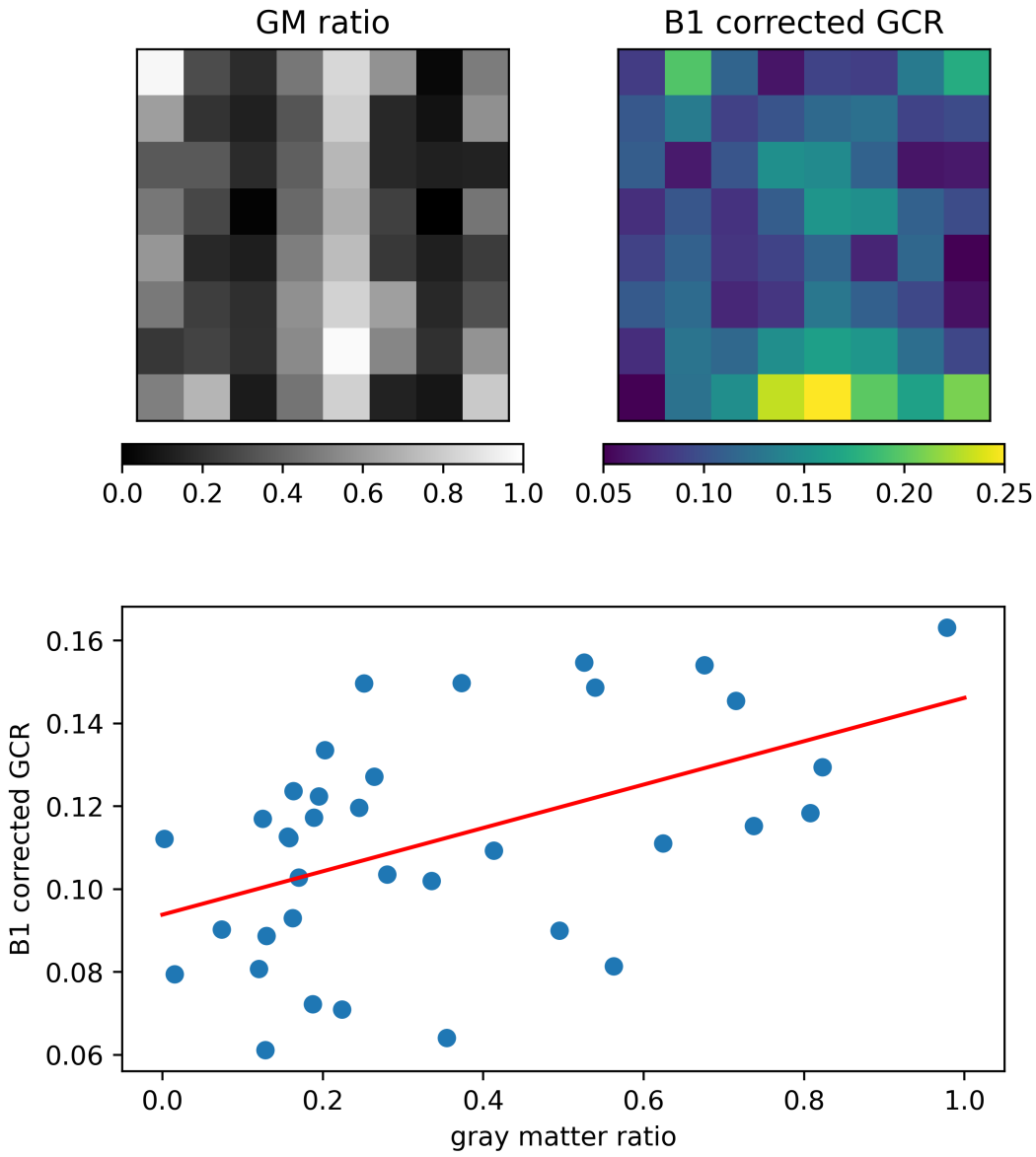

Figure 5.8: Gray matter fraction of each voxel (top left) and map of the B_1 corrected GCR (top right). The bottom shows the GCR as a function of the GMF for the central 36 voxels. The red line shows the linear regression.

	R	p
GMF	0.49	0.0026
FWHM	0.27	0.11
B_1	0.27	0.12
SNR	0.034	0.85
B_0	0.019	0.91 height

Table 5.1: Summary of the correlation of the editing efficiency corrected GCR to all metrics investigated in this chapter. The only significant correlation could be found between GABA concentration and the gray matter fraction.

Other potential dependencies

The dependence of the editing efficiency corrected GCR on the spectral quality, and local B_0 was investigated. Figure A.5 in the appendix depicts the editing efficiency corrected GCR as a function of SNR, FWHM, and reference frequency. This also includes linear fits. No significant correlation was found for the SNR ($R = 0.034$, $p = 0.85$), FWHM ($R = 0.27$, $p = 0.11$) or local B_0 ($R = 0.019$, $p = 0.91$). Therefore, no systematic quantification error has been introduced by any of these metrics.

In Table 5.1, the correlation between the GABA concentration and all presented metrics is summarized. The gray matter fraction is the only investigated metric with a significant correlation to the editing efficiency corrected GCR.

5.3.3 Discussion

Initial results show that GABA concentration measures can be performed at 7 Tesla using MEGA-sLASER EPSI in principle. The GABA to creatine ratio (GCR) was measured in a 2 cm thick slice with 1 cm in-plane resolution in less than 20 minutes. Reasonable GCRs could be measured with a moderate CoV. However, the measured GCR maps are dominated by measurement instability. Nevertheless, a clear correlation between the gray matter fraction within the voxel and the GABA concentration is found. In agreement with previous studies [67, 68], the GABA concentration was found to be higher in gray matter. This is a very promising finding, but as measurement instabilities dominate the measured GCR, the presented method lacks the sensitivity to map the spatial distribution of the GABA concentration in a routine setting.

Without correcting for the inhomogenous editing efficiency, the measured GABA concentration significantly depends on the local B_1. After editing efficiency correction, no significant dependence can be observed. Editing efficiency correction only takes into account the GABA signal. However, the measured GABA signal is not pure, as macromolecular contribution exists. This macromolecular contribution is also affected by B_1 inhomogeneities. As the macromolecular resonance is not targeted by the editing pulses, their editing efficiency will depend differently on B_1. As these signals cannot be separated, it is expected that a systematic B_1 dependent error is introduced. This error cannot be found in the data. However, given the high variation in GCR it is possible that the sensitivity is not high enough to detect this residual B_1-dependence. This

potential error could be minimized by including macromolecular suppression in the sequence. However, this suppression is expected to introduce a further increase of variation in the GCR, which would likely further reduce the sensitivity of this method.

No artifacts were found in the spectra. While the SNR is strongly reduced, compared to the SVS experiments, it is sufficient to effectively compensate for phase and frequency variations. Furthermore, no significant dependence of the measured GABA concentration on local B_0 or the spectral quality could be found. Therefore, the limited sensitivity of the presented method is likely caused by an unstable quantification due to a lack of SNR.

The main problem of the presented approach is the low SNR in the spectra. Increasing the SNR is possible by increasing the number of excitations. As this would prolong the measurement, which is already quite long, this is not a feasible approach. Data quality assessment suggests that the loss of SNR is larger than expected by the acquisition parameters. Thus, the data processing can still be optimized. The water maps indicate an imperfect coil combination. A promising way of increasing the SNR is implementing a coil combination approach that is specially designed for MRSI data, like MUSICAL [115]. This way, the ideal coil weight of the individual voxels can be accessed. However, these methods require additional data acquisition. Intra-voxel differences in coil sensitivity are also present in SVS experiments, especially in large voxels. Thus, this approach can potentially increase SNR per volume beyond the SVS SNR. One downside of the EPSI sequence, as presented here, is that no sampling is performed during the ramp time. The duty cycle is defined as the percentage of time during the readout when data is sampled. The lower the duty cycle, the more SNR is lost. This drop in SNR can only partially be restored by employing ramp sampling [116].

Increasing the resolution of the EPSI readout requires stronger gradients and, thus, longer ramps. The duty cycle can be improved by prolonging the dwell time, and sacrificing more spectral bandwidth. With this method, an in-plane resolution of 5 mm can be achieved [117]. Another possibility is to use more elaborated k-space trajectories, like concentric rings [118]. However, with the presented acquisition method, the GABA SNR does not allow for an increase in resolution.

In 2019 Magnussen et al. [93] published a very similar approach, which is also based on MEGA-sLASER EPSI. Although there were substantial inter-subject differences in editing efficiency corrected GCR maps, an increase in measured GABA concentration in the central brain can be consistently observed. This finding is consistent with the previously reported higher GABA concentration in gray matter, which could also be observed in the data presented in this thesis.

One intrinsic problem of the MEGA-sLASER approach is the long repetition time, which is enforced by the high SAR. This not only causes an SNR-inefficient acquisition but also increases the time needed for k-space coverage. Recently, alternative MRSI-specific sequences have been proposed that reduce the number of pulses needed and consequently, SAR. In 2019 Moser et al. [119] published a different approach to J-edited GABA MRS, based on a one-dimensional sLASER and adiabatic MEGA pulses. As the echo time has to be kept identical (see chapter 2.2.7), more time can be spent on the editing pulses. This allows for adiabatic editing pulses, mitigating the problems of B_1 inhomogeneities. In their work, GABA concentrations were elevated in gray matter, and the resulting GABA concentration maps show an impressive gray matter to white matter contrast.

In 2022 Weng et al. [120] introduced SLOW-editing, an alternative to the MEGA approach, which only uses refusing pulses with different bandwidths to create two subspectra with different coherence pathways. This further reduces the necessary SAR and might allow for very short repetition times. Both of these newly developed methods cannot be applied to SVS as they lack spatially selective refocusing. Therefore, a whole slice is selected.

Although some improvements can be implemented to the presented MRSI approach, future work on GABA MRSI should focus on these newly presented sequences.

CHAPTER 6

Conclusion and Outlook

Magnetic resonance spectroscopy (MRS) gives unique insides into the biochemistry of living tissue in a non-invasive manner. This method strongly benefits from the relatively recent introduction of ultra-high field scanners with a main magnetic field of 7 Tesla and higher for human use. MRS is of special interest in neuro-imaging, as it allows to measure the *in-vivo* concentration of brain metabolites. By combining MRS with MR imaging techniques, magnetic resonance spectroscopic imaging (MRSI) allows measuring the spatial distribution of these concentrations. Improving MRSI methods has been a major research topic in the last couple of years.

Gamma-amino butric acid (GABA) is the principal inhibitory metabolite in the human brain, and variations of its concentration can be linked to a great variety of neurological, psychological, and neurodegenerative diseases. Therefore, it has been a prime target of MRS and MRSI for several decades. The low GABA concentration and the signal overlap of more prominent brain metabolites hamper GABA MRS. This is especially true for MRSI.

J-editing is an MR spectroscopic technique, which is often used for GABA spectroscopy. Spectrally selective editing pulses perturb the spins of one GABA resonance frequency. Due to internal coupling mechanisms, this affects the shapes of other resonances. Spectra are acquired with and without these pulses. While the GABA shapes of the GABA resonances differ, this is not the case for overlapping resonance, which lack a coupling partner at the frequency that is selected by the editing pulses

Two main experiments were presented in this thesis. The first experiment focussed on single voxel spectroscopy of GABA in the human hippocampus utilizing. This brain region is linked to numerous diseases, including Alzheimer's. In this brain region, susceptibility differences cause severe B_0 inhomogeneities, which strongly impair spectral quality. While multiple MRS studies in the hippocampus have previously been performed, no hippocampal GABA concentration has been reported. The reduced spectral quality rendered many optimizations of the acquisition process, measurement sequence, preprocessing, and spectral quantification necessary.

A MEGA-sLASER sequence was implemented as a first step. MEGA-sLASER includes *J*-editing into an ultra-high field optimized sequence. Using classical and quantum mechanical simulations, the pulses within this sequence were optimized to maximize the GABA signal. It was found that the sequence was prone to spurious echoes, which arise from areas outside the

selected region of interest. To remove these echoes, a 16-step phase cycling and strong spoiler gradients were implemented. Only in one subject could these echoes be observed afterwards. The strong spoiler gradients caused substantial eddy currents, which were not sufficiently compensated for by the scanner model. Additionally, a preparation study was performed to identify the optimal shimming process. 3rd order shimming significantly outperformed 2nd order shimming. However, during this preparation study, the scan was stopped twice for technical reasons when 3rd order shimming was activated. Therefore, it was decided not to use it. Afterwards, the optimal data processing pipeline is identified. This included two parameters of the spectral quantification process and multiple preprocessing approaches. The main source of error was phase and frequency variations, which could best be compensated for by spectral registration using a joined reference signal and additional difference artifact suppression. Additionally, eddy-current compensation removed the quantification error that was introduced by the strong crusher gradients. A reference study in the posterior cingulate cortex showed that the limited spectral quality, caused by the strong field inhomogeneity, is the main source of measurement error.

With this workflow, the GABA to creatine ratio could be measured with an inter-subject coefficient of variation of around 12 %. This is comparable to literature values from more accessible brain regions and allows the routine use of hippocampal GABA MRS in upcoming clinical studies.

Using single-voxel spectroscopy (SVS) measures the metabolite concentrations only in a small region and does not allow to measure the spatial distribution of these concentrations. This would be very interesting for investigating neurodegenerative diseases that usually affect large areas of the brain. However, the small voxel size reduces the SNR compared to SVS. Furthermore, large-scale B_1 differences make J-editing challenging at ultra-high field as the editing efficiency will vary, depending on the local B_1. Therefore, the MEGA-sLASER sequence was extended by an EPSI-readout to measure the spatial distribution of the GABA concentration. Additionally, a data analysis pipeline was implemented. This sequence was tested in one young, healthy volunteer.

Image reconstruction, which included k-space filtering and compensating for k-space distortions, was performed. Afterwards, the metabolic concentrations were estimated for each voxel individually, using the workflow established for the SVS experiment. As the flip angle of the editing pulses varies between individual voxels because of the B_1 profile, a correction factor for the GABA concentration was introduced. This factor is based on simulating the GABA signal and the local B_1. Furthermore, the gray matter fraction was extracted from the anatomical reference scan for each voxel.

Reasonable GABA concentration estimates were made with a moderate inter-voxel variation. The significant correlation between the measured GABA concentration and the local B_1 could be removed by editing efficiency correction. Also, no significant dependence of the GABA concentration on the spectral quality could be found. Instead, a significant correlation to the gray matter fraction could be found, with higher GABA concentrations in gray matter, which is consistent with previous studies. However, most variation in GABA concentration is caused by measurement instabilities.

Although the dependence of the GABA concentration on the gray matter fraction is promising, the presented method is not sensitive enough to be used in clinical studies. Recently, two different

sequences have been proposed for GABA MRSI that might lead to substantial improvements of the GABA MRSI. Future work should focus on these methods instead of the presented one.

After the data acquisition for this thesis was completed, the 7 Tesla scanner was upgraded. The 3rd order shimming and parallel transmit capabilities of the scanner are now embedded into the main functionality of the scanner. This allows reliable usage of both techniques. Especially the SVS hippocampus spectroscopy will profit from this, as 3rd order shimming was demonstrated to yield better spectral quality, which is the main limitation of this method. B_1 shimming may lead to reduced SAR and allow T_R reduction and, consequently, an improved SNR. Both would reduce the quantification error.

The spectral line width of the GABA MRSI is very low already. Consequently, no significant increase in data quality is to be expected by using 3rd order shimming. However, spectroscopic imaging using J-editing can profit from B_1 shimming, as the influence of editing efficiency variation might be reduced.

Bibliography

[1] F. Bloch and A. Siegert, *Magnetic resonance for nonrotating fields*, Physical Review **57**.6 (1940) 522, ISSN: 0031899X (cit. on pp. 1, 7).

[2] E. M. Purcell, *Resonance Absorption by Nuclear Magnetic Moments in a Solid*, Phys. Rev **69** (1946) (cit. on p. 1).

[3] R. R. Ernst and W. A. Anderson, *Application of fourier transform spectroscopy to magnetic resonance*, Review of Scientific Instruments **37**.1 (1966) 93, ISSN: 00346748 (cit. on pp. 1, 13, 21).

[4] R. B. Moon and J. H. Richards, *Determination of intracellular pH by 31P magnetic resonance.*, eng, The Journal of biological chemistry **248**.20 (Oct. 1973) 7276, ISSN: 0021-9258 (Print) (cit. on p. 1).

[5] D. I. Hoult et al., *Observation of tissue metabolites using nuclear magnetic resonance*, Nature **252**.5481 (1974) 285, ISSN: 00280836 (cit. on p. 1).

[6] P. A. Bottomley et al., *In vivo solvent-suppressed localized hydrogen nuclear magnetic resonance spectroscopy: A window to metabolism?*, Proceedings of the National Academy of Sciences of the United States of America **82**.7 (1985) 2148, ISSN: 00278424 (cit. on p. 1).

[7] S. W. Provencher, *Automatic quantitation of localized in vivo 1H spectra with LCModel*, NMR in Biomedicine **14**.4 (2001) 260, ISSN: 09523480 (cit. on pp. 2, 38).

[8] R. A. E. Edden et al., *Gannet: a batch-processing tool for the quantitative analysis of GABA-edited MRS spectra*, J Magn Reson Imag **40**.6 (2014) 1445, ISSN: 15378276 (cit. on pp. 2, 38).

[9] D. Stefan et al., *Quantitation of magnetic resonance spectroscopy signals: The jMRUI software package*, Measurement Science and Technology **20**.10 (2009), ISSN: 13616501 (cit. on pp. 2, 38, 40).

[10] M. Wilson et al., *A constrained least-squares approach to the automated quantitation of in vivo* $_1$*Hmagneticresonancespectroscopydata*, Magnetic Resonance in Medicine **65**.1 (2011) 1, ISSN: 07403194 (cit. on pp. 2, 24, 38).

[11] T. R. Brown, B. M. Kincaid and K. Ugurbil, *NMR chemical shift imaging in three dimensions*, Proceedings of the National Academy of Sciences of the United States of America **79**.11 I (1982) 3523, ISSN: 00278424 (cit. on p. 2).

[12] A. A. Maudsley et al.,
Spatially resolved high resolution spectroscopy by "four-dimensional" NMR,
Journal of Magnetic Resonance (1969) **51**.1 (1983) 147, ISSN: 00222364 (cit. on p. 2).

[13] S. Posse, C. DeCarli and D. Le Bihan, *Three-dimensional echo-planar MR spectroscopic imaging at short echo times in the human brain.*,
Radiology **192**.3 (1994) 733, PMID: 8058941,
eprint: https://doi.org/10.1148/radiology.192.3.8058941
(cit. on pp. 2, 23).

[14] D. A. McCormick, *GABA as an inhibitory neurotransmitter in human cerebral cortex*,
Journal of Neurophysiology **62**.5 (1989) 1018, PMID: 2573696,
eprint: https://doi.org/10.1152/jn.1989.62.5.1018 (cit. on pp. 2, 25).

[15] M. C. Angulo et al., *GABA, a forgotten gliotransmitter*,
Progress in Neurobiology **86**.3 (2008) 297, ISSN: 0301-0082 (cit. on pp. 2, 25).

[16] U. E. Emir, P. J. Tuite and G. Öz, *Elevated pontine and putamenal gaba levels in mild-moderate parkinson disease detected by 7 tesla proton mrs*, PLoS ONE **7**.1 (2012), ISSN: 19326203 (cit. on pp. 2, 26).

[17] L. M. Rowland et al., *Medial Frontal GABA is Lower in Older Schizophrenia: A MEGA-PRESS with Macromolecule Suppression Study*,
Molecular Psychiatry **21**.2 (2016) 198 (cit. on p. 2).

[18] Z. Bhagwagar et al.,
Reduction in Occipital Cortex γ-Aminobutyric Acid Concentrations in Medication-Free Recovered Unipolar Depressed and Bipolar Subjects,
Biological Psychiatry **61**.6 (2007) 806, ISSN: 00063223 (cit. on pp. 2, 26).

[19] M. Mescher et al., *Simultaneous in vivo spectral editing and water suppression*,
NMR in Biomedicine **11**.6 (1998) 266, ISSN: 09523480 (cit. on pp. 2, 18).

[20] H. Wang et al., *Magnetic Resonance Spectroscopy in Alzheimer's Disease: Systematic Review and Meta-Analysis*, Journal of Alzheimer's Disease **46**.4 (2015) 1049,
ISSN: 18758908 (cit. on p. 2).

[21] C. G. Choi and J. Frahm, *Localized proton MRS of the human hippocampus: Metabolite concentrations and relaxation times*, Magnetic Resonance in Medicine **41**.1 (1999) 204,
ISSN: 07403194 (cit. on p. 2).

[22] J. Steinke et al., *Hippocampal metabolism and prefrontal brain structure: A combined 1H-MR spectroscopy, neuropsychological, and voxel-based morphometry (VBM) study*,
Brain Research **1677** (2017) 14, ISSN: 18726240 (cit. on pp. 2, 38).

[23] N. Allaıli et al., *Single-voxel 1H spectroscopy in the human hippocampus at 3 T using the LASER sequence: characterization of neurochemical profile and reproducibility*,
NMR in Biomedicine **28**.10 (2015) 1209,
eprint: https://onlinelibrary.wiley.com/doi/pdf/10.1002/nbm.3364
(cit. on p. 2).

[24] Y. Völzke et al., *On the reproducibility of hippocampal MEGA-sLASER GABA MRS at 7T using an optimized analysis pipeline*,
Magnetic Resonance Materials in Physics, Biology and Medicine (2020),
ISSN: 13528661 (cit. on pp. 3, 53).

[25] W. C. Dickinson,
Dependence of the F^{19} *Nuclear Resonance Position on Chemical Compound*,
Phys. Rev. **77** (5 Mar. 1950) 736 (cit. on p. 7).

[26] W. G. Proctor and F. C. Yu, *The Dependence of a Nuclear Magnetic Resonance Frequency upon Chemical Compound*, Phys. Rev. **77** (5 Mar. 1950) 717 (cit. on p. 7).

[27] H. S. Gutowsky, D. W. McCall and C. P. Slichter,
Coupling among Nuclear Magnetic Dipoles in Molecules,
Phys. Rev. **84** (3 Nov. 1951) 589 (cit. on p. 8).

[28] J. A. Pople, W. G. Schneider and H. J. Bernstein,
THE ANALYSIS OF NUCLEAR MAGNETIC RESONANCE SPECTRA: II. TWO PAIRS OF TWO EQUIVALENT NUCLEI, Canadian Journal of Chemistry **35**.9 (1957) 1060,
eprint: `https://doi.org/10.1139/v57-143` (cit. on p. 9).

[29] H. S. Gutowsky et al., *Electron Coupling of Nuclear Spins. I. Proton and Fluorine Magnetic Resonance Spectra of Some Substituted Benzenes*,
Journal of the American Chemical Society **79**.17 (1957) 4596, ISSN: 15205126
(cit. on p. 9).

[30] O. Sørensen et al.,
Product operator formalism for the description of NMR pulse experiments,
Progress in Nuclear Magnetic Resonance Spectroscopy **16** (1984) 163, ISSN: 0079-6565
(cit. on pp. 11, 16).

[31] M. Levitt, *Spin Dynamics: Basics of Nuclear Magnetic Resonance*, Wiley, 2008,
ISBN: 9780470517123 (cit. on p. 11).

[32] F. Bloch, *Nuclear induction*, Physical Review **70**.7-8 (1946) 460, ISSN: 0031899X
(cit. on p. 12).

[33] J. Pauly, D. Nishimura and A. Macovski,
A k-Space Analysis of Small Tip-Angle Excitation, 1989 (cit. on p. 12).

[34] F. J. van de Ven,
Multidimensional NMR in Liquids - Basic Principles and Experimental Methods,
Wiley-VCH, 1995 (cit. on p. 12).

[35] P. Mansfield and A. A. Maudsley, *Planar spin imaging by NMR*,
Journal of Physics C: Solid State Physics **9**.15 (Aug. 1976) L409 (cit. on p. 14).

[36] P. Bottomley, *Selective volume method for performing localized NMR spectroscopy*,
19 (1982) (cit. on p. 15).

[37] G. Bodenhausen, H. Kogler and R. R. Ernst,
Selection of coherence-transfer pathways in NMR pulse experiments,
Journal of magnetic resonance **213**.2 (1984) 276, ISSN: 10960856 (cit. on p. 16).

[38] P. Barker and R. Freeman, *Pulsed Field Gradients in NMR. An Alternative*, Journal of Magnetic Resonance **338** (1985) 334 (cit. on p. 16).

[39] I. Tkáč et al., *In vivo 1H NMR spectroscopy of rat brain at 1 ms echo time*, Magnetic Resonance in Medicine **41**.4 (1999) 649, ISSN: 07403194 (cit. on p. 18).

[40] R. J. Ogg, P. B. Kingsley and J. S. Taylor, *WET, a T1- and B1-insensitive water-suppression method for in vivo localized 1H NMR spectroscopy.* 1994 (cit. on p. 18).

[41] D. A. Yablonskiy et al., *Homonuclear J coupling effects in volume localized NMR spectroscopy: Pitfalls and solutions*, Magnetic Resonance in Medicine **39**.2 (1998) 169, ISSN: 07403194 (cit. on p. 19).

[42] F. T. Hioe, *Solution of Bloch equations involving amplitude and frequency modulations*, Phys. Rev. A **30** (4 Oct. 1984) 2100 (cit. on pp. 19, 20).

[43] M. S. Silver, R. I. Joseph and D. I. Hoult, *Selective spin inversion in nuclear magnetic resonance and coherent optics through an exact solution of the Bloch-Riccati equation*, Phys. Rev. A **31** (4 Apr. 1985) 2753 (cit. on pp. 19, 20).

[44] a. Tannús and M. Garwood, *Adiabatic pulses.*, NMR Biomed **10** (1997) 423, ISSN: 0952-3480 (cit. on pp. 19, 20).

[45] M. Garwood and L. DelaBarre, *The return of the frequency sweep: designing adiabatic pulses for contemporary NMR.*, Journal of magnetic resonance (San Diego, Calif. : 1997) **153** (2001) 155, ISSN: 1090-7807 (cit. on p. 20).

[46] O. C. Andronesi et al., *Spectroscopic imaging with improved gradient modulated constant adiabaticity pulses on high-field clinical scanners.*, Journal of magnetic resonance (San Diego, Calif. : 1997) **203**.2 (Apr. 2010) 283, ISSN: 1096-0856 (cit. on p. 20).

[47] E. Kupče and R. Freeman, *Adiabatic Pulses for Wideband Inversion and Broadband Decoupling*, 1995 (cit. on p. 20).

[48] T. W. Scheenen, A. Heerschap and D. W. Klomp, *Towards1H-MRSI of the human brain at 7T with slice-selective adiabatic refocusing pulses*, Magnetic Resonance Materials in Physics, Biology and Medicine **21**.1-2 (2008) 95, ISSN: 09685243 (cit. on p. 20).

[49] A. Andreychenko et al., *Efficient spectral editing at 7 T: GABA detection with MEGA-sLASER*, Magnetic Resonance in Medicine **68** (2012) 1018, ISSN: 07403194 (cit. on pp. 20, 44).

[50] R. G. Spencer and K. W. Fishbein, *Measurement of Spin-Lattice Relaxation Times and Concentrations in Systems with Chemical Exchange Using the One-Pulse Sequence: Breakdown of the Ernst Model for Partial Saturation in Nuclear Magnetic Resonance Spectroscopy*, Journal of Magnetic Resonance **142**.1 (2000) 120, ISSN: 10907807 (cit. on p. 21).

[51] K. L. Behar et al.,
Analysis of macromolecule resonances in 1H NMR spectra of human brain,
Magnetic Resonance in Medicine **32**.3 (1994) 294, ISSN: 15222594 (cit. on p. 21).

[52] P.-G. Henry et al., *Brain GABA Editing Without Macromolecule Contamination*,
520.May 2000 (2001) 517 (cit. on p. 22).

[53] M. Mikkelsen et al., *Big GABA: Edited MR spectroscopy at 24 research sites*,
NeuroImage **159** (2017) 32, ISSN: 1053-8119 (cit. on pp. 22, 34, 55, 56, 64–66).

[54] C. T. Moonen et al., *Proton spectroscopic imaging of human brain*,
Journal of Magnetic Resonance (1969) **98**.3 (1992) 556, ISSN: 00222364 (cit. on p. 23).

[55] A. Henning et al.,
Slice-selective FID acquisition, localized by outer volume suppression (FIDLOVS) for 1H-MRSI of the human brain at 7 T with minimal signal loss,
NMR in Biomedicine **22**.7 (2009) 683, ISSN: 09523480 (cit. on pp. 23, 69).

[56] P. Mansfield, *Multi-planar image formation using NMR spin echoes*,
J. Phys. C: Solid State Phys **10** (1977) 55 (cit. on p. 23).

[57] (Cit. on p. 24).

[58] J. R. Moffett et al.,
N-Acetylaspartate in the CNS: From neurodiagnostics to neurobiology,
Progress in Neurobiology **81**.2 (2007) 89, ISSN: 03010082 (cit. on p. 24).

[59] C. D. Rae, *A guide to the metabolic pathways and function of metabolites observed in human brain 1H magnetic resonance spectra*, Neurochemical Research **39**.1 (2014) 1,
ISSN: 03643190 (cit. on pp. 24–26).

[60] M. Rango, A. Castelli and G. Scarlato,
Energetics of 3.5 s Neural Activation in Humans: a 31P MR Spectroscopy Study,
Magnetic Resonance in Medicine **38** (1997) 878 (cit. on p. 24).

[61] B. L. Miller et al., *N VIVO 'H MRS CHOLINE: CORRELATION WITH IN VITRO CHEMISTRY/HISTOLOGY*, Life Sciences **58**.22 (1996) 1929 (cit. on p. 25).

[62] E. Roberts, S. Frankel and P. J. Harman, *Amino Acids of Nervous Tissue*,
Proceedings of the Society for Experimental Biology and Medicine **74**.2 (1950) 383,
eprint: `https://doi.org/10.3181/00379727-74-17916` (cit. on p. 25).

[63] N. G. Bowery, A. L. Hudson and G. W. Price,
GABAA and GABAB receptor site distribution in the rat central nervous system., eng,
Neuroscience **20**.2 (Feb. 1987) 365, ISSN: 0306-4522 (Print); 0306-4522 (Linking)
(cit. on p. 25).

[64] C. Rae et al., *Now i know my ABC. A systems neurochemistry and functional metabolomic approach to understanding the GABAergic system*,
Journal of Neurochemistry **109**.SUPPL. 1 (2009) 109, ISSN: 00223042 (cit. on p. 25).

[65] M. Farrant and Z. Nusser,
Variations on an inhibitory theme: Phasic and tonic activation of GABA A receptors,
Nature Reviews Neuroscience **6**.3 (2005) 215, ISSN: 1471003X (cit. on p. 25).

[66] F. A. Chowdhury et al., *Investigation of glutamine and GABA levels in patients with idiopathic generalized epilepsy using MEGAPRESS*, Journal of Magnetic Resonance Imaging **41**.3 (2015) 694, ISSN: 15222586 (cit. on p. 26).

[67] J. E. Jensen, B. de B. Frederick and P. F. Renshaw, *Grey and white matter GABA level differences in the human brain using two-dimensional, J-resolved spectroscopic imaging*, NMR in Biomedicine **18**.8 (2005) 570, ISSN: 09523480 (cit. on pp. 26, 78, 81).

[68] I. Y. Choi et al., *In vivo detection of gray and white matter differences in GABA concentration in the human brain*, NeuroImage **33**.1 (2006) 85, ISSN: 10538119 (cit. on pp. 26, 78, 81).

[69] J. Near et al., *Chemical shifts and coupling constants of the GABA spin system*, Proc. Intl. Soc. Mag. Reson. Med. **20**.1993 (2012) 4386 (cit. on pp. 26, 27).

[70] L. G. Kaiser et al., *A detailed analysis of localized J-difference GABA editing: theoretical and experimental study at 4T*, NMR in Biomedicine **21**.1 (2008) 22, eprint: https://onlinelibrary.wiley.com/doi/pdf/10.1002/nbm.1150 (cit. on p. 27).

[71] V. Govindaraju, K. Young and A. A. Maudsley, *Proton NMR chemical shifts and coupling constants for brain metabolites*, NMR in Biomedicine **13**.3 (2000) 129 (cit. on p. 27).

[72] L. R. Squire, *Memory and the hippocampus: a synthesis from findings with rats, monkeys, and humans.*, eng, Psychol Rev **99**.2 (Apr. 1992) 195, ISSN: 0033-295X (Print); 0033-295X (Linking) (cit. on p. 28).

[73] W. J. P. Henneman et al., *Hippocampal atrophy rates in Alzheimer disease: added value over whole brain volume measures.*, eng, Neurology **72**.11 (Mar. 2009) 999, ISSN: 1526-632X (Electronic); 0028-3878 (Print); 0028-3878 (Linking) (cit. on p. 28).

[74] M. Brant-Zawadzki, G. D. Gillan and W. R. Nitz, *MP RAGE: a three-dimensional, T1-weighted, gradient-echo sequence–initial experience in the brain.*, Radiology **182**.3 (1992) 769, PMID: 1535892, eprint: https://doi.org/10.1148/radiology.182.3.1535892 (cit. on pp. 28, 54).

[75] J. J. L. Rodriguez et al., *Prevalence of dementia in Latin America, India, and China: a population-based cross-sectional survey*, The Lancet **372**.9637 (2008) 464, ISSN: 0140-6736 (cit. on p. 29).

[76] K. Le Meur et al., *GABA release by hippocampal astrocytes*, Frontiers in Computational Neuroscience **6**.August (2012) 1, ISSN: 1662-5188 (cit. on p. 29).

[77] Z. Wu et al., *Tonic inhibition in dentate gyrus impairs long-term potentiation and memory in an Alzheimer's disease model*, Nature Communications **5** (2014) 1 (cit. on p. 29).

[78] S. Jo et al.,
GABA from reactive astrocytes impairs memory in mouse models of Alzheimer's disease,
Nature Medicine **20** (June 2014) 886 (cit. on p. 29).

[79] K. Nehrke and P. Börnert,
DREAM-a novel approach for robust, ultrafast, multislice B1 mapping,
Magnetic Resonance in Medicine **68**.5 (2012) 1517, ISSN: 07403194 (cit. on p. 29).

[80] P. Ehses et al., *Whole-brain B1-mapping using three-dimensional DREAM*,
Magnetic Resonance in Medicine November 2018 (2019) mrm.27773, ISSN: 0740-3194
(cit. on pp. 29, 54).

[81] E. Schneider and G. Glover, *Rapid in Vivo Proton Shimming*,
Magnetic Resonance in Medicine **347** (1991) 335 (cit. on p. 29).

[82] L. Fang et al., *Adaptively optimized combination (AOC) of magnetic resonance spectroscopy data from phased array coils*,
Magnetic Resonance in Medicine **2244** (2015) 2235, ISSN: 15222594 (cit. on p. 33).

[83] M. Wu et al., *Adaptively Optimized Combination (AOC) of Phased-Array MR Spectroscopy Data in the Presence of Correlated Noise: Compared with Noise-Decorrelated or Whitened Methods*,
Magnetic Resonance in Medicine **78**.3 (2017) 848, ISSN: 0740-3194 (cit. on p. 33).

[84] W. Du et al., *Reduction of spectral ghost artifacts in high-resolution echo-planar spectroscopic imaging of water and fat resonances*,
Magnetic Resonance in Medicine **49**.6 (2003) 1113, ISSN: 07403194 (cit. on p. 33).

[85] F. J. Harris,
On the Use of Windows for Harmonic Analysis with the Discrete Fourier Transform,
Proceedings of the IEEE **66**.1 (1978) 51, ISSN: 15582256 (cit. on p. 34).

[86] U. Klose, *In vivo proton spectroscopy in presence of eddy currents.*, eng,
Magn Reson Med **14**.1 (Apr. 1990) 26, ISSN: 0740-3194 (Print); 0740-3194 (Linking)
(cit. on p. 34).

[87] D. M. Spielman et al.,
Motion correction and lipid suppression for H-1 magnetic resonance spectroscopy,
Magnetic Resonance in Medicine **43**.3 (2000) 325 (cit. on p. 36).

[88] G. Helms and A. Piringer, *Restoration of motion-related signal loss and line-shape deterioration of proton MR spectra using the residual water as intrinsic reference*,
Magnetic Resonance in Medicine **46**.2 (2001) 395, ISSN: 07403194 (cit. on p. 36).

[89] T. Thiel et al.,
Phase coherent averaging in magnetic resonance spectroscopy using interleaved navigator scans: Compensation of motion artifacts and magnetic field instabilities,
Magnetic Resonance in Medicine **47**.6 (2002) 1077, ISSN: 07403194 (cit. on p. 36).

[90] K. Waddell et al., *A practical guide to robust detection of GABA in human brain by J-difference spectros- copy at 3 T using a standard volume coil.*,
Magn Reson Imaging **25**.7 (2007) 1032 (cit. on p. 36).

[91] J. Near et al., *Frequency and phase drift correction of magnetic resonance spectroscopy data by spectral registration in the time domain*,
Magnetic Resonance in Medicine **73**.1 (2015) 44, ISSN: 15222594 (cit. on pp. 36, 37).

[92] P. G. Mullins et al.,
Current practice in the use of MEGA-PRESS spectroscopy for the detection of GABA,
NeuroImage **86** (2014) 43, ISSN: 10959572, arXiv: NIHMS150003 (cit. on p. 38).

[93] P. O. Magnusson et al., *Gamma-aminobutyric acid edited echo-planar spectroscopic imaging (EPSI) with MEGA-sLASER at 7T*,
Magnetic Resonance in Medicine **81**.2 (2019) 773, ISSN: 15222594 (cit. on pp. 39, 82).

[94] R. Kreis, *Issues of spectral quality in clinical 1H-magnetic resonance spectroscopy and a gallery of artifacts*, NMR in Biomedicine **17**.6 (2004) 361, ISSN: 09523480
(cit. on pp. 40, 64).

[95] A. Henning et al.,
Clinical Proton MR Spectroscopy in Central Nervous System Disorders,
Radiology **270**.3 (2014) 658, ISSN: 0033-8419 (cit. on pp. 40, 64).

[96] M. Wilson, P. B. Barker and P. J. Bolan,
Spectroscopy of the Brain : Review and Recommendations, **82**.2 (2020) 527
(cit. on pp. 40, 64).

[97] Feb. 2016 (cit. on p. 44).

[98] S. A. Smith et al., *Computer Simulations in Magnetic Resonance. An Object-Oriented Programming Approach*, 1994 (cit. on p. 46).

[99] Y. Kilian, *B0 Shimming zweiter und dritter Ordnung am 7 Tesla MRT für qualitativ hochwertige Single-Voxel Spektroskopie*, 2019 (cit. on p. 51).

[100] C. J. Evans, D. J. McGonigle and R. A. E. Edden, *Diurnal stability of γ-aminobutyric acid concentration in visual and sensorimotor cortex*,
Journal of Magnetic Resonance Imaging **31**.1 (2010) 204, ISSN: 10531807 (cit. on p. 65).

[101] M. G. Saleh et al.,
Reproducibility of macromolecule suppressed GABA measurement using motion and shim navigated MEGA-SPECIAL with LCModel, jMRUI and GANNET,
Magnetic Resonance Materials in Physics, Biology and Medicine **29**.6 (2016) 863,
ISSN: 13528661 (cit. on p. 65).

[102] D. C. Shungu et al., *Brain γ-aminobutyric acid (GABA) detection in vivowith the J -editing 1H MRS technique: a comprehensive methodological evaluation of sensitivity enhancement, macromolecule contamination and test-retest reliability*,
NMR in Biomedicine May (2016) 932, ISSN: 09523480 (cit. on p. 65).

[103] H. Prinsen et al.,
Reproducibility Measurement of Glutathione, GABA, and Glutamate: Towards In Vivo Neurochemical Profiling of Multiple Sclerosis with MR Spectroscopy at 7 Tesla,
45.1 (2017) 187 (cit. on p. 66).

[104] S. A. Wijtenburg et al., *Reproducibility of brain spectroscopy at 7T using conventional localization and spectral editing techniques*,
Journal of Magnetic Resonance Imaging **38**.2 (2013) 460, ISSN: 10531807 (cit. on p. 66).

[105] A. Baeshen et al., *Test – Retest Reliability of the Brain Metabolites GABA and Glx With JPRESS , in vivo at 3T*, J. MAGN. RESON. IMAGING **51** (2020) 1181 (cit. on p. 66).

[106] C. A. Van Den Berg et al., *Simultaneous B1+ homogenization and specific absorption rate hotspot suppression using a magnetic resonance phased array transmit coil*,
Magnetic Resonance in Medicine **57**.3 (2007) 577, ISSN: 07403194 (cit. on p. 66).

[107] Y. Zhang, M. Brady and S. Smith, *Segmentation of brain MR images through a hidden Markov random field model and the expectation-maximization algorithm*,
IEEE Transactions on Medical Imaging **20**.1 (2001) 45 (cit. on pp. 66, 73).

[108] J. Snyder et al., *Selective excitation of two-dimensional arbitrarily shaped voxels with parallel excitation in spectroscopy*, Magnetic Resonance in Medicine **67**.2 (2012) 300, ISSN: 07403194 (cit. on p. 66).

[109] H. Zhu et al., *High resolution spectroscopic imaging of GABA at 3 Tesla*,
Magnetic Resonance in Medicine **65**.3 (2011) 603, ISSN: 15222594 (cit. on p. 69).

[110] W. Bogner et al., *3D GABA imaging with real-time motion correction, shim update and reacquisition of adiabatic spiral MRSI*, NeuroImage **103** (2014) 290, ISSN: 10959572 (cit. on p. 69).

[111] G. Hangel et al., *Inter-subject stability and regional concentration estimates of 3D-FID-MRSI in the human brain at 7 T*, NMR in Biomedicine **34**.12 (2021) 1, ISSN: 10991492 (cit. on p. 69).

[112] R. Stirnberg et al., *Rapid fat suppression for three-dimensional echo planar imaging with minimized specific absorption rate*,
Magnetic Resonance in Medicine **76**.5 (2016) 1517, ISSN: 15222594 (cit. on p. 69).

[113] R. Stirnberg et al., *Rapid whole-brain resting-state fMRI at 3 T: Efficiency-optimized three-dimensional EPI versus repetition time-matched simultaneous-multi-slice EPI*,
NeuroImage **163** (2017) 81, ISSN: 1053-8119 (cit. on p. 69).

[114] R. Stirnberg and T. Stöcker, *Segmented K-space blipped-controlled aliasing in parallel imaging for high spatiotemporal resolution EPI*,
Magnetic Resonance in Medicine **85**.3 (2021) 1540, ISSN: 15222594 (cit. on p. 69).

[115] B. Strasser et al., *Coil combination of multichannel MRSI data at 7 T: MUSICAL*,
NMR in Biomedicine **26**.12 (2013) 1796, ISSN: 09523480 (cit. on p. 82).

[116] W. Bogner, R. Otazo and A. Henning,
Accelerated MR spectroscopic imaging—a review of current and emerging techniques,
NMR in Biomedicine November 2019 (2020) 1, ISSN: 10991492 (cit. on p. 82).

[117] E. Coello et al., *High-resolution echo-planar spectroscopic imaging at ultra-high field*,
NMR in Biomedicine **31**.11 (2018) 1, ISSN: 10991492 (cit. on p. 82).

[118] J. K. Furuyama, N. E. Wilson and M. A. Thomas,
Spectroscopic imaging using concentrically circular echo-planar trajectories in vivo,
Magnetic Resonance in Medicine **67**.6 (2012) 1515, ISSN: 15222594 (cit. on p. 82).

[119] P. Moser et al., *Whole-slice mapping of GABA and GABA + at 7T via adiabatic MEGA-editing, real-time instability correction, and concentric circle readout*,
NeuroImage **184** (2019) 475, ISSN: 10959572 (cit. on p. 82).

[120] G. Weng et al., *SLOW : A novel spectral editing method for whole-brain MRSI at ultra high magnetic field*, Magnetic Resonance in Medicine October 2021 (2022) 53,
ISSN: 0740-3194 (cit. on p. 83).

APPENDIX A

Appendix

A.1 Additional tables

step	excitation	AFP 1	AFP 2	readout
1	0	0	0	0
2	0	90	0	0
3	0	180	0	0
4	0	270	0	0
5	0	0	90	0
6	0	90	90	0
7	0	180	90	0
8	0	270	90	0
9	0	0	180	0
10	0	90	180	0
11	0	180	180	0
12	0	270	180	0
13	0	0	270	0
14	0	90	270	0
15	0	180	270	0

Table A.1: Pulse and readout phases (in degrees) during a 16-step phase cycles

A.2 Additional figures

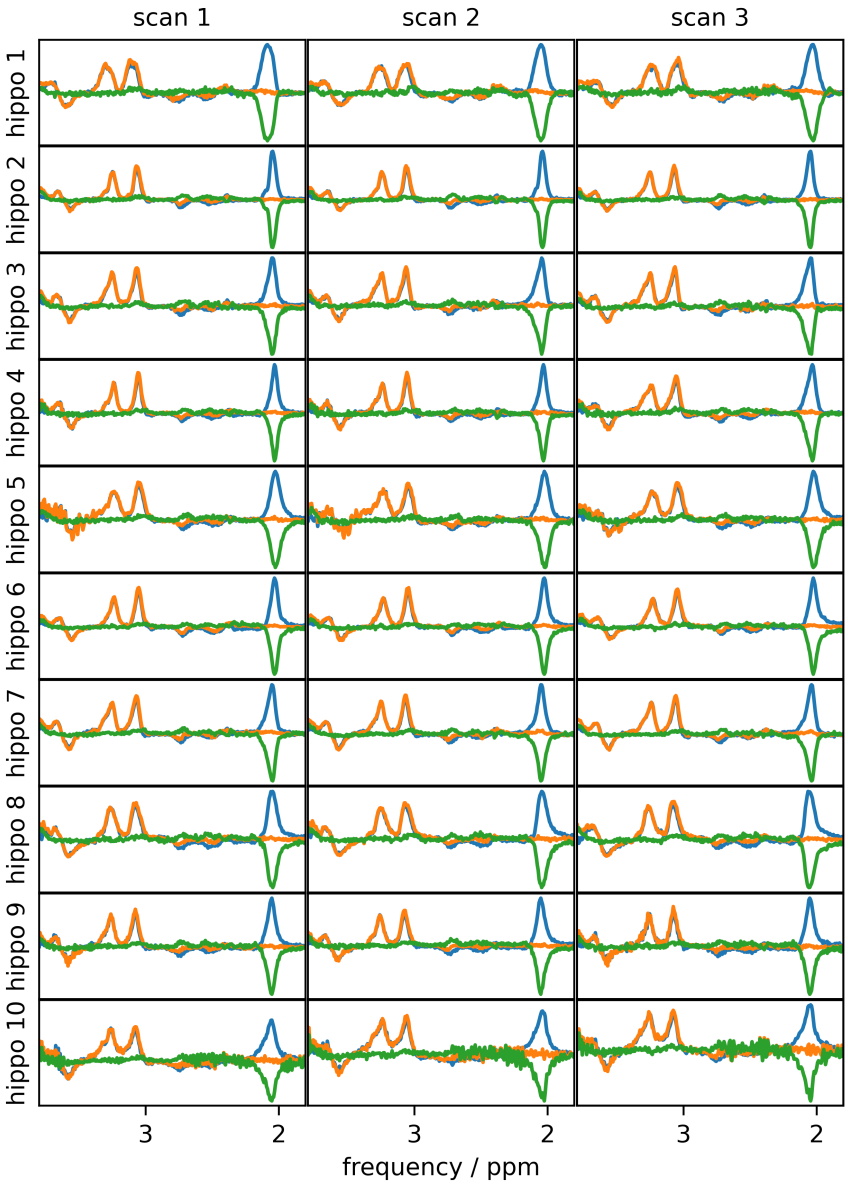

Figure A.1: Edit-off (blue), edit-on (green), and difference (red) spectra of all measurements of all subjects scanned in the hippocampus reproducibility study

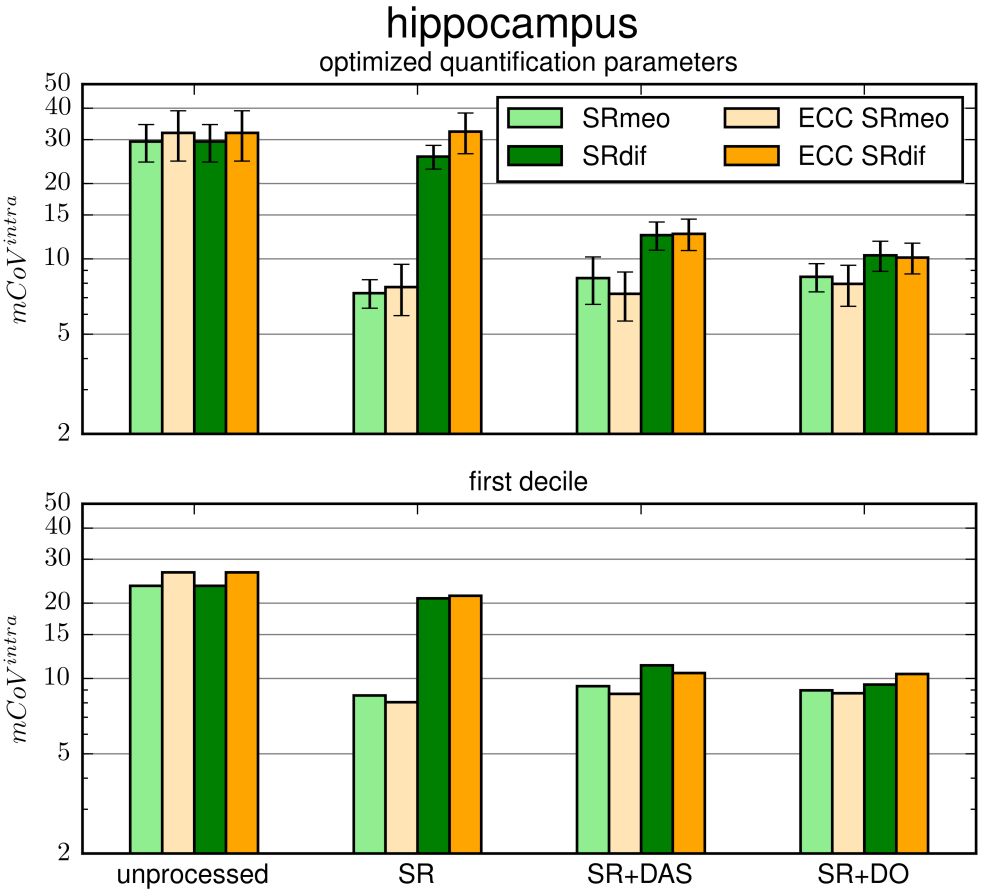

Figure A.2: $mCoV^{\text{intra}}$ in the hippocampus for all tested data processing approaches. On the x-axis the phase and frequency method is shown (None, SR, SR+DAS, SR+DO), and the bars represent different ECC settings and SR references. The top plot shows the $mCoV^{\text{intra}}$ obtained with the optimal TARQUIN parameters, while the bottom plot shows the top decile of the $mCoV^{\text{inter}}$of all the 169 pairs of n_s for each data processing routine.

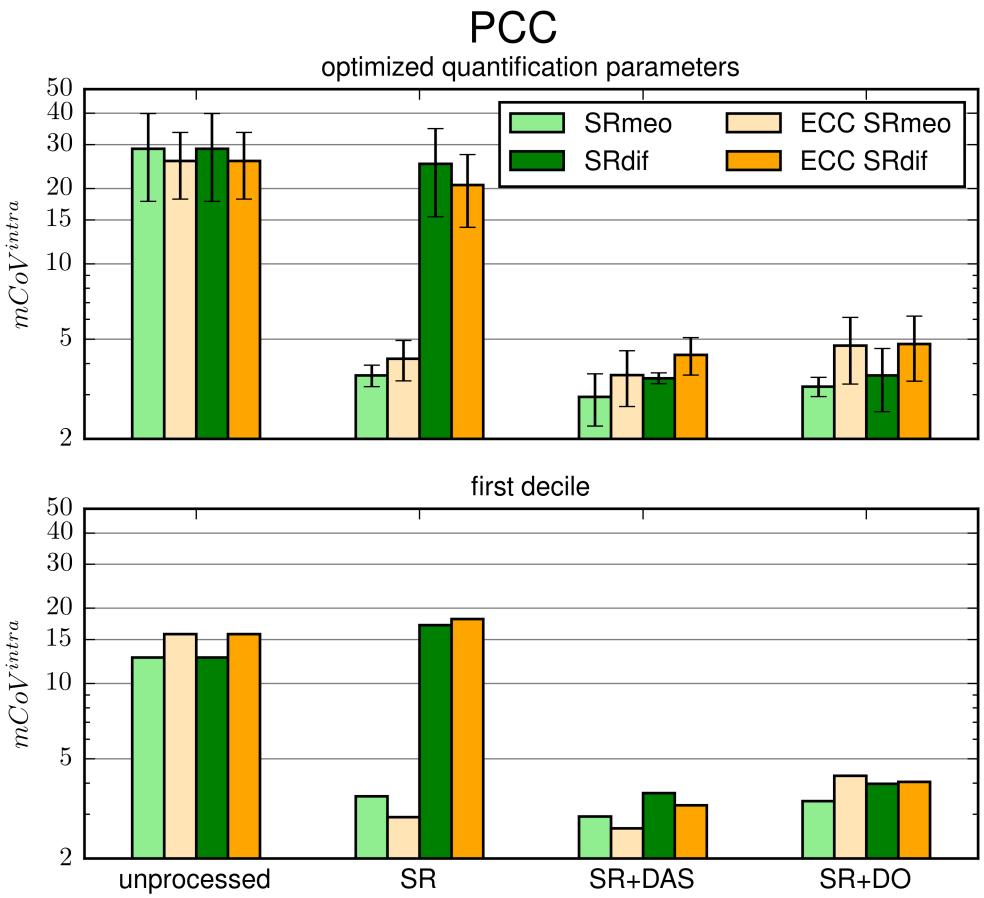

Figure A.3: $mCoV^{\text{intra}}$ in the PCC for all tested data processing approaches. On the x-axis the phase and frequency method is shown (None, SR, SR+DAS, SR+DO), and the bars represent different ECC settings and SR references. The top plot shows the $mCoV^{\text{inter}}$ obtained with the optimal TARQUIN parameters, while the bottom plot shows the top decile of the $mCoV^{\text{inter}}$of all the 169 pairs of n_s for each data processing routine.

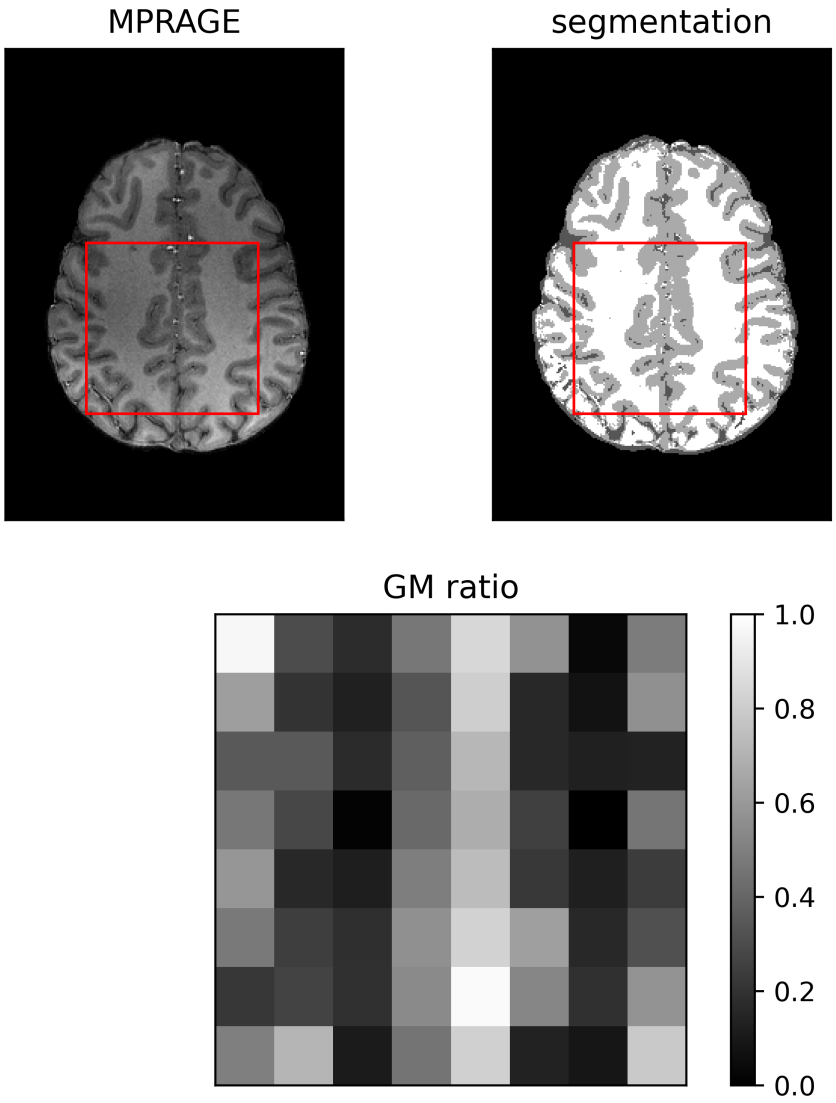

Figure A.4: One slice of the MPRAGE acquisition (top left). The same slice segmented into gray matter, white matter, ans CSF (top right) and the resulting GMF (bottom)

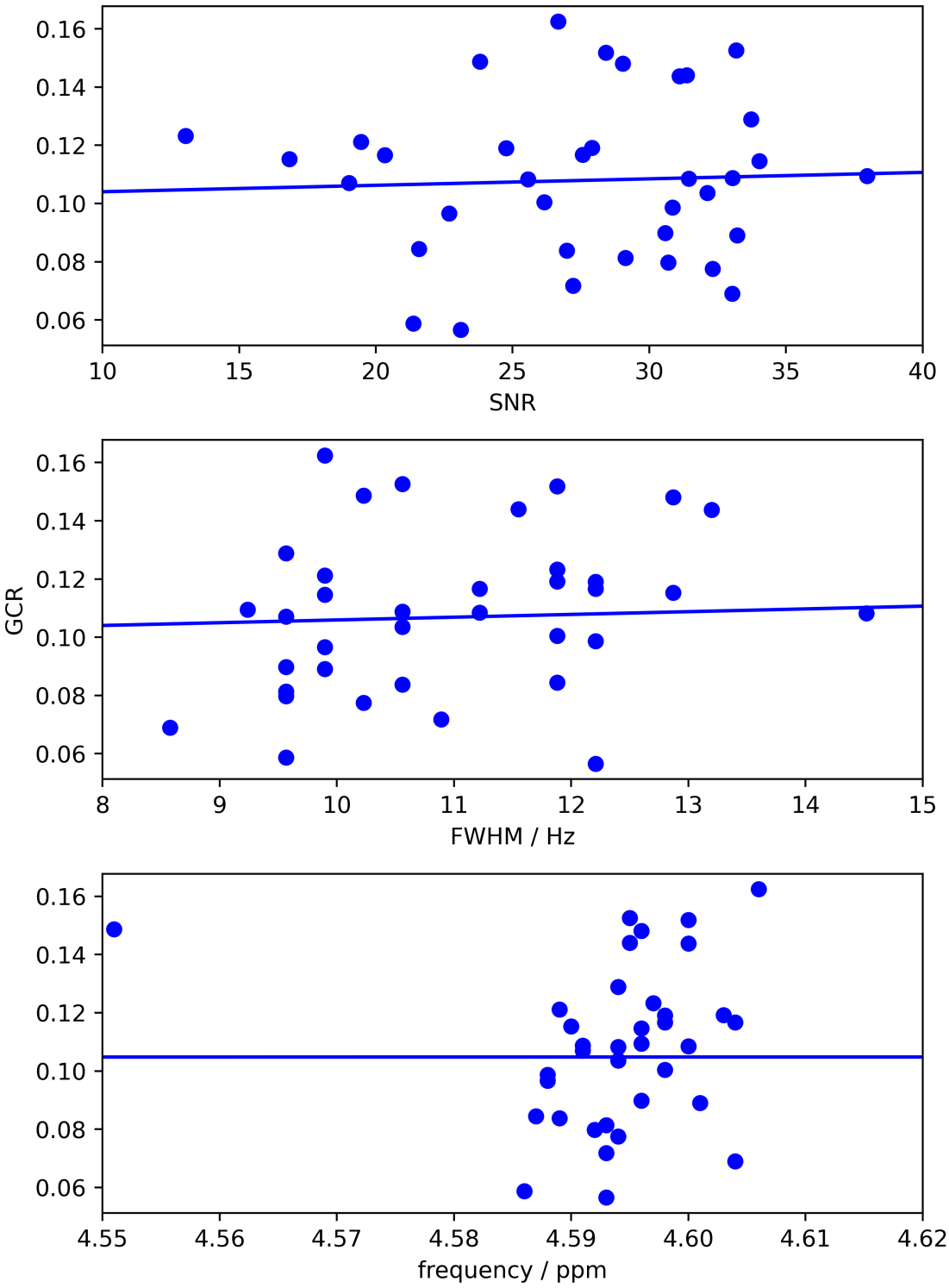

Figure A.5: Dependence of the B_1-corrected GCR on the SNR, FWHM and local B_0. No significant dependence was found.

List of Figures

List of Tables